

Investigation of transverse-momentum-dependent functions
(TMD) in azimuthal spin asymmetries of semi-inclusive
deep inelastic nucleon scattering.

Erforschung transversalimpulsabhängiger Verteilungen
(TMD) durch azimuthale Spin-Asymmetrien in
semi-inklusive tief-inelastischer Nukleon-Streuung.

Inaugural-Dissertation
zur Erlangerung des Doktorgrades der Naturwissenschaften
der Justus-Liebig-Universität Gießen
Fachbereich 07
(Mathematik und Informatik, Physik, Geographie)

vorgelegt von
Vitaly Zagrebelnyy
aus Hamburg, Deutschland

II. Physikalisches Institut der Justus-Liebig Universität Gießen

2015

Contents

Zusammenfassung	iv
1 Introduction	1
2 Theory	3
2.1 Deep-inelastic scattering	3
2.2 Quark parton model	7
2.3 Quantum chromodynamics	8
2.4 Semi-inclusive deep-inelastic scattering	11
2.5 Transverse-momentum dependent functions	12
2.5.1 Sivers effect	18
2.5.2 Collins function	21
2.6 Beam-spin effects	23
3 The HERMES experiment at HERA	26
3.1 Polarimeters	27
3.2 The target	28
3.3 Spectrometer	33
3.3.1 Tracking detectors	34
3.3.2 Transition radiation monitor (TRD)	34
3.3.3 The preshower detector	35
3.3.4 The calorimeter	35
3.3.5 Ring imaging Cherenkov detector	36
3.3.6 Luminosity monitor	40
3.3.7 Hodoscopes	41
3.4 Particle identification	41
3.5 Data acquisition	43
4 Data Analysis	45
4.1 Data quality	45
4.2 Event selection	46

4.2.1	Particle identification cuts	47
4.2.2	Reconstruction cuts	47
4.2.3	Geometric cuts	48
4.2.4	Kinematic cuts	48
4.3	Extraction of $A_{LU}^{\sin\phi_h}$ asymmetries	50
4.4	Yields and kinematic bins	54
4.5	Choice of normalization (DIS events/Luminosity)	58
4.6	Charge symmetric background	59
4.7	Data merging	61
4.8	Crosscheck of results	71
5	Systematics	75
5.1	RICH unfolding procedure	75
5.2	Additional azimuthal modulations	77
5.3	Uncertainty of measurement of beam polarization	80
5.4	3-in-1 procedure	81
5.4.1	Parametrization of asymmetry	82
5.4.2	Implementation of asymmetries in MC	90
5.4.3	MC validation check	91
5.4.4	Uncertainty due to acceptance, smearing and radiation effects	96
5.5	Total systematics	99
6	Final results	100
6.1	Comparison with CLAS and COMPASS experiments	105
6.2	Comparison with theory	107
	Conclusion	114
	Bibliography	115
	Erklärung zur Dissertation	123

Zusammenfassung

In der vorliegenden Arbeit wurden Strahlpolarisationsasymmetrien (BSA) in semi-inklusiver tief-inelastischer Streuung (SIDIS) für geladene Pionen, Kaonen, Protonen und Antiprotonen berechnet. Die analysierten Daten wurden am HERMES Experiment von 1996-2007 mit longitudinal polarisierten Elektronen/Positronen, die an Protonen oder Deuteronen gestreut wurden, gesammelt. Die hier vorgestellte Analyse baut auf bereits veröffentlichte Ergebnisse auf (siehe [28]). Die Übereinstimmung mit den früher veröffentlichten Ergebnissen sowie die unabhängige Überprüfung jedes Analyseschrittes untermauert die Genauigkeit dieser Arbeit.

Im Rahmen der TMD-Faktorisierung (siehe sec. 2.5) stellen die erhaltenen Asymmetrieamplituden Summen von Faltungen verschiedener Partonverteilungen (PDFs) und Fragmentationsfunktionen (FFs) dar. Diese TMD Funktionen beschreiben die Korrelationen zwischen Transversalimpuls der Partonen (insbesondere der Quarks), deren Spin, dem Spin der Nucleonen sowie dem Transversalimpuls der Hadronen im Endzustand. Zu diesen TMDs gehören die Collins FF H_1^\perp , Boer Mulders PDF h_1^\perp , unpolarisierte PDF f_1 und die spin-unabhängige FF D_1 . In den hier analysierten Asymmetrien sind jeweils eine Twist-2 Funktionen mit einer unbekanntem Twist-3 Funktionen verbunden: e , \tilde{G}^\perp , g^\perp , \tilde{E} . Die Effekte des Twist-3 sind schwieriger zu erforschen, da sie üblicherweise durch den Faktor $1/Q$ unterdrückt sind. Die hier vorgestellte Analyse könnte jedoch dazu beitragen, das Wissen über die Twist-3-Funktionen zu verbessern.

Die π^+ Asymmetrien, gemessen in der Streuung an Protonen und Deuteronen, sind positiv. Die π^- Asymmetrien und K^+ sind ebenfalls leicht positiv. Die K^- , p and \bar{p} Asymmetrien sind verräglich mit Null. Die Asymmetrien der Pionen steigen mit zunehmendem z an. Im Allgemeinen nehmen die Asymmetrien für alle Teilchen mit abnehmenden $P_{h\perp}$ ab. Die Asymmetrien der Pionen wurden mit Ergebnissen von den COMPASS und CLAS Experimenten verglichen, in denen jeweils Daten aus der Streuung an ${}^6\text{LiD}$ bzw. Wasserstoff, analysiert wurden. Die Pionasymmetrien sind deckungsgleich mit den COMPASS Resultaten (siehe fig. 6.10). Die π^+ Asymmetrie ist auch in guter Übereinstimmung mit den CLAS Ergebnissen. Die π^- Asymmetrie stimmt mit den x und $P_{h\perp}$ Projektionen überein, während sie eine umgekehrte Abhängigkeit von z vorweist. Man kann daran die unterschiedliche Rolle der TMD Funktionen in den verschiedenen kinematischen Intervallen der Experimente sehen (siehe fig. 6.11). Die Ergebnisse wurden weiterhin mit theoretischen Prognosen verglichen (siehe sec. 6.2). Im Allgemeinen stimmen die Ergebnisse nur teilweise mit dem theoretischen Modell überein. Dies könnte evtl. auf das Fehlen von $f_1\tilde{G}^\perp$ und $h_1^\perp\tilde{E}$ zurückgeführt werden (diese wurden im Modell vernachlässigt).

Wichtige neue Aspekte dieser Analyse gegenüber der vorherigen HERMES Publikation sind die Ergebnisse, die in der Streuung an Deuteronen erhalten wurden. Weiterhin stellen die Asymmetrien für Kaonen, Protonen, Antiprotonen und das 3-dimensionale Binning, welches die gleichzeitige Abhängigkeit der Asymmetrien von x , z , und $P_{h\perp}$ zeigen, wesentliche Neuerungen dar. Die Resultate für das 3-dimensionale Binning sind auch weniger empfindlich gegenüber Akzeptanzeffekten (siehe sec. 5.4). Alle diese Ergebnisse werden hier zum ersten Mal präsentiert

und machen eine Verbesserung der theoretischen Modelle möglich.

Chapter 1

Introduction

For many years physicists have investigated the inner structure of matter. In 1897 the electron was discovered by J.J. Thomson. In 1913 E. Rutherford showed that atoms have a substructure and contain compact nuclei surrounded by electrons. Rutherford's experimental nucleus was hydrogen. It received the name "proton". In 1932 the proton was accompanied by the discovery of the neutron by Chadwick. Consequent experiments revealed an enormous number of particles which were classified by M. Gell-Mann and Y. Ne'emann in 1961 in "Eightfold Way" conception [1]. In 1968 the particle accelerator SLAC revealed a substructure of the proton [2]. From that moment quarks appeared to be constituents of protons and neutrons. Evidence of gluons was discovered in three-jet events at PETRA (DESY) in 1979 [3]. This and other results confirmed the success of quantum chromodynamics (QCD) which was developed in 1950s and 1960s. The QCD successfully explained strong interactions between quarks and gluons. The latter, like photons in quantum electrodynamics (QED), are mediators of the strong interaction. In 1969 the quark-parton-model (QPM) was presented by R. Feynman and J.Bjorken [4], which could explain the results of deep-inelastic scattering (DIS) experiments at that moment. But following experiments produced new questions for theorists. The "spin crisis" [5] effect observed by EMC in 1987 revealed that only a small fraction of the proton spin originates from its quarks. Large azimuthal single-spin asymmetries observed in 70s and 80s at Fermilab [6,7] in hadron production at proton collisions also could not be explained in the framework of the QPM. Later asymmetries were observed by HERMES, CLAS, SMC and COMPASS in semi-inclusive hadron production [8,9,10,11] and by the collider experiments STAR, PHENIX and BRAHMS [12,13,14]. The failure of the QPM of the 70s required new approaches to spin effects. Based on QCD theory approach of transverse-momentum-dependent (TMD) parton distributions and fragmentation functions was investigated [15]- [20]. Transverse-momentum-dependent functions describe intrinsic motion of quarks and gluons inside hadrons due to correlations between transverse momentum of quark, quark spin, target nucleon spin, and transverse momentum of final-state particle. Examples of them are the Sivers function [18], which represents the distribution of unpolarized quarks in a transversely polarized nucleon, and the Collins function [36],

which describes fragmentation of transversely polarized quarks into unpolarized hadrons. The introduction of TMD functions gave the possibility to explain the large single-spin asymmetries and helped to learn more about the proton spin.

Beam-spin asymmetries in semi-inclusive DIS reveal new effects related to quark-gluon correlations and their corresponding TMDs. The beam-spin asymmetry was measured both at HERMES [28], CLAS [30,31], COMPASS [11]. Significantly non-zero asymmetries were observed for positive and neutral pions. The work presented here expands results from [28] using a larger data sample on a hydrogen target. Furthermore, data are collected also on a deuterium target. Results are presented for charged pions, and for the first time charged kaons, protons and antiprotons.

Chapter 2

Theory

2.1 Deep-inelastic scattering

Let us consider a deep-inelastic lepton-proton (lepton-nucleon) scattering process with *assumption of one-photon exchange* described by:

$$l + N \rightarrow l' + X. \quad (2.1)$$

Here, the lepton scatters off the nucleon and transfers part of its four-momentum through the virtual photon γ^* . It breaks up the nucleon leading to a final hadronic state X that remains unobserved.

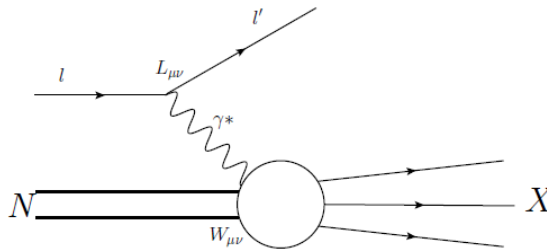


Figure 2.1: Scheme of DIS event

Particles appearing neither in the initial nor in the final state are called *virtual*. In fig. 2.1 the virtual photon appears only in the interaction point and is used to describe quantities of energy-momentum transfer in DIS process.

Via parameter comparisons of the initial and scattered lepton one can extract information about the inner structure of the nucleon. A reaction where only the scattered lepton is detected is called *inclusive*, or DIS reaction (see fig. 2.1). If in coincidence with the lepton at least one of the produced hadrons is detected the reaction is called *semi-inclusive*, or SIDIS reaction. If all products of a reaction are identified the reaction is called *exclusive*. The Trento conventions [27] define angles and vectors of all participating particles in the reaction.

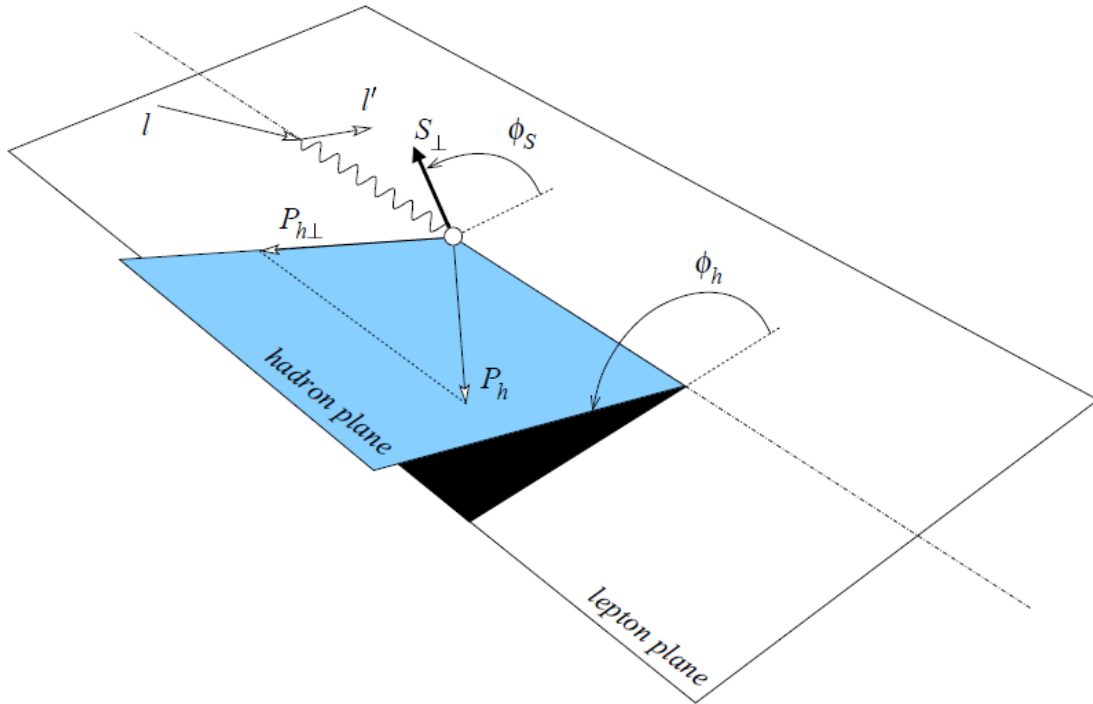


Figure 2.2: Definition of azimuthal angles for semi-inclusive deep-inelastic scattering in the target rest frame. The plot is taken from [27]

In fig. 2.2 SIDIS reaction is shown. The virtual photon is denoted by the wavy line. The transverse components of the momentum P_h of the produced hadron and of the target spin S are $P_{h\perp}$ and S_{\perp} correspondingly. The angle between the target spin and the lepto-production plane (ll') is ϕ_S . The angle between the lepto-production plane and the hadron plane (qP_h) is ϕ_h .

Common kinematic variables used both in DIS and SIDIS analysis are Q^2 , W^2 , ν , y , x . Additional variables z , $P_{h\perp}$, ϕ_h are used in case of SIDIS:

- l ... four-momentum of the initial lepton
- E ... energy of the initial lepton
- l' ... four-momentum of the scattered lepton
- E' ... energy of the scattered lepton
- M ... mass of the target nucleon (in following text it will be identified as the mass of the proton)
- $\mathbf{P}^{\text{lab}}(M,0)$... four momentum of the target nucleon, which is at rest (fixed target) in the lab frame

- $\mathbf{q}=\mathbf{l}-\mathbf{l}'$... four-momentum transfer of the virtual photon to the target
- θ ... polar angle of the scattered lepton
- $Q^2=-\mathbf{q}^2 \approx 4EE' \sin^2 \frac{\theta}{2}$... negative squared 4-momentum of the virtual photon
It fixes the wave-length λ of the virtual photon $\lambda \sim \frac{1}{Q^2}$, and therefore determines the spatial resolution of the DIS process
- $\nu = \frac{\mathbf{P} \cdot \mathbf{q}}{M} \stackrel{lab}{=} E - E'$... energy transfer to the target
- $W^2 = (\mathbf{P} + \mathbf{q})^2 = M^2 + 2M\nu - Q^2$... invariant mass of the final state
It describes maximum energy of the reaction products (particle producing threshold)
- $x = \frac{Q^2}{2\mathbf{P} \cdot \mathbf{q}} = \frac{Q^2}{2M\nu}$... Bjorken scaling variable
It is dimensionless quantity which shows the *inelasticity* of the process (see [32]). For inelastic processes $W > M$ and $0 < x < 1$. For the elastic process $W = M$ and consequently $x = 1$. Also x can be interpreted in the infinite-momentum frame as the fraction of the nucleon momentum carried by the nucleon's constituent which absorbed the photon (see 2.15))
- $y = \frac{\mathbf{P} \cdot \mathbf{q}}{\mathbf{P} \cdot \mathbf{l}} \stackrel{lab}{=} \frac{\nu}{E}$... fractional energy transfer from lepton to proton
- $z = \frac{\mathbf{P} \cdot \mathbf{P}_h}{\mathbf{P} \cdot \mathbf{q}} \stackrel{lab}{=} \frac{E_h}{\nu}$... fractional energy of virtual photon carried by the produced hadron
- $\theta_{\vec{P}_h \vec{\gamma}^*}$... angle between hadron and virtual photon momenta
- $P_{h\perp} = \sin \theta_{\vec{P}_h \vec{\gamma}^*} |\vec{P}_h|$... component of hadron momentum perpendicular to virtual-photon direction
- S_{\perp} - ... perpendicular component of the target spin \vec{S}
- $\phi_h = \frac{\vec{q} \times \vec{l} \cdot \vec{P}_h}{|\vec{q} \times \vec{l} \cdot \vec{P}_h|} \cos^{-1} \left(\frac{\vec{q} \times \vec{l} \cdot \vec{q} \times \vec{P}_h}{|\vec{q} \times \vec{l}| |\vec{q} \times \vec{P}_h|} \right)$... azimuthal angle between lepton scattering and hadron production planes
- $\phi_S = \frac{\vec{q} \times \vec{l} \cdot \vec{S}}{|\vec{q} \times \vec{l} \cdot \vec{S}|} \cos^{-1} \frac{\vec{q} \times \vec{l} \cdot \vec{q} \times \vec{S}}{|\vec{q} \times \vec{l}| \cdot |\vec{q} \times \vec{S}|}$

Following notation was adopted:

- **bold** symbols in above written equations denote four-component vectors
- $\stackrel{lab}{=}$ is case of using fixed target (laboratory frame)
- \approx is case of laboratory frame with neglection of electron mass in calculations Both ν and dimensionless y are complementary variables in DIS calculations

The differential cross section of the DIS process in the energy range $[E', E' + dE']$ within the solid angle $d\Omega$ can be expressed by (see [33]):

$$\frac{d^2\sigma}{d\Omega dE'} = \frac{\alpha^2}{2MQ^4} \frac{E'}{E} L_{\mu\nu} W^{\mu\nu} = \frac{\alpha^2}{2MQ^4} \frac{E'}{E} [L_{\mu\nu}^{(S)} W^{\mu\nu(S)} - L_{\mu\nu}^{(A)} W^{\mu\nu(A)}], \quad (2.2)$$

where α is the electromagnetic coupling constant, $L_{\mu\nu}$ and $W^{\mu\nu}$ are the leptonic and hadronic tensors which describe interactions at corresponding vertices (see fig. 2.1). The leptonic and hadronic tensors can be decomposed into symmetric (S) and anti-symmetric (A) parts, where only the anti-symmetric part is spin-dependent:

$$L_{\mu\nu} = L_{\mu\nu}^{(S)} + iL_{\mu\nu}^{(A)}, \quad (2.3)$$

$$W_{\mu\nu} = W_{\mu\nu}^{(S)} + iW_{\mu\nu}^{(A)}. \quad (2.4)$$

Due to the fact that the lepton is a point-like spin- $\frac{1}{2}$ particle, the symmetric and antisymmetric parts of the leptonic tensor can be calculated in quantum electrodynamics (QED):

$$L_{\mu\nu}^S(\mathbf{l}; \mathbf{l}') = 2[l_\mu l'_\nu + l_\nu l'_\mu - g_{\mu\nu}(\mathbf{l} \cdot \mathbf{l}' - m_l^2)], \quad (2.5)$$

$$L_{\mu\nu}^A(\mathbf{l}, \mathbf{s}; \mathbf{l}') = 2m_l \epsilon_{\mu\nu\gamma k} s^\gamma (l^k - l'^k), \quad (2.6)$$

where \mathbf{s} is spin of the quark, $g_{\mu\nu}$ denotes metric tensor, $\epsilon_{\mu\nu\gamma k}$ defines Levi-Civita tensor with $\epsilon^{0123} = 1$, and m_l is the lepton mass. Using symmetry arguments the non-calculable unknown hadronic tensor can be parametrized and simplified through a combination of the structure functions W_1, W_2, G_1, G_2 :

$$W_{\mu\nu}^S \propto W_1, W_2, \quad (2.7)$$

$$W_{\mu\nu}^A \propto G_1, G_2, \quad (2.8)$$

where W_1, W_2 are unpolarized and G_1, G_2 depend on the proton spin.

The structure functions depend on x and Q^2 . In Ref. [32] the weak dependence of the structure functions on Q^2 at fixed values of x was proposed. This phenomena is called *Bjorken scaling*:

$$\lim_{Q^2 \rightarrow \infty} MW_1(Q^2, x) = F_1(x), \quad (2.9)$$

$$\lim_{Q^2 \rightarrow \infty} \nu W_2(Q^2, x) = F_2(x), \quad (2.10)$$

$$\lim_{Q^2 \rightarrow \infty} \nu M^2 G_1(Q^2, x) = g_1(x), \quad (2.11)$$

$$\lim_{Q^2 \rightarrow \infty} \nu^2 M^2 G_2(Q^2, x) = g_2(x). \quad (2.12)$$

2.2 Quark parton model

The structure functions in DIS can be simplified in the system where the proton has infinite longitudinal momentum. In this frame transverse momenta and rest masses of the proton constituents (partons) are neglected for the moment. If the interaction time between the virtual photon and the constituent is short enough (Q^2 is high) it ensures that the interaction between the constituents inside the proton can be neglected. Therefore the proton momentum is equal to the sum of the longitudinal momenta of its constituents (*impulse approximation*). The interaction of the virtual photon with the proton can be approximated as a coherent sum of elastic interactions with the charged constituents:

$$d\sigma^{ep \rightarrow eX} \propto \sum_q e_q^2 q(x) d\sigma^{eq \rightarrow eq}, \quad (2.13)$$

$$\vec{p} = (\vec{p}_t \rightarrow 0, x \cdot \vec{P}), \quad (2.14)$$

$$\vec{p} = (\vec{p}_t \rightarrow 0, x \cdot \vec{P}), \quad (2.15)$$

where e_q^2 is the square of the elementary charge of the parton, $d\sigma^{eq \rightarrow eq}$ is the elementary elastic lepton-quark cross-section, $q(x)$ is a function that expresses the probability of finding a parton in the proton with a certain momentum fraction (parton distribution function).

Finally, the cross section of the DIS process in the quark parton model (QPM) can be presented as a combination of distribution functions of corresponding constituents multiplied by the squared charge of the constituents and convoluted with the elementary lepton-quark cross-section.

In the above described frame the parton spin can be aligned (+) or antialigned (-) to the proton spin. In the case of the transversely polarized target the proton spin can be presented through two opposite polarization states \uparrow , \downarrow . The parton distribution function can be split up into spin-oriented distribution functions:

$$\begin{aligned} q(x) &= q_+(x) + q_-(x) && \text{unpolarized,} \\ \Delta q(x) &= q_+(x) - q_-(x) && \text{polarized,} \\ \delta q(x) &= q_\uparrow(x) - q_\downarrow(x) && \text{transversity.} \end{aligned} \quad (2.16)$$

Using these PDFs, the four structure functions of the nucleon can be written as:

$$\begin{aligned}
 F_1(x) &= \frac{1}{2} \sum_q e_q^2 q(x), \\
 F_2(x) &= x \sum_q e_q^2 q(x) = 2xF_1, \\
 g_1(x) &= \frac{1}{2} \sum_q e_q^2 \Delta q(x), \\
 g_2(x) &= 0,
 \end{aligned} \tag{2.17}$$

where the second spin-dependent function, $g_2(x)$, vanishes in the QPM.

2.3 Quantum chromodynamics

The weak dependence of the structure functions on Q^2 (*scaling violation*) can be explained by the fact that partons continuously interact (*strong interaction*) via exchange of electrically neutral gluons inside the nucleon. Quantum chromodynamics was developed to describe strong interactions.

Quantum chromodynamics is part of the Standard Model. It has SU(3) symmetry and involves three "color" charges which present new quantum numbers. The QCD assumes that quarks are elementary spin- $\frac{1}{2}$ particles and gluons are spin-1 bosons, mediators of the interaction between quarks. Contrary to the quantum electrodynamics (QED) gluons carry (color) charge and can interact with each other. This fact produce two important features of QCD, which are dependent on the strong coupling constant α_S :

- *Confinement.* It holds quarks inside the nucleon and generally in a hadron (which is a "colorless" object) and prevents the existence of free coloured quark due to the dependence of α_S on Q^2 in the energy region $Q^2 \leq 1$:

$$\alpha_S(Q^2) \propto \frac{1}{\ln Q^2}. \tag{2.18}$$

- *Asymptotic freedom.* Oppositely, asymptotic freedom implies that with increasing Q^2 in the energy region $Q^2 \gg 1$ the coupling constant becomes smaller and quarks appear to be free, not interacting with each other. It offers the possibility to calculate cross sections of high-energy interactions in powers of α_S at high Q^2 by using *perturbation theory*:

$$\sigma = \sigma_{LO}(1 + \alpha_S C_1 + \alpha_S^2 C_2 + \dots). \tag{2.19}$$

QPM is only a partial case of QCD which uses the fact that the photon interacts instantly

with partons ($Q \rightarrow \infty$) and partons have no time to interact with each other.

Glucos can be probed by the photon when they split to quark-antiquark pairs (see fig. 2.3).

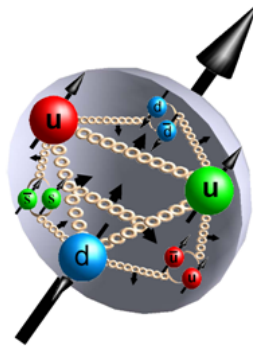


Figure 2.3: Schematic picture of constituent interactions inside the proton.

With increasing of Q^2 more gluons are resolved by the photon. Detected gluons share the nucleon momentum with quarks. Therefore the probability to find the quark with large momentum fraction decreases and to find the quark with low momentum fraction increases.

This fact can be demonstrated in "scaling violation effect", fig. 2.4, where the dependence of the measured structure function F_2 on Q^2 is presented.

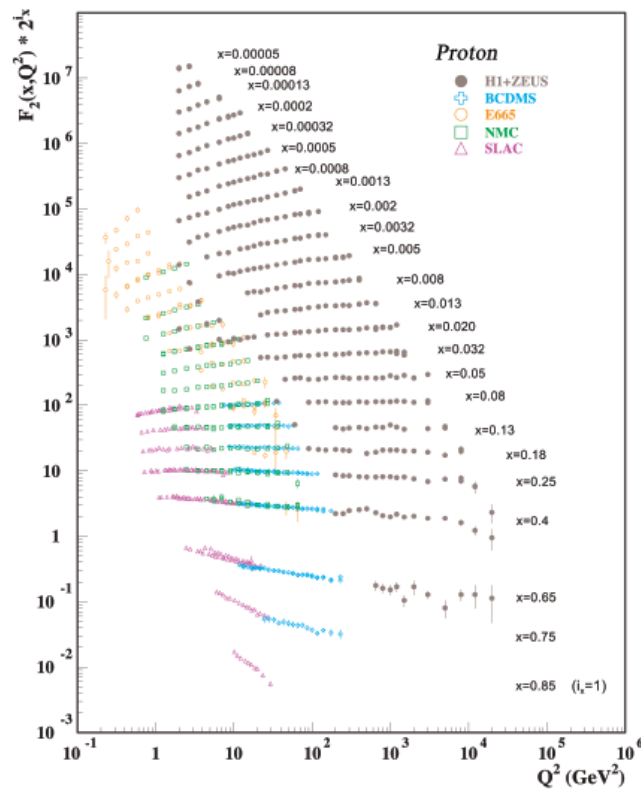


Figure 2.4: The proton structure function F_2 measured in electromagnetic scattering of electrons and positrons by protons. Plot is taken from [39].

Quarks can be classified as *valence quarks* and *sea quarks*. Valence quarks are responsible

for quantum numbers of the nucleon. Sea quarks appear as quark-antiquark pairs which can be produced and annihilated in the field of strong interaction. Parton and gluon distributions are depicted in Fig. 2.5. Contribution $x \cdot u_v$ and $x \cdot d_v$ shows the distributions of valence u and d quarks and $x \cdot s$ depicts increasing role of the sea-quark contribution in low-x range.

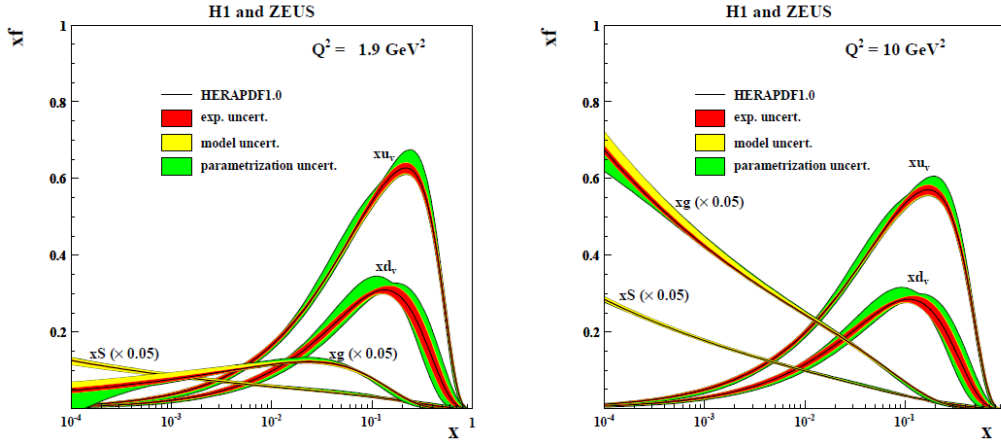


Figure 2.5: Parton distribution functions in a combined analysis by the H1 and ZEUS collaborations at $Q^2 = 1.9 \text{ GeV}^2$ and at $Q^2 = 10 \text{ GeV}^2$. Plot is taken from [40]

Photon-quark scattering can be understood as the superposition of all Feynman diagrams (processes) that are possible for this process (see fig. 2.6). Each diagram reflects amplitude of this process. The main process is determined by pure photon-quark scattering with cross-section σ_{LO} (Leading Order) and is depicted as the first diagram in fig. 2.6. Three additional diagrams include gluon radiation.

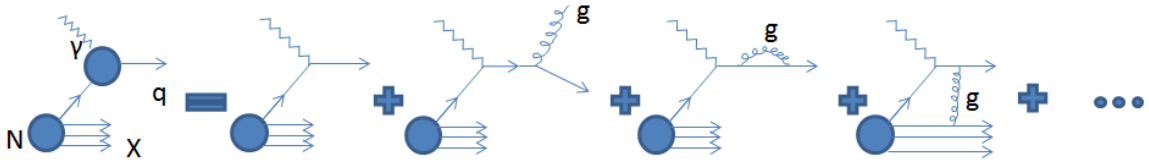


Figure 2.6: Schematic decomposition of SIDIS into various diagrams. First contributing diagram is of leading order. The other contribute due to gluon corrections

Not all diagrams with gluons are calculable. Collinear gluons emitted by the struck quark or the gluons with very small momentum (soft gluons) make the calculation of the cross section impossible because of divergence of the k_T -dependent integrals. The *divergence renormalization* technique is used for the correct estimation of these divergences and implies a special parameter, μ , the *factorization* scale. This parameter allows to include all non-perturbative (non-calculable) effects in PDF functions and leave perturbative effects (calculable) in the cross-section calculation. Often μ is taken equal to Q^2 for convenience reasons. Corrections to the hard cross section are applied on the level of $O(\alpha_S)$ because of collinear and soft gluons. Intending the connection with *evolution equations* or so called DGLAP equations [41] it is

possible to calculate $f_q(x, Q^2)$ at any Q^2 from a measured $f_q(x, Q_0^2)$ at Q_0^2 . Therefore results of two experiments in different kinematic ranges can be compared.

2.4 Semi-inclusive deep-inelastic scattering

Eq. 2.20 describes the SIDIS cross-section analogous to eq. 2.2 for the inclusive DIS cross-section and can be written (see [33]):

$$\frac{d\sigma}{dx dy d\psi dz d\phi_h dP_{h\perp}^2} = \frac{\alpha^2}{8zQ^4} L_{\mu\nu} W^{\mu\nu}. \quad (2.20)$$

It contains besides the dependence on the inclusive variables x , y , ψ also the dependence on the hadron variables z , ϕ_h , $P_{h\perp}^2$. Here ψ is the azimuthal angle of \mathbf{l}' around the lepton beam axis with respect to an arbitrary fixed direction. In DIS kinematics one has $d\psi \approx d\phi_S$ (for details see [34]). The hadronic tensor $W^{\mu\nu}$ now includes information on both target-hadron structure and the hadronization process (fragmentation) including of fragmentation functions (FFs). Fragmentation functions reflect the probability to find a quark q fragmenting into a hadron of type h carrying a fraction z of the energy of transferred virtual photon. An inclusive DIS reaction can be seen as the integrated case of SIDIS reactions over all produced hadrons.

For SIDIS with unpolarized hadrons in both the initial and final state the cross-section integrated over the transverse momentum of the hadron $\vec{P}_{h\perp}$ then reads:

$$\frac{d\sigma^{ep \rightarrow ehX}}{dx dQ^2 dz} \propto \sum_q e_q^2 q(x) \frac{d\sigma^{eq \rightarrow eq}}{dQ^2} D_q^h(z), \quad (2.21)$$

where $D_q^h(z)$ denotes the fragmentation function of the quark q into a hadron h . Often hadron and quark types in the notation of PDF and FF are omitted. Often PDFs are usually denoted with special letters, that define the alignment of spin states of the quark and the nucleon (see eq. 2.16): f is unpolarized, g is longitudinally polarized, h is transversely polarized. Superscripts define the dependence on transverse momentum of the quark and subscripts define the spin of the nucleon target. For example unpolarized PDF could be written as f_{1T}^\perp , where subscript determines the *twist* of the function (Here it is equal to 2. See twist explanation in [23]) and polarization state of the target nucleon (here it is transverse, T). The definition letters can change with increasing of twist number (see [23], [43]). For FF special letters defining spin alignment are: D is unpolarized, G is longitudinally polarized, H is transversely polarized. The number of FF can be decreased via application of *charge conjugation* and *isospin symmetry* to

only three for pions:

$$D_{q,fav} = D_u^{\pi^+}(z) = D_{\bar{u}}^{\pi^-}(z) = D_d^{\pi^+}(z) = D_{\bar{d}}^{\pi^-}(z), \quad (2.22)$$

$$D_{q,dis} = D_u^{\pi^-}(z) = D_{\bar{u}}^{\pi^+}(z) = D_d^{\pi^-}(z) = D_{\bar{d}}^{\pi^+}(z), \quad (2.23)$$

$$D_{q,s} = D_s^{\pi^+}(z) = D_{\bar{s}}^{\pi^-}(z) = D_{\bar{s}}^{\pi^+}(z) = D_s^{\pi^-}(z). \quad (2.24)$$

The FF $D_{q,fav}^h$ and $D_{q,dis}^h$ in eq. 2.24 are called *favoured* and *disfavoured* respectively. Their names reflect the fact that according to theory a u quark is more likely to fragment into a π^+ with valence structure of $|u\bar{d}\rangle$, while a d quark will be preferably fragmented into π^- with structure $|d\bar{u}\rangle$. The FF function $D_{q,s}^h$ is called *strange*. The strange quarks can be probed as sea quark-antiquark pairs.

Eq. 2.21 reflects *factorization*, which allows to separate the cross section in three main steps:

- the probability to find a quark in the nucleon (PDF), $q(x)$
- the elementary lepton-quark cross section, $d\sigma^{eq\rightarrow eq}$
- the probability that a quark fragments into a hadron of type h (FF), $D_q^h(z)$

Factorization was proved by Collins, Soper and Sterman in [17].

2.5 Transverse-momentum dependent functions

Using inclusive reaction and neglecting transverse momentum of the quark one can obtain only three PDFs in leading order (see eq. 2.16), where the transversity PDFs can be presented only in transverse polarization basis and can not be measured in usual DIS. However, taking into account transverse momentum of quarks in semi-inclusive reactions additional transverse-dependent PDFs can be obtained (see [15], [16]). Under the assumption that the detected hadron contains struck quark it is possible to connect through formulas the transverse momentum of the produced hadron with initial quark transverse momentum.

The spin states of the nucleon and its inner constituents can be decomposed into components of spin projections. The schematic decomposition of the nucleon state is illustrated in fig. 2.7. The coefficients $a_1 - a_6$ are probabilities of states with normalization $\sum a_i^2 = 1$

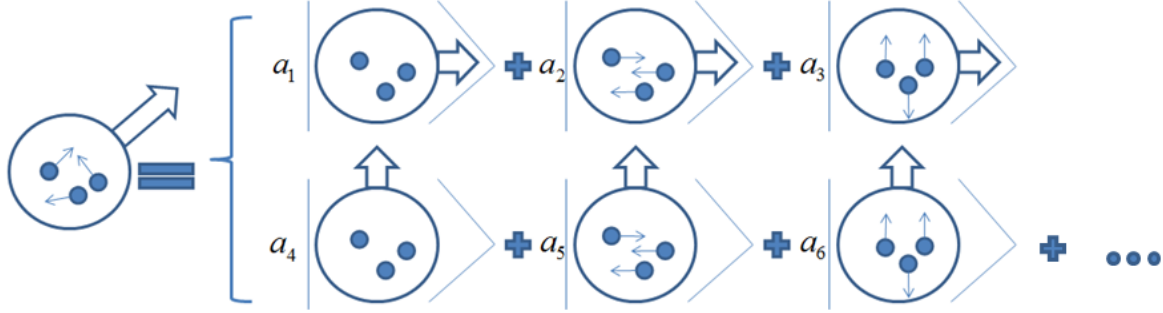


Figure 2.7: Schematic view of the nucleon spin state. Polarized states of the nucleon and quarks are indicated with arrows.

In inclusive DIS the hadronic tensor can be written:

$$W^{\mu\nu} = \sum_{q, \bar{q}} e_q^2 \int d^4\mathbf{p} \delta((\mathbf{p} + \mathbf{q})^2) \text{Tr}[\Phi \gamma^\nu (\not{\mathbf{p}} + \not{\mathbf{q}}) \gamma^\mu], \quad (2.25)$$

where \mathbf{p} is initial four-momentum of the quark, thus $\mathbf{k} = \mathbf{p} + \mathbf{q}$ is four-momentum of the fragmenting quark, $\Phi_{i,j}(\mathbf{p}, \mathbf{P}, \mathbf{S})$ is the correlation matrix (*quark correlator*). It can be read:

$$\Phi_{i,j}(\mathbf{p}, \mathbf{P}, \mathbf{S}) = \frac{1}{(2\pi^4)} \int d^4\xi e^{i\mathbf{p}\xi} \langle \mathbf{P}\mathbf{S} | \psi_j(\mathbf{0}) \psi_i(\xi) | \mathbf{P}\mathbf{S} \rangle, \quad (2.26)$$

where \mathbf{S} is the spin of the nucleon, $\psi_j(\mathbf{0})$ and $\psi_i(\xi)$ are local quark fields describing one type of quark. The correlation matrix relates initial state of the nucleon $|\mathbf{P}\mathbf{S}\rangle$ to the struck quark integrated over all separations of space time-coordinate ξ in space-time the quark might have.

For eq. 2.25 following assumptions are done:

- scattering process $e + p \rightarrow e' + X$ takes place on a quark,
- quark masses can be neglected

The quark-correlator can be decomposed in a basis of Dirac matrices $\gamma^{0,1,2,3}$, its product $\gamma^5 = i\gamma^0\gamma^1\gamma^2\gamma^3$, $\sigma^{\mu\nu} = \frac{i}{2}[\gamma^\mu, \gamma^\nu]$, and the unity matrix \mathbb{I} :

$$\Phi(\mathbf{k}, \mathbf{P}, \mathbf{S}) = \frac{1}{2} (\varsigma \mathbb{I} + \vartheta_\mu \gamma^\mu + A_\mu \gamma_5 \gamma^\mu + i\rho_5 \gamma_5 + i\tau_{\mu\nu} \sigma^{\mu\nu} \gamma_5), \quad (2.27)$$

where the parameters ς , ϑ_μ , A_μ , $\tau_{\mu\nu}$, ρ_5 - are **PDF functions multiplied on corresponding kinematic prefactors**.

In the similar way, the *fragmentation correlator* Ξ is defined for the SIDIS process. It

contains information on the hadronization of the struck quark into a certain type of the hadron:

$$W^{\mu\nu} = \sum_{q, \bar{q}} e_q^2 \int d^4\mathbf{p} d^4\mathbf{k} \delta(\mathbf{p} + \mathbf{q} - \mathbf{k}) Tr[\Phi(\mathbf{p}, \mathbf{P}, \mathbf{S}) \gamma^\mu \Xi_{i,j}(\mathbf{k}, \mathbf{P}_h, \mathbf{S}_h) \gamma^\nu], \quad (2.28)$$

where $\Xi_{i,j}(\mathbf{k}, \mathbf{P}_h, \mathbf{S}_h)$ is the *fragmentation correlator*. It can be written as (see [37]):

$$\Xi_{i,j}(\mathbf{k}, \mathbf{P}_h, \mathbf{S}_h) = \frac{1}{(2\pi^4)} \int d^4\xi e^{i\mathbf{k}\xi} \langle \mathbf{0} | \psi_i(\xi) | \mathbf{P}_h, \mathbf{S}_h \rangle \langle \mathbf{P}_h, \mathbf{S}_h | \psi_j(\mathbf{0}) | \mathbf{0} \rangle, \quad (2.29)$$

where \mathbf{P}_h is four momentum of the hadron with spin \mathbf{S}_h . The parameters of the decomposition of fragmentation correlator are **FF functions multiplied on corresponding kinematic prefactors**.

Substituting the decomposed quark and fragmentation correlators Φ and Ξ in the hadronic tensor $W^{\mu\nu}$ and calculating the leptonic tensor $L_{\mu\nu}$ in eq. 2.20 using eq. 2.6, one obtains the equation for the SIDIS cross section:

$$\sigma_{SIDIS} \propto L_{\mu\nu} W^{\mu\nu} \propto \Phi \otimes \Xi \propto \sum_q \text{mod}(\phi_h, \phi_s) e_q^2 PDF(\mathbf{x}) \otimes \sigma^{eq \rightarrow e'q} \otimes FF(\mathbf{z}), \quad (2.30)$$

where $\text{mod}(\phi_h, \phi_s)$ presents an azimuthal modulation, sensitive to a set of corresponding transverse-momentum-dependent (TMD) distribution and fragmentation functions.

After integrating over the intrinsic quark transverse momentum k_T only three PDFs survive, that satisfy parity, hermicity, and time-reversal invariance. This leads to following description of the quark correlator:

$$\Phi = \frac{1}{2} (q(\mathbf{x}) \not{\mathbf{P}} + \lambda \Delta q(\mathbf{x}) \gamma_5 \not{\mathbf{P}} + \delta q(\mathbf{x}) \not{\mathbf{P}} \gamma_5 \not{\mathbf{S}}). \quad (2.31)$$

Parton distributions $q(\mathbf{x})$, $\Delta q(\mathbf{x})$, $\delta q(\mathbf{x})$ are connected with k_T -dependent PDF functions (see 2.16) through equations:

$$\begin{aligned} q(\mathbf{x}) &= \int dk_T^2 f_1(\mathbf{x}, k_T^2) \\ \Delta q(\mathbf{x}) (\Delta q(\mathbf{x})) &= \int dk_T^2 g_1(\mathbf{x}, k_T^2) \\ \delta q(\mathbf{x}) &= \int dk_T^2 h_1(\mathbf{x}, k_T^2). \end{aligned} \quad (2.32)$$

Accounting for the k_T dependence in the decomposition one can obtain 8 TMD PDF (see table 2.1) and 2 TMD FF for unpolarized or spinless final-state hadrons (see table 2.2). The various TMD functions reflect different correlations of spin of the target nucleon, spin of the quark, momentum of the quark and momentum of the hadron (for more details see [38]).

The correlations relate to density distributions of the quarks inside the nucleon. They can be drawn as blue areas in table for PDF function (see table. 2.1). The fragmentation functions can be found in table 2.2. At this moment it is hard to measure the polarization for the majority of produced particles. Thus, the FF functions are presented only for unpolarized state of the hadron.

N \ q	U	L	T
U	f_1		h_1^+
L		g_1	h_{1L}^+
T	f_{1T}^+	g_{1T}	$h_1^+ h_{1T}^+$

Table 2.1: The TMD PDF with various polarized states of the quark and the target nucleon. The correlations are shown as blue areas. Possible polarization states of probed quark are written in the row titled with letter "q". Polarization states of the target nucleon are written in the column titled with letter "N". The table is taken from [42]

H \ q	U	L	T
U	D_1		H_1^+

Table 2.2: The TMD FF with various polarized states of the quark and the hadron. Possible polarization states of fragmenting quark are written in the row titled with letter "q". Hadron polarization states are reduced to unpolarized one in the column with title "U". The table is taken from [42].

The TMD functions can be classified in terms of odd/even chirality and time-reversal nature in table 2.3.

T-even		T-odd	
chiral-even	chiral-odd	chiral-even	chiral-odd
q 			h_1^\perp  - 
Δq  - 	h_{1L}^\perp  - 		
g_{1T}  - 	h_{1T}^\perp  -  h_{1T}  - 	f_{1T}^\perp  - 	

Table 2.3: Classification of TMD functions by chirality and time-reversal nature. The plot is taken from [21].

In table 2.3 the nucleon and the quark are depicted as light and dark circles according to their *chirality* and *time-reversal nature*. Their spin orientations with respect to the virtual photon (photon comes from the left side of picture) are indicated with arrows.

Chiral-odd functions change the helicity of parton during reaction, while *chiral-even functions* conserve it. The diagrams of quark scattering with assigned helicity in initial and final state as "+" or "-" is shown in fig. 2.8.



Figure 2.8: Chirality of quark in DIS process. Right diagram indicates flip of helicity for initial and final states. The plot is taken from [21].

Due to the helicity conservation chiral-odd function should always come in pair with another chiral-odd function. This is the reason why the transversity function can not be measured ($d\sigma^\uparrow - d\sigma^\downarrow = 0$) in inclusive DIS reaction, which is sensitive to only one chirally-odd PDF, h_1 . The transversity function can be accessed via Drell-Yan process $p^\uparrow \bar{p}^\downarrow \rightarrow e^+ e^-$ with involving of the second distribution function or in SIDIS process by adding chiral-odd fragmentation function (see fig. 2.9).

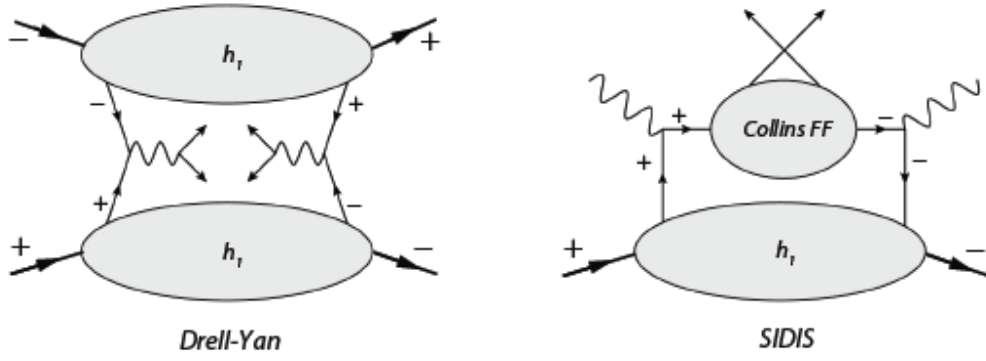


Figure 2.9: Quark helicity flip in Drell-Yan and SIDIS processes involving two chiral-odd functions. The plot is taken from [39]

Naive-T-odd functions change their sign by applying naive-time-reversal operation (T), while *naive-T-even functions* do not. Naive-time-reversal in QCD is time-reversal operation without interchanging of initial and final particles.

The example of a naive-T-odd function is the Sivers function. It corresponds to the correlation $\mathbf{S} \cdot (\mathbf{P} \times \mathbf{k}_T)$, where

nucleon momentum is T-odd, $T : \mathbf{P} \rightarrow -\mathbf{P}$,

quark transverse momentum is T-odd, $T : \mathbf{k}_T \rightarrow -\mathbf{k}_T$,

nucleon spin is T-odd, $T : \mathbf{S} \rightarrow -\mathbf{S}$.

Hence one has $\mathbf{S} \cdot (\mathbf{P} \times \mathbf{k}_T) = T_{odd} \cdot (T_{odd} \times T_{odd}) = T_{odd} \cdot T_{even} = T_{odd}$. As it was mentioned in sec. 2.1 the cross-section of the DIS process can be written in a set of structure functions. In a similar way the SIDIS cross-section can be written through structure functions and corresponding azimuthal modulations:

$$\begin{aligned}
\sigma_{SIDIS} = & F_{UU,T} + \varepsilon F_{UU,L} + \sqrt{2\varepsilon(1+\varepsilon)} \cos \phi_h F_{UU}^{\cos \phi_h} + \varepsilon \cos(2\phi_h) F_{UU}^{\cos(2\phi_h)} + \\
& \lambda_l \sqrt{2\varepsilon(1-\varepsilon)} \sin \phi_h F_{LU}^{\sin \phi_h} + \\
& S_{\parallel} [\sqrt{2\varepsilon(1+\varepsilon)} \sin \phi_h F_{UL}^{\sin \phi_h} + \varepsilon \sin(2\phi_h) F_{UL}^{\sin(2\phi_h)}] + \\
& S_{\perp} [\sin(\phi_h - \phi_S) (F_{UT,T}^{\sin(\phi_h - \phi_S)} + \varepsilon F_{UT,L}^{\sin(\phi_h - \phi_S)}) + \varepsilon \sin(\phi_h + \phi_S) F_{UT}^{\sin(\phi_h + \phi_S)} + \dots] + \\
& S_{\parallel} \lambda_l [\dots] + \\
& S_{\perp} \lambda_l [\dots],
\end{aligned} \tag{2.33}$$

where $F_{12,3}^{mod(\phi_h, \phi_S)}$ are the SIDIS structure functions. First, second and third subscripts define polarization of the beam, target and virtual photon respectively. Longitudinal and transverse spins of the target nucleon are denoted with S_{\parallel} , S_{\perp} respectively. Beam-spin helicity is denoted

with λ_i . The ratio ε of longitudinal and transverse photon flux is given by:

$$\varepsilon = \frac{1 - y - \frac{1}{4}\gamma^2 y^2}{1 - y + \frac{1}{2}y^2 + \frac{1}{4}\gamma^2 y^2}, \quad (2.34)$$

where variable γ is described by:

$$\frac{2Mx}{Q}. \quad (2.35)$$

Except of the first two structure functions each structure function presents due to the factorization a combination of convolutions of PDF and FF functions multiplied on kinematic prefactor and is sensitive to individual azimuthal modulation $\text{mod}(\phi_h, \phi_S)$, written as superscript of structure function:

$$\begin{aligned} F_{UU}^{\cos \phi_h} &\propto f_1 \otimes D_1, \\ F_{UU}^{\cos(2\phi_h)} &\propto h_1^\perp \otimes H_1^\perp, \\ F_{UT}^{\sin(\phi_h - \phi_S)} &\propto f_{1T}^\perp \otimes D_1, \\ F_{UT}^{\sin(\phi_h + \phi_S)} &\propto h_1 \otimes H_1^\perp, \\ &\dots \end{aligned} \quad (2.36)$$

Some of the SIDIS structure functions are discussed below.

2.5.1 Sivers effect

The Sivers effect creates azimuthal asymmetries in SIDIS hadron production with transversely polarized target. Its amplitude depends on the convolution of the unpolarized FF D_1 and the PDF f_{1T}^\perp , the Sivers function: $F_{UT}^{\sin(\phi_h - \phi_S)} \propto f_{1T}^\perp \otimes D_1$.

The Sivers function was introduced in 1990 in [18] and implies that unpolarized partons can have an asymmetric k_T distribution in a transversely polarized nucleon. It can be presented by the correlation $\mathbf{S} \cdot (\mathbf{P} \times \mathbf{k}_T)$ and can be written as the asymmetric part of the unpolarized quark distribution:

$$f_{1T}(x, k_T) = f_1(x, k_T) + \frac{1}{2} f_{1T}^\perp(x, k_T) \mathbf{S} \cdot (\mathbf{P} \times \mathbf{k}_T). \quad (2.37)$$

Eq. 2.37 shows that in the case of a transversely polarized nucleon the distribution of unpolarized quarks (which is initially axially symmetric) is distorted due to the correlation of the vectors written above.

It has been conjectured that DF functions can be written in impact parameter space [22].

The unpolarized distribution can be written as:

$$q(x) = \int d^2\vec{b}_T q(x, \vec{b}_T), \quad (2.38)$$

where \vec{b}_T is the impact parameter. In eq. 2.38 the impact dependent DF $q(x, \vec{b}_T)$ of unpolarized quarks is axial symmetric for unpolarized nucleons and nucleons with their spins aligned with the virtual-photon direction. In case of transversely polarized nucleons the distribution of unpolarized quarks (u_X and d_X) is distorted perpendicular to the spin and the momentum of the nucleon. The example of these distorted distributions can be found in fig. 2.10.

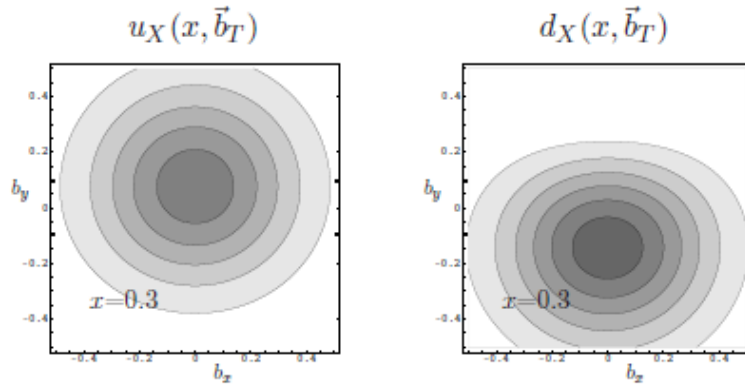


Figure 2.10: Impact parameter distributions of u and d quarks in a transversely polarized nucleon. Here, the nucleon spin is in x-direction, the virtual photon points into the page, z-direction. The plot is taken from [21].

This distortion is shown in fig. 2.10 for quark momentum fraction $x=0.3$. There is an enhancement of up-quark density in the top of the nucleon and its reduction in the bottom of the nucleon.

A possible explanation of the Sivers effect is shown in fig. 2.12. Here the spin of the nucleon is perpendicular to the page ($\phi_S = \frac{\pi}{2}$) and goes outwards. The orbital momentum of the u quark is positive. It causes a difference of the momentum fraction $x_{bottom} < x_{top}$ of the u-quark probed by the virtual photon in the top and bottom sides of the nucleon. This shift is reflected in the quark distribution as illustrated in fig. 2.11.

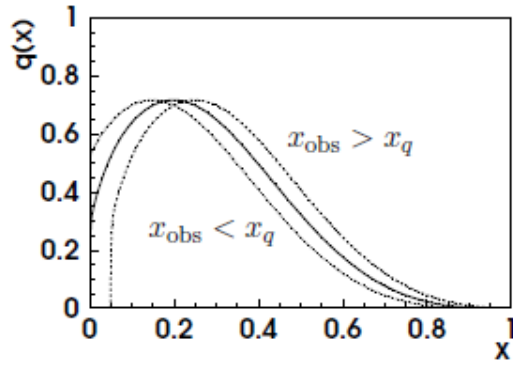


Figure 2.11: The shift in the quark distribution for u and d quarks caused by orbital momentum of the quark. The plot is taken from [21]

It means that more u quarks are probed in the top side of the nucleon than in the bottom side. The virtual photon scatters off a u quark that fragments then into a π^+ -meson. During the fragmentation process the struck quark is influenced by attractive forces (here denoted as Final State Interactions) of the color-charged nucleon remnant. The π^+ trajectory is deflected to the right in respect of the virtual-photon direction.

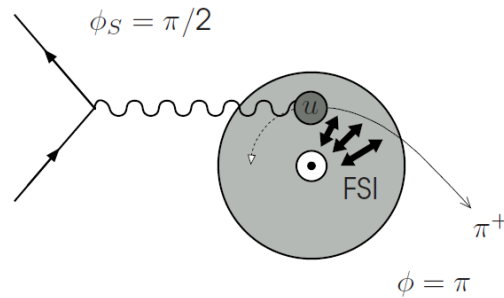


Figure 2.12: Siverts effect. Struck quark with positive orbital momentum is deflected by attractive forces (FSI) during fragmentation process. Figure is taken from [21]

Consequently, the produced π^+ is detected on the right side with $\frac{\pi}{2} < \phi_h < \pi$. Azimuthal modulation of Siverts function is $\sin(\phi_h - \phi_s)$ (see [18]). The measured Siverts amplitude at HERMES is presented on the right side of fig. 2.13. It is positive for π^+ meson in accordance with explanation above.

In fig. 2.10 right panel, the d-quark has a higher quark density in the bottom of the nucleon because of negative orbital momentum opposite to u-quark. One could think that d-quark should produce negative Siverts amplitude for π^- of the same size as u-quark fragmenting into π^- . Due to the factor of the quark charge e_q^2 (which is 4 times less for d quark, see eq. 2.15) and prevalence of u-quarks in the proton target ($p = |uud\rangle$) the d-quark does not play such a dominant role in π^- production. Instead, both u and d quarks contribute to the process and cancel each other making final Siverts amplitude consistent with zero.

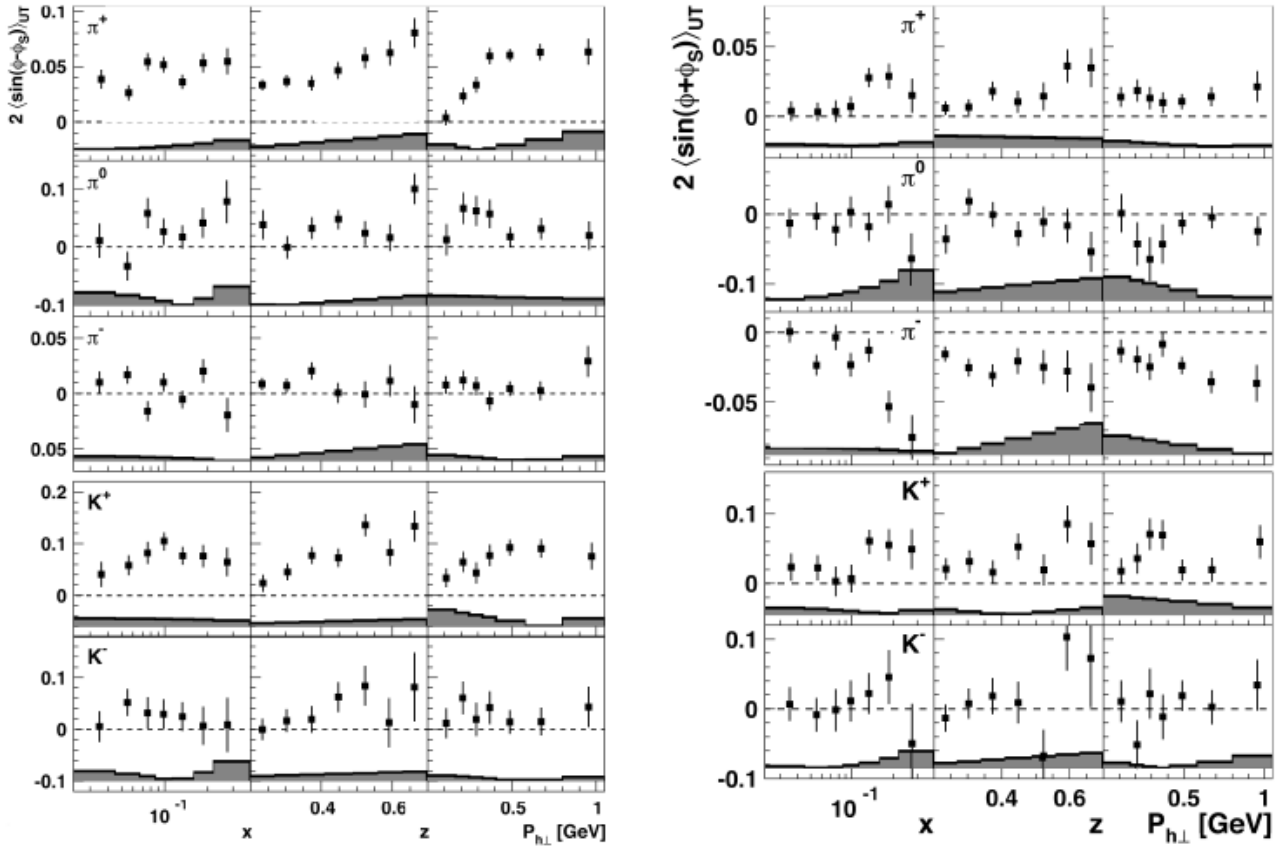


Figure 2.13: Sivers(left) and Collins(right) amplitudes for π^+ , π^- , π^0 , K^+ , K^- as a function of x , z or $P_{h\perp}$. The plots are taken from [24], [25].

2.5.2 Collins function

The Collins effect also produces azimuthal asymmetries in hadron production and it is dependent on the convolution of the PDF h_1 , transversity, and the FF H_1^\perp , the Collins function: $F_{UT}^{\sin(\phi_h+\phi_S)} \propto h_1 \otimes H_1^\perp$.

The Collins function was introduced in 1993 in [36] and corresponds to the correlation $\mathbf{s}_q \cdot (\mathbf{p}_q \times \mathbf{P}_{h\perp})$. It describes the fragmentation of transversely polarized quarks into unpolarized hadrons. The Collins function can be written as:

$$D_1^\uparrow(z, k_T) = D_1(z, k_T) + \frac{1}{2} H_1^\perp(z, k_T) \mathbf{s}_q \cdot (\mathbf{p}_q \times \mathbf{P}_{h\perp}). \quad (2.39)$$

The Collins effect can be understood through an explanation based on the string fragmentation model written in [26]. The explanation is shown in fig. 2.14 for two possible cases of orientation of target spin and lepton plane ($\phi_S = 0, \phi_S = \frac{\pi}{2}$).

According to this model the struck u quark reverses its spin component S_z in lepton-scattering plane after absorption of virtual photon (see fig. 2.14 (a)). When the nucleon breaks a quark-antiquark pair ($|d\bar{d}\rangle$) is produced (fig. 2.14 (b)) with quantum numbers of the vacuum,

$J^P = 0^+$. Positive parity of produced pair urges quark spins of the quark-antiquark pair to be aligned. Therefore orbital angular momentum for this quark-antiquark pair should be $L = 1$ in order to compensate its spin: $J = S + L$. This orbital angular momentum causes a deflection of the produced meson for the original quark direction, when struck u quark and \bar{d} quark from quark-antiquark pair are merged. Therefore the produced meson is deflected with respect to the lepton-scattering plane and depicted by open arrow (see fig. 2.14 (c)). A similar set of figures demonstrate the case when the target spin is perpendicular (fig. 2.14 (d)) to the scattering plane ($\phi_S = \frac{\pi}{2}$). In this case the spin of the quark does not change and the produced pion is deflected to the left side of the target spin (fig. 2.14 (e),(f)) compared to the virtual-photon direction. It results with a preference in $\phi_h = 0$.

The azimuthal modulation of Collins function is $\sin(\phi_h + \phi_S)$ and it is positive for both orientations of target spin described above. The explanation is consistent with positive amplitudes for π^+ observed at HERMES in fig. 2.13 right side. Also it can be proposed that favoured and disfavoured Collins FF have same amplitude but differ in sign, as a result of the large negative asymmetries observed for π^- .

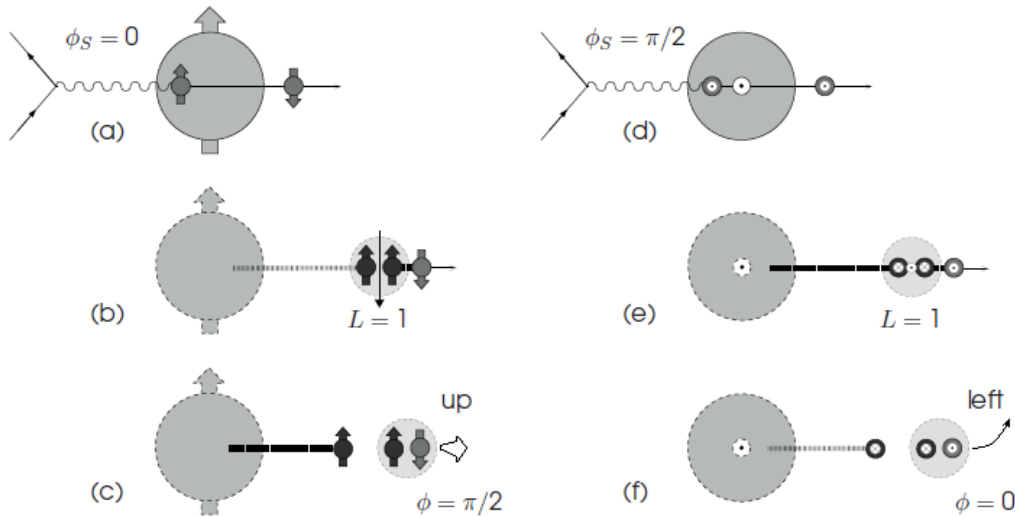


Figure 2.14: Collins effect

The results of the measurement of Sivers and Collins effects at HERMES are written in [54], [55] correspondingly. To access the Sivers function or Collins function one needs to know the D_1 FF or h_1 PDF which are convoluted with them. The D_1 can be obtained via inclusive hadron production in annihilation of leptons $e^+e^- \rightarrow \gamma(Z) \rightarrow h + X$. The transversity PDF h_1 can be extracted via Drell-Yan process $p^\uparrow \bar{p}^\downarrow \rightarrow e^+e^-$. The more detailed view on obtaining access to different functions one can find in [56].

2.6 Beam-spin effects

Probing an unpolarized proton with longitudinally polarized leptons one can gain insight into new correlations. Beam helicity effects were measured in [28], [30], [31] by HERMES, CLAS and COMPASS collaborations. In the case of longitudinally polarized beam and unpolarized target the SIDIS cross-section is presented by first two lines of eq. 2.33 . It contains contributions of two beam spin-independent structure functions $F_{UU}^{\cos \phi_h}$ and $F_{UU}^{\cos 2\phi_h}$, and beam spin-dependent structure function of interest $F_{LU}^{\sin \phi_h}$. All three are ϕ_h dependent. The $F_{UU}^{\cos 2\phi_h}$ modulation appears at leading twist due to intrinsic transverse motion of the quarks, while the $F_{UU}^{\cos \phi_h}$ modulation is formed by Boer-Mulders (see [35]) and Cahn (see [82]) effects. The Cahn effect is generated at subleading twist also by the non-zero intrinsic transverse motion of the quarks, while the Boer-Mulders effect originates at subleading twist from the correlation between quark spins and their own orbital angular momentum in an unpolarized nucleon. The $F_{UU}^{\cos 2\phi_h}$ and $F_{UU}^{\cos \phi_h}$ modulations were investigated at HERMES in [96] and are not the subject of interest in the present analysis. The $F_{LU}^{\sin \phi_h}$ is expressed in following FFs and PDFs (for details see [43]):

$$F_{LU}^{\sin \phi_h} = \frac{2M}{Q} \mathcal{C} \left[-\frac{\hat{\mathbf{h}} \cdot \mathbf{k}_T}{M_h} \left(x e H_1^\perp + \frac{M_h}{M} f_1 \frac{\tilde{G}^\perp}{z} \right) + \frac{\hat{\mathbf{h}} \cdot \mathbf{p}_T}{M} \left(x g^\perp D_1 + \frac{M_h}{M} h_1^\perp \frac{\tilde{E}}{z} \right) \right], \quad (2.40)$$

where $\hat{\mathbf{h}} = \mathbf{P}_{h\perp}/|\mathbf{P}_{h\perp}|$ and the notation:

$$\mathcal{C}[w f D] = x \sum_a e_a^2 \int d^2 \mathbf{p}_T d^2 \mathbf{k}_T \delta^{(2)}(\mathbf{p}_T - \mathbf{k}_T - \mathbf{P}_{h\perp}/z) w(\mathbf{p}_T, \mathbf{k}_T) f^a(x, p_T^2) D^a(z, k_T^2), \quad (2.41)$$

where $w(\mathbf{p}_T, \mathbf{k}_T)$ is an arbitrary function and the summation runs over quarks and antiquarks.

The structure function contains four convolutions:

- $e H_1^\perp$
usually called "Collins effect" demonstrated above and discussed in [46]
Here e is a twist-3 T-odd chiral-odd PDF, described in [46], [48]
 H_1^\perp is Collins twist-2 T-odd chiral-odd FF discussed in sec. 2.5
- $f_1 \tilde{G}^\perp$
where f_1 is the unpolarized twist-2 chiral-even T-even PDF. Integration over k_T gives unpolarized PDF $q(x)$
 \tilde{G}^\perp is a twist-3 T-odd FF and is poorly known.
- $g^\perp D_1$
where g^\perp is a twist-3 T-odd PDF analogous to the Sivers function
 D_1 is the unpolarized twist-2 FF
- $h_1^\perp \tilde{E}$

where h_1^\perp is the twist-2 T-odd chiral-odd "Boer Mulders" function explained in [44] analogous to Sivers function which describes correlation between quark transverse momentum and spin in an unpolarized nucleon

\tilde{E} - chiral-odd twist-3 FF function, discussed in [45], [46]

It is important to mention that twist-3 functions have no simple partonic interpretation due to the quark-gluon-quark interactions. Most of them are almost unknown and still not measured. The problematic point is that all four contributions described above are convolutions of a better known twist-2 and less-known twist-3 function.

Using eq. 2.40 and known F_{UU} from world data, one can access the DF and FF of interest, described in section 2.6. It is done through the specially constructed quantity, *asymmetry*. The beam-spin azimuthal asymmetry is defined as the difference of the cross sections for two opposite beam-spin states normalized to the sum of these cross sections:

$$A_{LU}(\phi_h) = \frac{1}{P_L} \frac{d\sigma^+(\phi_h) - d\sigma^-(\phi_h)}{d\sigma^+(\phi_h) + d\sigma^-(\phi_h)} = \frac{\sigma_{LU}}{\sigma_{UU}} = \frac{F_{LU}}{F_{UU}} = A_{LU}^{\sin\phi_h} \sin\phi_h, \text{ where} \quad (2.42)$$

$A_{LU}^{\sin\phi_h}$ is the amplitude of the beam-spin azimuthal asymmetry

Asymmetries are attractive to be measured because they are less sensitive to influence of acception, while its influence appears both in numerator and denominator of the asymmetry and is, therefore, reduced. Several sets of models were proposed by theorists for those functions included in beam spin asymmetry. It is not trivial to calculate all contributions simultaneously. Model calculations, sometimes, are not consistent with experimental results (see [49]) and can vary in a wide range of predictions because of using different model types (spectator, bag, di-quark models) and of making different assumptions (one photon approximation, Wandzura-Wilczek approximation, Gaussian ansatz, etc.), which simplify the cross section calculation. For example, two opposite models exist for the Collins function [53] and [46]. Also [46] and [47] estimate the major impact of certain convolutions differently.

Latest comparisons of HERMES results with theoretical models were made in [49], where the SIDIS cross-section was simplified through the Wandzura-Wilczek approximation [52], and contains only contributions $g^\perp D_1 + eH_1^\perp$ (see fig. 2.15). In this analysis more data was selected compared to [28]. Due to this fact it can be possible to increase the accuracy of comparison between theoretical models and experiment results.

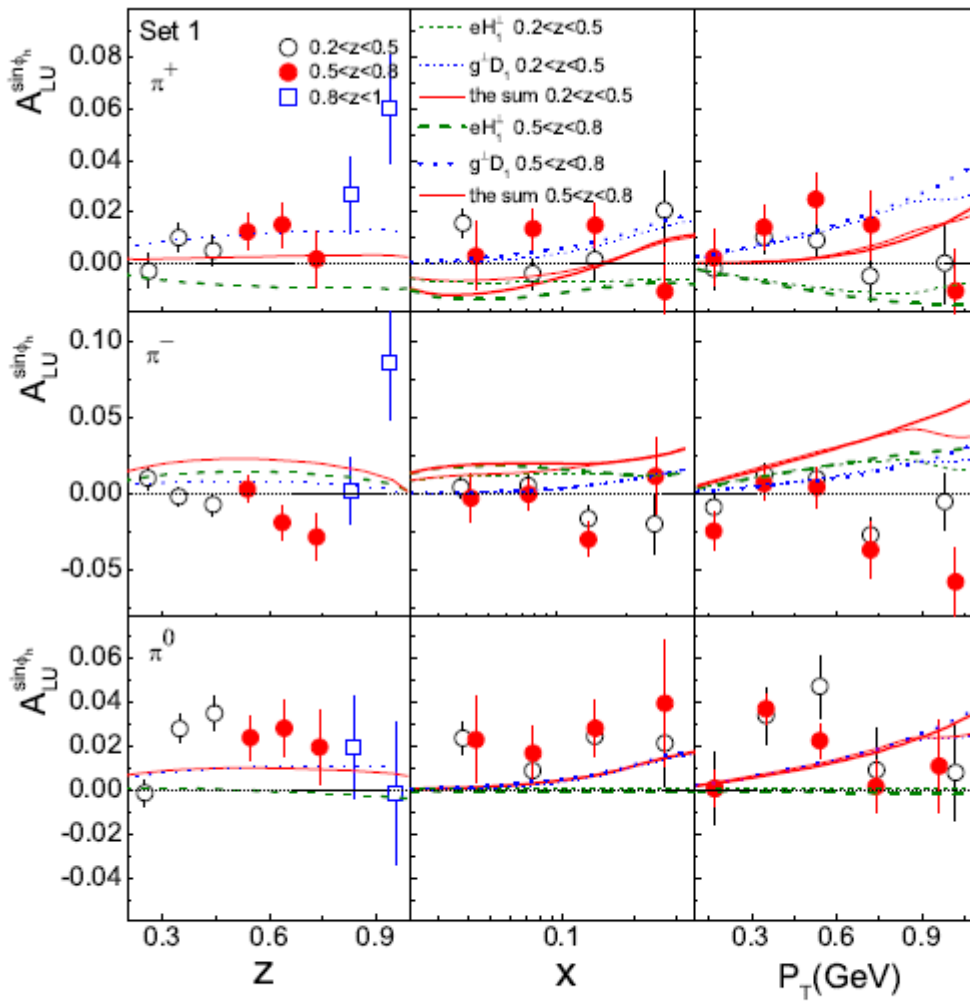


Figure 2.15: The beam SSAs $A_{LU}^{\sin\phi_h}$ for π^+ , π^- and π^0 productions in SIDIS at HERMES compared to theoretical models of TMD functions. Solid line shows total calculated value of $A_{LU}^{\sin\phi_h}$.

Chapter 3

The HERMES experiment at HERA

The HERMES experiment (HERA Measurement of Spin) was a fixed target experiment installed in the east hall of the storage-facility HERA (Hadron Elektron Ring Anlage) of the DESY accelerator. The experimental setup of HERA is presented in fig. 3.1. In the north and south halls of HERA, the H1 and ZEUS experiments were located, respectively. The HERA-B experiment was located in the west hall. The storage-facility HERA itself consisted of system made up from the two storage rings containing protons (with running energy $E=920$ GeV) and electrons ($E=27.6$ GeV). At the ZEUS and H1 experiments, the electron and proton beams were brought into collision, while at the HERMES and HERA-B experiments, the lepton and proton beams, respectively, were brought into collision with fixed targets.

The HERMES was designed for spin structure investigation. It allowed to reveal spin effects by using an longitudinally polarized beam and longitudinally or transversely polarized or unpolarized target.

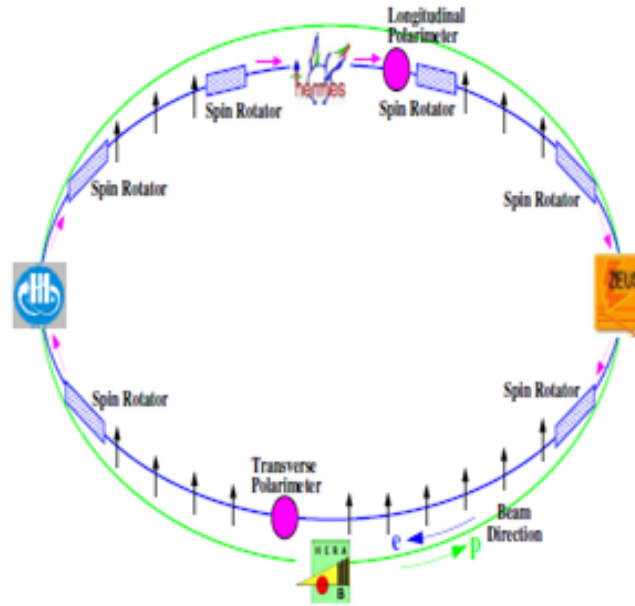


Figure 3.1: The HERA ring with HERMES, H1, ZEUS and HERA-B experiments. The spin orientation of the lepton beam is indicated by the arrows.

Longitudinal beam polarization was achieved through the usage of spin-rotators, consisting of six vertical and horizontal dipole magnets located before and after the HERMES spectrometer. The spin rotators rotated the polarization of the lepton beam from transverse to longitudinal one. Transverse beam polarization of leptons was achieved using the Sokolov-Ternov effect [57]. With the emission of synchrotron radiation there is a probability for electron to flip its spin, and the probability to flip its spin parallel to the magnetic field is higher than to flip its spin antiparallel to magnetic field. For positrons this is opposite.

3.1 Polarimeters

For the measurement of the beam polarization two polarimeters were used at HERMES. The longitudinal polarimeter (LPOL) [58] measured the longitudinal lepton polarization between the two spin rotators at HERMES. It used the asymmetry of integrated energy of Compton photons when scattering left or right circularly polarized laser light off a polarized lepton bunch. The transverse polarimeter (TPOL) measured the transverse lepton polarization [60] in the west part of the ring where no spin rotators were installed. It used the spatial up-down asymmetry of the back-scattered Compton photons for left or right circularly polarized laser light off a polarized lepton bunch. In fig. 3.2 one can see the coincident measurements of the polarimeters during the life time of the beam. They were used to check each other and decrease systematic uncertainty of the polarization.

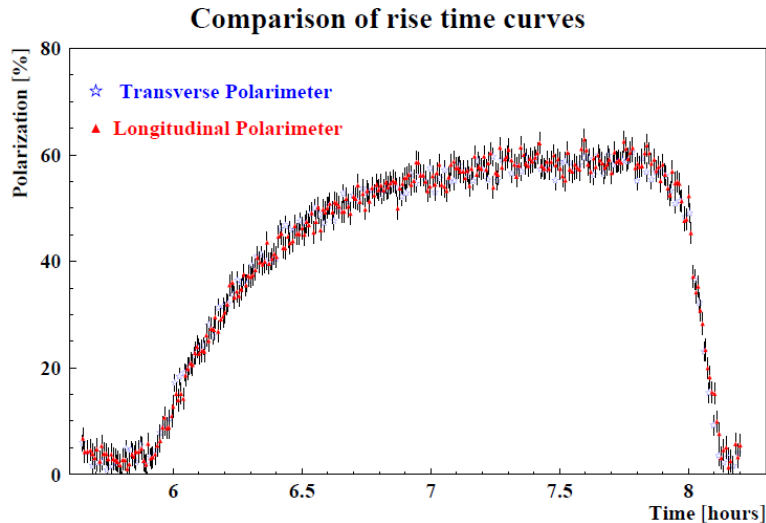


Figure 3.2: The beam polarization values measured by the longitudinal and transverse polarimeters.

3.2 The target

The target construction was designed in order to satisfy the following requirements: hold polarized or unpolarized gases and, according to the needs of other HERA experiments, to preserve the beam life time.

Gaseous target has the advantage of smaller dilution factor compared to solid or liquid targets and the possibility to provide higher polarization values. The HERMES target consisted of five main parts:

- Storage cell,
- Unpolarized gas feeding system (UGFS),
- Atomic beam source (ABS),
- Target gas analyzer (TGA),
- Breit-Rabi polarimeter (BRP),
- Target magnet.

The UGFS system was used instead of the ABS in order to provide measurements on an unpolarized targets. The following components (except of UFGS and target magnet) of transversely polarized target are shown in fig. 3.3.

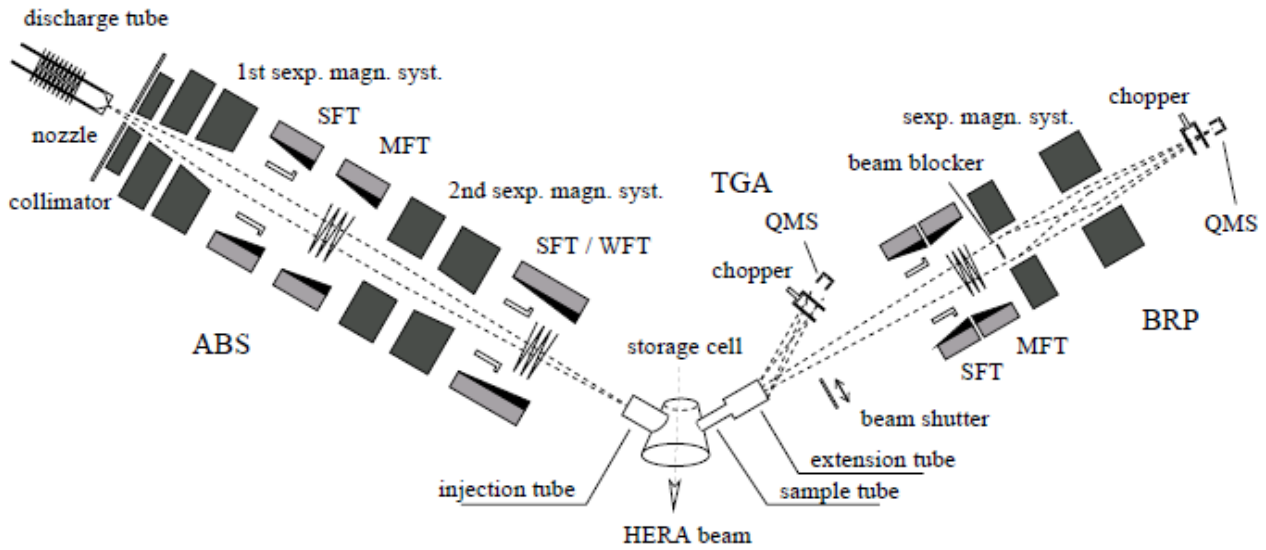


Figure 3.3: HERMES transversely polarized target and its main components.

A flow of the polarized hydrogen atoms was formed in the ABS and injected into the storage cell through which the HERA electron/positron beam was circulating. The TGA and the BRP continuously measured the state of the gas. The target magnet provided a holding field and prevented spin relaxation due to the decoupling of the magnetic moments of electrons and nucleons. In 2006 the target cell was exchanged to a shorter one and was shifted forward along the beam-axis.

Storage cell

The storage cell consisted of aluminum pipe 40 cm long with 75 μ m thick walls and elliptical cross sections of 9.8 mm and 29 mm diameters (see ref. [73]). For purity reasons the storage cell was directly attached to the beam pipe. A gas was injected in the center of the storage cell by the ABS and removed by two pumps situated at the ends of the cell. The gas density distribution had a triangular form with its maximum equal to $\sim 10^{14}$ nucleons/cm² at the center of cell. About 5% of the gas was drawn aside through sample tube to TGA and BRP for measurements of gas state. Two collimators were installed on the upstream of the target chamber to protect the cell from synchrotron radiation and the leptons scattered from the beam pipe walls. Additionally, the target was cooled down to the temperature of 100 K with a helium stream going through special inner rails (see fig. 3.4). The inner surface of the target cell storage was covered by special material called "Dryfilm" to minimize depolarization of the atoms in wall collisions.

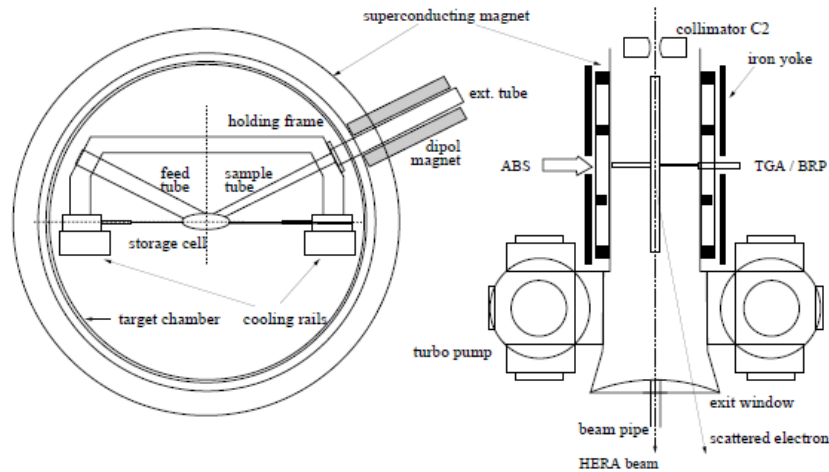


Figure 3.4: The HERMES storage cell

Unpolarized Gas Feeding System (UGFS)

The UGFS provided fill of the target storage with different unpolarized molecular gases (H, De, He, Ni, Ne, Kr and Xe). The maximum density of unpolarized gas was of the order of $\sim 10^{17}$ nucleons/cm² and was higher than the available polarized one ($\sim 10^{14}$ nucleons/cm²). However, the achievable level of gas density was limited by two factors:

- life time of the HERA lepton beam,
- dead-time of the data acquisition system (DAQ) which is proportional to the fraction of Möller electrons (see sec. 3.3.6).

These limitations led to typical gas density of $\sim 10^{16}$ nucleons/cm².

Atomic beam source (ABS)

The hydrogen and deuterium polarized atomic gases with polarization $\sim 97\%$ and injection rate 6.5×10^{16} nucleons/s were produced by the atomic beam source (see ref. [74]). The process of gas polarization had several steps. First, molecular hydrogen (deuterium) gas was dissociated by radio-frequency discharge into atomic gas with a dissociation fraction up to $\sim 80\%$. The dissociated gas flowed into the vacuum chamber which had the pumping system installed inside. It suppressed the scattering and recombination of atomic gas. Due to the magnetic field originating from the set of sextupole magnets atomic gas undergoes hyperfine splitting of its states with total spin $F=0$, $F=1$ (see fig. 3.5).

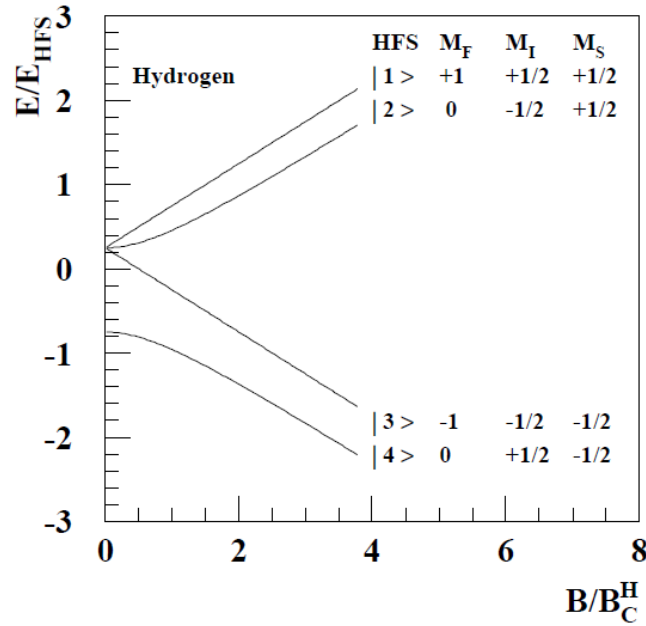


Figure 3.5: The energy splitting of hyperfine levels for hydrogen as function of the magnetic field.

The four states for hydrogen present combinations of the spin states of the nucleon $m_I = \pm \frac{1}{2}$ and the shell electron $m_S = \pm \frac{1}{2}$. The set of sextupole magnets focused states $|1\rangle$ and $|2\rangle$ with the same electron spin while the other two were deflected. Weak field transition (WFT) and strong field transition (SFT) radio-frequency units interchanged occupation numbers of $|1\rangle$, $|3\rangle$ and $|2\rangle$, $|4\rangle$ respectively. It gave possibility to produce two states $|1\rangle + |4\rangle$ and $|2\rangle + |3\rangle$. The states have the same atomic spin orientation $+\frac{1}{2}$ or $-\frac{1}{2}$ and zero electron polarization. Finally, atoms of the polarized gas were injected into the target storage cell. Deuterium is polarized in the similar way. For the longitudinally polarized target, the nucleon spin state was flipped every 60 s, while for the transversely polarized target it was increased up to 90 s. In this analysis, integrated transversely polarized data was used as effectively unpolarized target.

Target gas analyzer (TGA)

Measurements of the gas polarization in the storage cell were necessary for the target spin dependent analyzes. For this purpose a TGA (see ref. [75]) and BRP were installed. A TGA had the quadrupole mass spectrometer (QMS), a chopper and a channel electron multiplier (CEM). The TGA was tilted under an angle of 7° with respect to the sampling tube in order to avoid interference with the beam going to the BRP. The atomic and molecular gas entering the TGA were ionized by additional electron beam. Then ions were filtered by the QMS and detected by CEM. The chopper separated the gas flow in front of the QMS into portions. The gas polarization value in the storage cell was affected by the recombination of atoms into molecules due to the wall collisions with flow ϕ_r , the flow of undissociated gas after the dissociation chamber (ballistic flow of gas) ϕ_{ball} and the flow of the residual molecular gas in

the target storage ϕ_{res} . Together with atomic flow ϕ_a the full gas flow for the storage cell reads:

$$\phi_{tot} = \phi_a + \phi_r + \phi_{ball} + \phi_{res}. \quad (3.1)$$

The TGA measured the degree of dissociation of the target gas α_{TGA} through the flow rates for atoms ϕ_a and molecules $\phi_m = \phi_r + \phi_{ball} + \phi_{res}$. Together with calibration measurements [76], the degree of dissociation in absence of recombination, α_0 , and the degree of atoms surviving recombination, α_r , could be obtained:

$$\left\{ \begin{array}{l} \alpha_{TGA} = \frac{\phi_a}{\phi_a + \phi_m}, \\ \alpha_0 = \frac{\phi_a + \phi_r}{\phi_{tot}}, \\ \alpha_r = \frac{\phi_a}{\phi_a + \phi_r}. \end{array} \right. \quad (3.2)$$

Quantities α_r , α_{TGA} and α_0 were used later to determine the density-averaged nuclear polarization P_T in storage cell.

Breit-Rabi Polarimeter

In addition to the measurements of the gas polarization with the TGA, the second measuring device, the BRP was installed at HERMES [77]. It consisted of high transition radio-frequency units SFT and MFT, a QMS, a chopper, and a sextupole magnet system. As in case of the TGA, the gas entered to BRP through a sample tube and passed through SFT and MFT. Frequency units were tuned for exchange between different hyperfine states. The sextupole magnet system focused atoms with $m_S = +\frac{1}{2}$ and filtered out the atoms with $m_S = -\frac{1}{2}$. The beam blocker was installed in front of the first magnet in order to reject those atoms that were towards the symmetry axis of the magnets and were not affected by the magnet field (which is zero at the symmetry axis). The BRP used the same principles of particle detection as the TGA. It also contained the QMS and the chopper. In contrast to TGA, the BRP detected only atoms. Measurement of hyperfine state populations of atoms provided access to the atomic polarization P_a . Corrections calculated in Monte Carlo simulations were to be applied to relate P_a in the BRP with P_a in the center of the target. Combining measurements from TGA and BRP one could obtain the average polarization of the target gas:

$$P_{target} = \alpha_0[\alpha_r + \alpha_0(1 - \alpha_r)\beta]P_a, \text{ where} \quad (3.3)$$

$\beta = \frac{P_m}{P_a}$ is the ratio of the nuclear polarization of molecules produced by the recombination process to the nuclear polarization of atoms. Because the BRP was only able to measure atomic polarization, it was solely possible to restrict the β parameter to a range $\beta = [0.45; 0.83]$. The

limits of range were obtained by additional measurements at higher temperatures under special assumptions (see ref. [78] for more details).

Target Magnet

The target magnet surrounding the storage cell was holding the target polarization provided by ABS. The magnetic field decreased the spin relaxation of atoms due to the splitting of hyperfine energy levels. For the years 1997-2000, where the target was longitudinally polarized, the target magnet contained a set of superconducting magnet coils. In the period 2002-2005 the polarization was switched to the transverse one and the magnet was changed to the conventional dipole magnet.

3.3 Spectrometer

At the HERMES experiment a fixed gaseous target was used, the particles created from the interaction of the lepton beam with the target were detected by a forward spectrometer (see fig. 3.6). The latter consisted of various sets of detectors in forward-beam direction, because the majority of produced particles in high-energy collisions is emitted coincidentally with the beam direction.

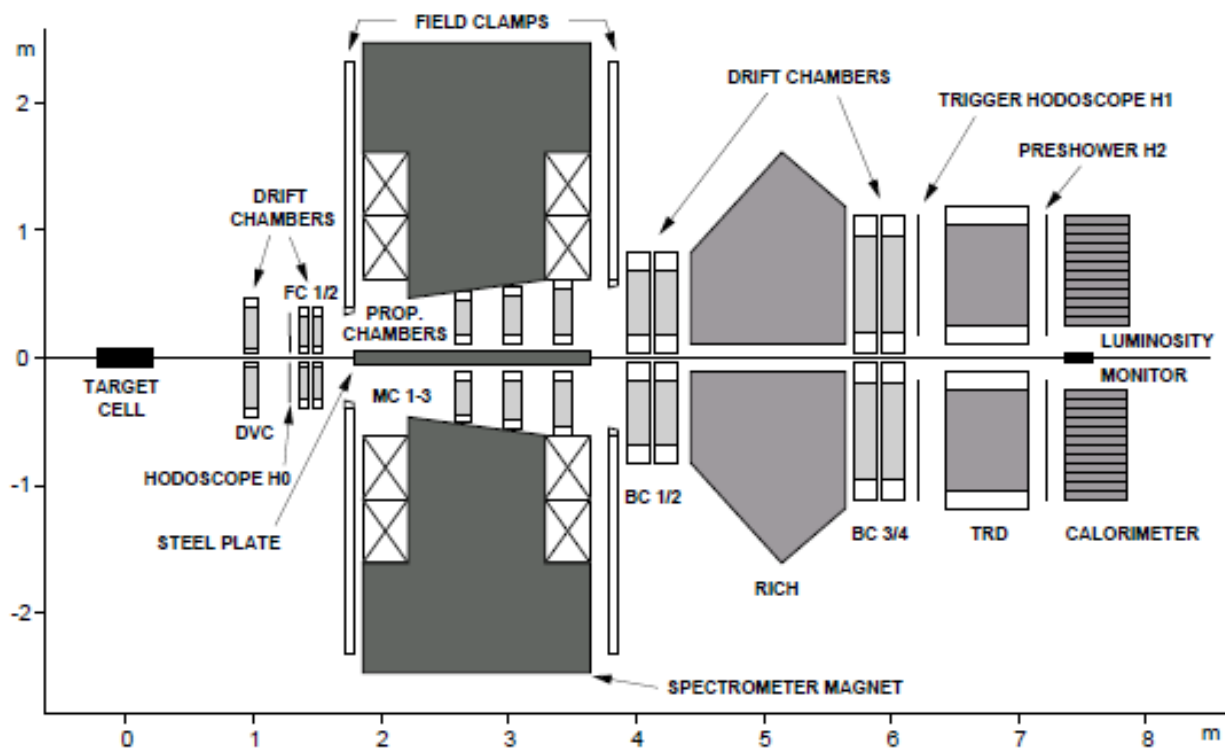


Figure 3.6: The HERMES spectrometer.

The detailed description of the several spectrometer components is presented below.

3.3.1 Tracking detectors

The tracking system consisted of gas wire chambers, drifting chambers which were used to determine coordinates of a particle track. Bending of particle tracks caused by the spectrometer magnet was used to calculate the momentum of the particle.

Drift chambers

The tracking system contained sets of wire chambers which took information about interaction points before (FC) [61] and after (BC) [62] the spectrometer magnet. They used gas ionization caused by charged particles. The ionization produced charges inside the plane volume which drifted to the wires with potential opposite to their charge. Two FC_s were installed in front of the spectrometer magnet. Each had 2×3 planes perpendicular to the beam. Two of them were located in the vertical plane, four of them were tilted by $\pm 30^\circ$. The FC_s were designed in order to reconstruct the part of the track before its bending in the the magnetic field. Additional chambers, the DVC_s, were installed in front of FC_s in order to improve the track reconstruction, in particular the vertex reconstruction. Two BC_s were installed after the spectrometer magnet in order to reconstruct the part of the track after its bending in the the magnetic field, they also have similar construction to FC_s.

Proportional chambers

Together with FC_s, BC_s and DVC_s, three *proportional* chambers (MC_s) [63] were located inside the spectrometer magnet. They offered the possibility to detect the low-momentum particles that did not reach the back end of the spectrometer.

3.3.2 Transition radiation monitor (TRD)

The TRD [64] at HERMES was used for the discrimination of hadrons and leptons. It contained six modules (see fig. 3.7) made up from the polypropylene fibers and surrounded by the gas layers Xe and CH₄. When a particle traversed the boundary of the gas and fiber surfaces it had a probability to emit an electromagnetic radiation (*transition radiation*) due to the Coulomb field continuity at the boundary of two dielectric materials.

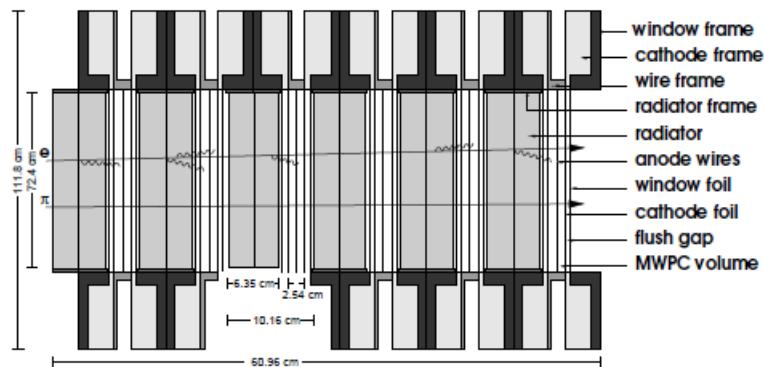


Figure 3.7: The upper TRD half.

The probability to radiate the transition radiation is proportional to the Lorentz factor γ , which is different for hadrons ($\gamma \approx 10^1$) and leptons ($\gamma \approx 10^4$). It gives a possibility to separate leptons from hadrons.

3.3.3 The preshower detector

The preshower detector was a scintillating lead glass detector, which was installed behind a thick 11 mm lead plate. It consisted of 42 vertical panels with a total area of $9.3 \times 91 \text{ cm}^2$. Charged particles were deflected by the Coulomb field inside of the lead glass and detector material. Particle acceleration (deflection) gave rise to Bremsstrahlung radiation. The emitted photon could then converge to electron-positron pair. This whole process led to the evolution of particle showers inside the detector. Electrons and positrons are lighter than hadrons and therefore were strongly deflected inside the lead plate. It resulted in a larger energy deposit (shower) left by the particle. This fact provided a possibility to distinguish electrons and positrons from hadrons. The preshower also contributes in detecting of photons.

3.3.4 The calorimeter

The calorimeter [65] was installed right after the preshower detector. The half of calorimeter contained 42×10 array of lead-blocks, each of them had a cross section of $9 \times 9 \text{ cm}^2$ and was 50 cm long. The length of the calorimeter block corresponds to 18 radiation lengths and assured that particle showers initiated by leptons, were fully contained in the blocks. Particle showers produced Cherenkov light in the lead glass blocks, which was collected by photon multiplier tubes (PMTs), attached at the outer ends of the blocks. Hadrons left only a small part of their energy under the action of the ionization process in the detector material, while leptons were almost totally absorbed. The ratio of the particle's energy deposit to its momentum $\frac{E}{P}$ allowed the separation of hadrons and leptons. The ratio for leptons was around 1, while for hadrons this ratio was less than 1. The calorimeter and preshower detectors are shown in fig. 3.8

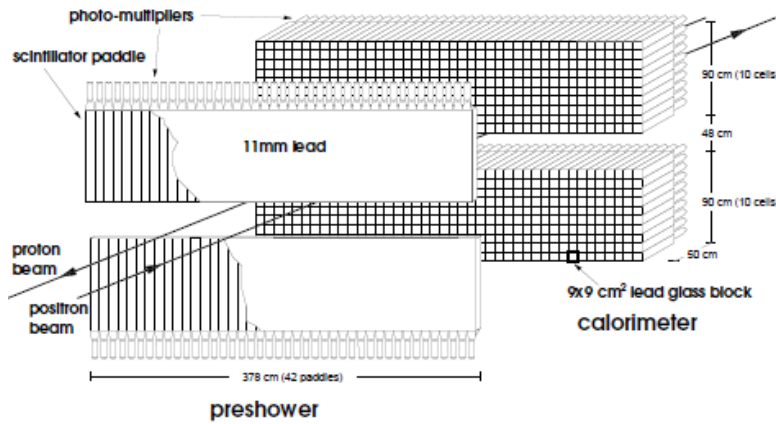


Figure 3.8: Preshower detector and calorimeter at HERMES.

In addition to charged particles, the calorimeter detected photons and reconstructed their energy and position.

3.3.5 Ring imaging Cherenkov detector

The threshold Cherenkov detector was exchanged by the ring imaging Cherenkov detector (RICH) [66] in 1998 to improve hadron identification. Both detectors used Cherenkov radiation, which is emitted, when a particle moves through material with a speed higher than the speed of light in this material. Moving particle emits photons in a cone with an opening angle θ when it exceeds momentum threshold p_{thres} :

$$\begin{cases} p > p_{thres} = \frac{1}{\sqrt{n^2 - 1}}, \\ \theta = \arccos\left(\frac{1}{\beta n}\right), \text{ where} \end{cases} \quad (3.4)$$

$\beta = \sqrt{\frac{v^2}{c^2}}$ is a particle velocity, and n is the refraction index of material.

Using threshold Cherenkov detector it was only possible to distinguish leptons and pions. The principle was improved in RICH detector and allowed to distinguish additionally to pions and leptons, also kaons and (anti)protons. The kinematic range of detected pions was also increased. One half the RICH detector is presented in fig. 3.9. Particles passed radiator made of silica aerogel SiO_2 ($n=1.0304$) and then passed through a second radiator with a heavy gas C_4H_{10} ($n=1.0013$). Emitted Cherenkov photons were focused by the spherical mirror to the PMT matrix. They left image-circles on the matrix (see fig. 3.10 a)). The radius of the circle corresponds to the opening angle θ .

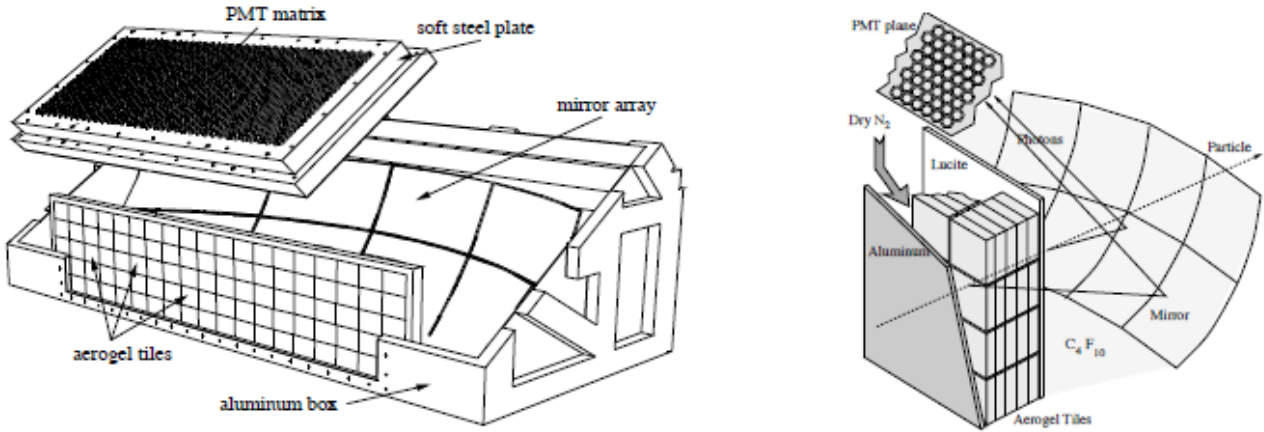


Figure 3.9: The HERMES RICH detector. Schematic view of the upper half of RICH.

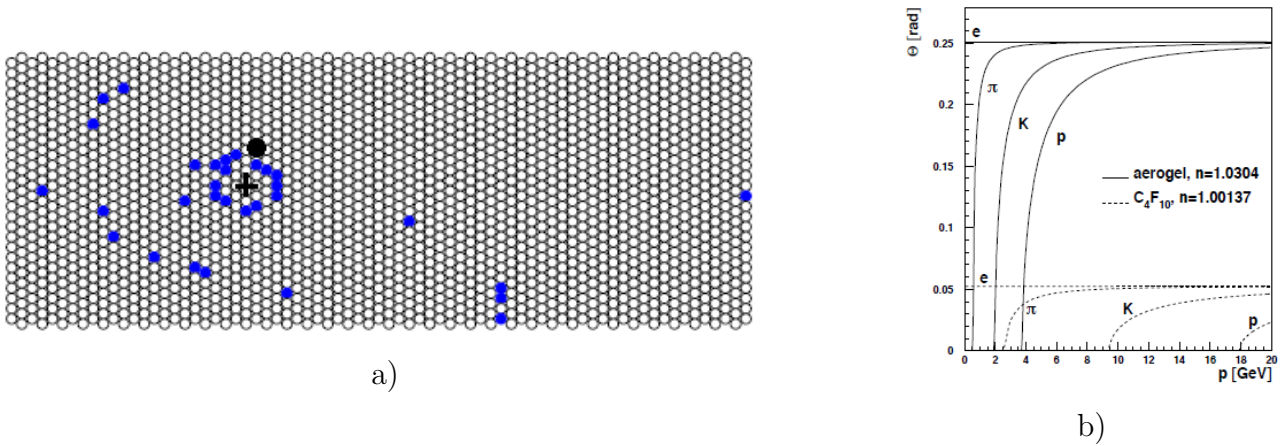


Figure 3.10: a) Two reconstructed centers of circles left by a hadron track on PMT matrix, o corresponds to the center of the circle in aerogel, + corresponds to the center of the circle in C_4H_{10} b) The momentum dependence of the Cherenkov opening angle θ .

Different radiator materials gave a possibility to produce image-circles of charged hadrons in a wide momentum range. In fig. 3.10 b) the dependence of the opening angle on the particle momentum in aerogel and C_4H_{10} is shown. The particle velocity can be estimated through the opening angle θ (see eq. 3.4). Using the value of the particle momentum obtained under the action of the magnetic field, one can determine the particle mass and therefore, the particle type. The reconstruction of the angle θ is affected by acceptance effects, background processes, detector noise, and the geometrical asymmetry of the focusing mirror. Several reconstruction algorithms were developed to improve the hadron separation efficiency.

The *Indirect Ray Tracing* (IRT) algorithm is described in [67]. Its main idea is the following: the opening angle was calculated for a given track for each hit in the PMT matrix. The mean of the calculated θ distribution was compared to the theoretical angle θ_{theory} calculated

from the particle hypotheses: pion, kaon, and proton. The most probable particle type was determined from the conditional probabilities that the detected hit pattern was generated by the hypothetical particle. Applying likelihoods for two radiators an overall conditional probability was determined.

The *Direct Ray Tracing* (DRT) is explained in [68]. In this method, the particle type was determined by comparison of the detected hit pattern in the PMT matrix to the simulated pattern in Monte Carlo (MC) based calculations. The contribution from background processes and instrumental noise could also be estimated via the MC simulation.

The *EVenT-level (EVT) algorithm* is detailed in [69]. Overlapping of circles-images in PMT from two tracks could lead to misidentification of particles. It can happen when two tracks are close to each other. The EVT algorithm was developed to decrease the identification inefficiency in this case. It is very important in analyses that are sensitive to hadron yields of different types. Therefore, the EVT algorithm was chosen for this analysis. It was developed from the DRT algorithm. The main difference is that EVT looked at each event as a whole and used the topology of event tracks (it distinguishes to which half each track belongs), while DRT looked at individual tracks. The EVT reduced to the DRT when only one track in the event was detected.

P-matrices. For each algorithm the P-matrix was evaluated to decrease the RICH inefficiency (*RICH unfolding procedure*). The matrix determines the conditional probability P_t^r that a given hadron of true type t was identified as a hadron of type r. It describes the contamination and the inefficiency of the measured hadron yields. It relates measured yields I of type r with true yields T of type t:

$$\begin{pmatrix} I_\pi \\ I_K \\ I_p \\ I_X \end{pmatrix} = \begin{pmatrix} P_\pi^\pi & P_K^\pi & P_p^\pi \\ P_\pi^K & P_K^K & P_p^K \\ P_\pi^P & P_K^P & P_p^P \\ P_\pi^X & P_K^X & P_p^X \end{pmatrix} \cdot \begin{pmatrix} T_\pi \\ T_K \\ T_p \end{pmatrix}. \quad (3.5)$$

In order to obtain true yields from measured ones, one can truncate the row containing P_T^X from the P-matrix ($P \rightarrow P'$), invert it and apply it to the measured yields:

$$T = P'^{-1}I. \quad (3.6)$$

The P-matrix depends on the track momentum and number of tracks presented in the detector half.. An overlap of the PMT patterns of different tracks is probable, when several particles are detected by one RICH half. It is illustrated in fig. 3.11, conditional probabilities of given hadron of true type h_{true} to be identified as a pion, kaon or (anti)proton, are shown.

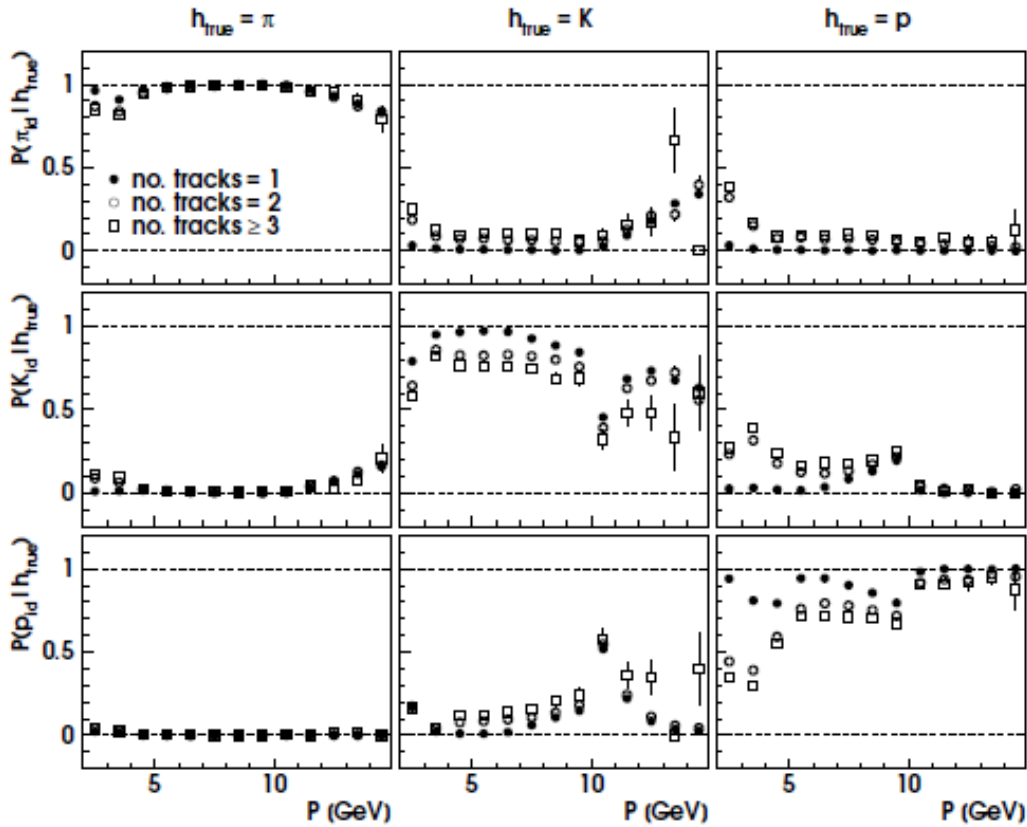


Figure 3.11: The P-matrix dependence on the particle momentum and the number of detected tracks in one detector half obtained from a MC simulation.

P-matrices were produced via MC simulations using both Pythia and disNG generators. Matrices were tuned to the HERMES kinematics using decay particle yields, hadron and electron yields (see ref. [70]). Tuning was made by adjusting mirror roughness parameters of the RICH. In the present analysis one of the matrices was used to provide the central value, while the others were used for the estimation of systematic uncertainties. For the two different experimental geometries of the data taking periods 1998-2005 and 2006-2007, four matrices were produced:

- center= $disNG_{ownBkg}$, a disNG MC sample with background estimation evaluated from the sample itself;
- $disNG_{dataBkg}$, same as the disNG MC own background sample, but extracted from data;
- $disNG_{pythia}$, same as the disNG MC own background sample, but extracted from Pythia MC sample;
- $pythia_{disngBkg}$, Pythia MC sample own background sample, but extracted from disNG MC sample;

The values of all four matrices are presented in fig. 3.12. All four samples show very compatible results.

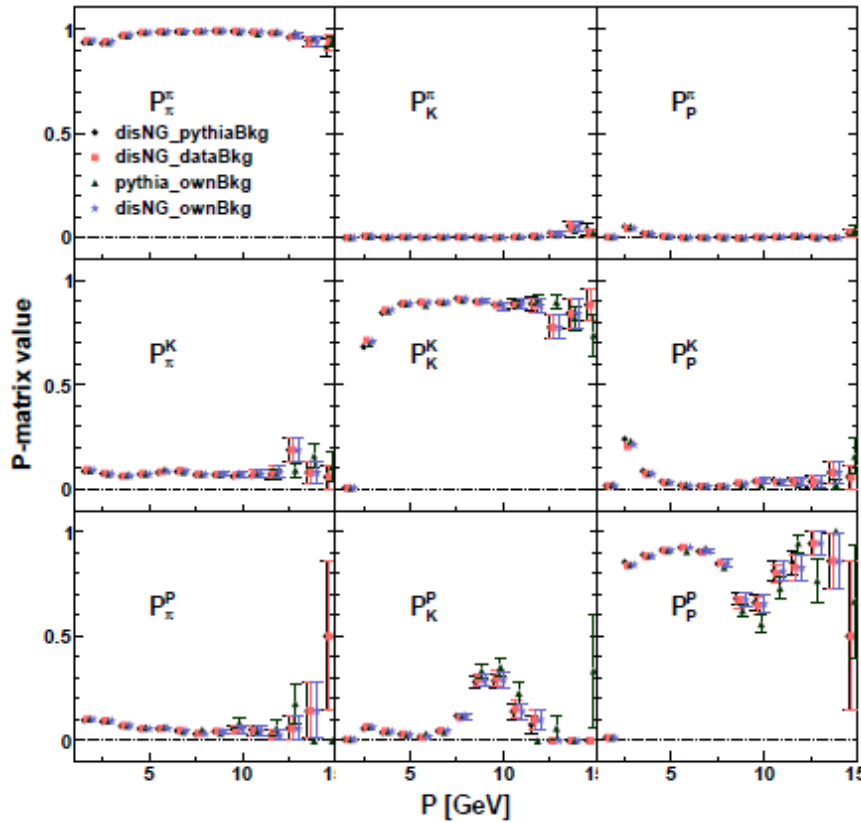


Figure 3.12: P-matrices for the EVT method for three or more tracks in one of the detector halves.

The EVT algorithm shows better identification compared to IRT (for more details see ref. [69]). It has higher efficiency and lower contamination in almost all kinematic bins. An exception is the region of 8-12 GeV for protons, which overlaps with the kaon C_4H_{10} threshold.

3.3.6 Luminosity monitor

Luminosity measurements provide a possibility to calculate cross-sections or cross-section asymmetries. They can be used to normalize particle yields. The luminosity is the product of the beam current and target density integrated over the measurement time. The normalization of particle yields can be done using luminosity monitor measurements or, alternatively, DIS events.

The luminosity monitor counted coincident particle pairs coming from Möller scattering ($e^-e^- \rightarrow e^-e^-$) for the electron beam case, or Bhabba scattering ($e^+e^- \rightarrow e^+e^-$) for the positron beam. Also the annihilation process ($e^+e^- \rightarrow \gamma\gamma$) contributed to the positron beam case. The luminosity monitor consisted of two calorimeters, which measured the simultaneous response from particle pairs with a lower energy threshold of 4.5 GeV in order to suppress background. Each calorimeter consisted of 3×4 array of lead-glass blocks with a $2.2 \times 2.2 \text{ cm}^2$ cross section area and 20 cm length.

Measurements of absolute luminosity were sensitive to the geometry of the experiment. The geometry was taken into account with the proportionality constant C_{lumi} , which varies for different years of data taking period.

Since this analysis deals with asymmetries (see eq. 4.9), only the relative luminosity plays a role. This fact essentially decreases the systematic uncertainty and also gives a possibility to use DIS events for normalization.

3.3.7 Hodoscopes

Three scintillator detectors, *hodoscopes* (H0, H1, H2), were installed at HERMES to measure scintillating light left by particles inside the material. The PMTs were connected to the detectors and converged the light signal coming from hodoscopes into electric ones. Each half of H0 was made from one single sheet of scintillator, while H1 and H2 consisted of an array of panels. Hodoscopes are part of *trigger* system, which can distinguish between events of specific physics interest from the background noise, and switch on or switch off the readout of spectrometer detectors. The most important physics trigger for this analysis is the DIS candidate-trigger (trigger-21), which indicates signals in the three hodoscopes and in the calorimeter coinciding with the HERA lepton bunch. The H0 was installed to suppress trigger signals initiated by a backward going particles originating from the proton beam. The H1 was located in front of the TRD detector. It had a function to prevent the shower to be determined as a lepton signal, which was initiated by the photon in the preshower and calorimeter.

3.4 Particle identification

Particle identification (PID) was performed by four detectors. By means of the transition radiation detector (TRD), the preshower, and the calorimeter the lepton-hadron separation was achieved (see fig. 3.13). Further separation of charged pions, kaons and (anti)protons was performed by Ring Imaging Cherenkov detector (RICH). It was installed in 1998 in order to replace the threshold Cherenkov detector.

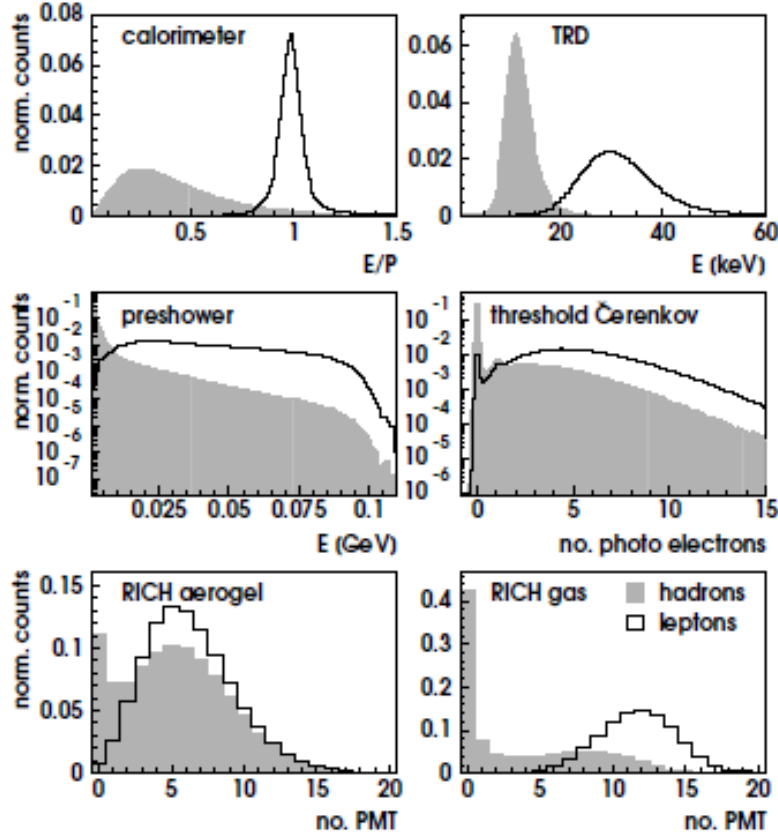


Figure 3.13: Signal responses of the different PID detectors for hadrons and leptons.

The combination of PID detectors could significantly improve particle identification compared to using only one PID detector. The conditional probability $P_i^{l(h)}$ represents the probability with which a lepton (l) or a hadron (h) produces measured signal in the PID detector i . The logarithm of the ratio $\frac{P_i^l}{P_i^h}$ was calculated for each detector or its combinations and named PID value. In this analysis, value PID_3 corresponds to combined responses from the preshower, the calorimeter, and the RICH detector while PID_5 is related to the TRD detector. PID_3 and PID_5 were determined for each detected particle:

$$\left\{ \begin{array}{l} PID_3 = \log_{10} \frac{P_{presh}^l P_{calo}^l P_{RICH}^l}{P_{presh}^h P_{calo}^h P_{RICH}^h}, \\ PID_5 = \log_{10} \frac{\prod_{m=1}^6 P_{TRDm}^l}{\prod_{m=1}^6 P_{TRDm}^h}, \\ PID_3 + PID_5 - \log_{10} \frac{\Phi^l}{\Phi^h} = \log_{10} \frac{P_i^l}{P_i^h}, \text{ where} \end{array} \right. \quad (3.7)$$

$\Phi^{l(h)}$ are lepton (hadron) fluxes, which can be calculated iteratively. The product in the equation for PID_5 runs up to six, which corresponds to the amount of modules in TRD.

The separation of hadrons and leptons performed by PID values is shown in fig. 3.14.

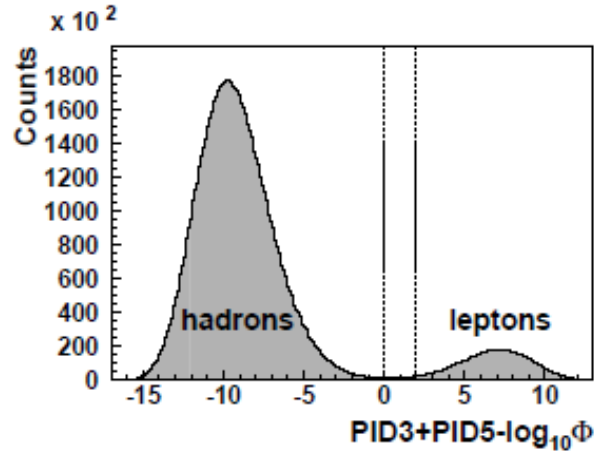


Figure 3.14: The $PID_3 + PID_5 - \log_{10}\Phi$ distribution shows clear separation of leptons from hadrons. The dashed vertical lines show chosen limits for lepton-hadron separation.

Strict cuts for combined PID quantities can be chosen:

$$\begin{cases} PID_3 + PID_5 - \lg \frac{\Phi^l}{\Phi^h} > 2 & : \text{leptons,} \\ PID_3 + PID_5 - \lg \frac{\Phi^l}{\Phi^h} < 0 & : \text{hadrons.} \end{cases} \quad (3.8)$$

It allowed lepton identification with an efficiency of 98% and a hadron contamination less than 1%.

3.5 Data acquisition

The electronic readout was attached to each detector in order to provide digitization of an analogous signal. Information about detectors, triggers and other experimental parameters were saved every few minutes. It was called by *slow-control data*: the information about beam polarization measurements, operating voltages, etc. The HERMES Decoding software (HDC) was designed to map raw data into physically meaningful quantities. The calibration signals collected by ADC (Analog to Digital Converter) were used to convert detector signals into energy measurements, while the TDC (Time to Digital Converter) information helped to convert signals into drift times and consequently to distances.

Decoded information synchronized with slow-control data was stored in ADAMO tables as ready-to-use data (see ref. [79]). It was regularly updated by adding new information on spectrometer calibration and tracking efficiencies. Versions of the data production have special names, e.g. 00e1 or 06f1. The first two digits refer to the year of data recording. The letter

encodes the version of the data with newly applied calibration information and the last digit increases when new slow-control data information is known. In version d1 new reconstruction algorithm HTC was applied. It used the Kalman filter method [80] and took into account the target magnetic field, the beam position, and spectrometer materials. The HTC uses probability technique and binds the track of the particle to the beam (one-track-to-beam) or two tracks with each other (two-track vertex). The HTC provides more accurate parameters of the track: momentum, azimuthal and polar angles compared to the previously used HERMES ReConstruction code (HRC).

Tracking information was written in a special format μDST and was organized in three data levels: runs, bursts and events. The event level contained information on the momentum, angles of the track, and the PID value. All information recorded in the period of 10 s form a *burst*. It gave a possibility to choose quickly only safe data according to *bitmask*. The bitmask contained the spectrometer criteria, which are to be verified for each recorded burst. The run is presented by a collection of bursts written to around a 500 MB volume. It gave a possibility to split raw data into small pieces. Usually, special runs can indicate the beginning of the data taking periods with new conditions (new gas in target, changing from negative to positive beam polarization).

Chapter 4

Data Analysis

In this chapter the selection of candidate events will be shown. Using slow control data (see sec. 3.5) only safely recorded data is selected. This is done with the use of status bits in sec. 4.1. After this, the candidate events were selected. The restrictions for the candidate events are listed in sec. 4.2, 4.2.1, 4.2.3, 4.2.2. They serve to find the window, through which pass the events with the highest quality of measured physical parameters of the particle, which leaves the trace in the spectrometer. The deep inelastic scattering can be accessed only in the special kinematic region. Kinematic restrictions are written in sec. 4.2.4. The events are distributed in different kinematic regions, *bins*. In sec. 4.4 the statistics of selected events and their distribution for determined bins are presented. Then, the events are used to construct the asymmetry quantity. In sec. 4.3 the process of asymmetry extraction is shown. In sec. 4.3, 6 the difference between two kinds of constructed asymmetries is explained. The extraction procedure can be done in alternative way with the use of luminosity monitors, which measure the intensity of proceeded reactions in the target. The comparison of both ways is reflected in 4.5. Possible contamination of events by the background is estimated in sec. 4.6. The data was recorded during several years. Some parts of the spectrometer were exchanged by improved ones. The differences in experimental setup can influence the signal. The consistency of the recorded data from different measurement periods is checked in 4.7. The additional check of the extracted values is done by independent analyzer in sec 4.8.

4.1 Data quality

According to the DAQ description (see 3.5) the analyzer has the possibility to discard unreliable data by choosing a special 32 bit burst mask. This mask is applied to each burst bit pattern in the data sample. The burst mask verifies certain bits of the bit pattern which can be '0' (didn't work properly) or '1' (normal status). If at least one of the checked bits was '0', then this burst is discarded. The burst masks used in analysis are shown in table 4.1.

production	96d0	97d1	98e1, 99d1, 00e1	04d2	05d2	06f1, 07d1
burst mask	0x525e13dc	0x521e13dc	0x527e13dc	0x527813dc	0x527e13dc	0x567e13dc

Table 4.1: Burst masks applied to the data samples.

This analysis deals with beam polarization and selection of different hadrons. The condition of the target polarization can be ignored. Also in the case of normalization using DIS events, it is not needed to check bits related to the luminosity monitor. Instead, the attention should be paid to the work of PID detectors and polarimeters:

- proper working state of PID detectors (TRD, RICH, preshower, hodoscopes, calorimeter).
It discards bursts where defective segments were found in one of the PID detectors.
- absence of high voltage trips in the wire chambers.
Ensures good track reconstruction
- reasonable beam current ($2 \text{ mA} < I_b < 50 \text{ mA}$), dead-time correction ($0.5 < \delta_{dead} < 1.0$), burst length ($0 \text{ s} < L < 11 \text{ s}$).
It discards data with small counting rates consequently high statistical uncertainty and also controls safe conditions of data recording
- sufficient beam polarization value $0.2 < \text{beam polarization} < 0.8$
Used burst mask does not contain this criteria. It is additionally applied to each burst. This criteria discards low beam-polarization data which can not clearly reveal beam-spin effects. Data with unphysical high polarization is rejected by the upper limit of the criterion.
- polarization measurements are recorded less than 5 minutes ago.
Ensures proper polarization value of the beam.

4.2 Event selection

A DIS event candidate has as trigger requirement that a bunch of electrons passed HERA clock, and that all three hodoscopes and calorimeter gave a signal above threshold in the same spectrometer half, so called *trigger21*. SIDIS events form sample from DIS events. After passing data quality requirements each detected track should pass particle identification, reconstruction, geometric, and kinematic criteria or so called *cuts*. The selected lepton track e' or the selected lepton and hadron tracks $e'h$ form candidate events of interest:

- DIS candidate: $eN \rightarrow e'X$.
- SIDIS candidate: $eN \rightarrow e'hX$.

The lepton track with maximum momentum is considered as the DIS lepton if more than one lepton track is detected. For SIDIS candidate events more than one hadron can be detected. In this case it is assumed that each hadron track forms an individual SIDIS event:

$$[eN \rightarrow e'h_1h_2X] \Rightarrow [eN \rightarrow e'h_1X] + [eN \rightarrow e'h_2X].$$

DIS and SIDIS events are selected from corresponding candidate events with requirements which are applied on kinematic variables (kinematic cuts) used in SIDIS analyzes (see for variable definitions sec. 2).

4.2.1 Particle identification cuts

Lepton-hadron separation:

As was explained in sec. 3.4 lepton-hadron separation is based on a combined signal of PID detectors and initial particle flux, Φ . It is expressed in PID_n quantities (see fig. 3.14):

- leptons: $PID_3 + PID_5 - \log_{10} \frac{\Phi^l}{\Phi^h} > 2$.
- hadrons: $PID_3 + PID_5 - \log_{10} \frac{\Phi^l}{\Phi^h} < 0$.

The region of $0 < PID_3 + PID_5 - \log_{10} \frac{\Phi^l}{\Phi^h} < 2$ is excluded as an intermediate region between hadrons and leptons which increases contamination of leptons with hadrons or of hadrons with leptons (for details see [39]).

Charged hadron separation:

A RICH detector (with usage of applied p-matrices) separates hadron types based on the opening angle of the Cherenkov radiation, which is registered by the PMT matrix (see sec. 3.3.5), for a given particle momentum. It is able to separate pions and kaons in the hadron momentum range $2 \text{ GeV} < P_h < 15 \text{ GeV}$ and protons or antiprotons in the region $4 \text{ GeV} < P_h < 15 \text{ GeV}$. The EVT algorithm is used to take into account the topology of each event. The hadron selection also implies the ratio of the most (h_1) and the second most (h_2) likely hadron type: $Qp = \log_{10} \left(\frac{P_{h_1}^{event}}{P_{h_2}^{event}} \right)$. Following criteria for the hadron selection were applied:

- $Qp > 0$.
- $2 \text{ GeV} < P_{\pi^\pm} < 15 \text{ GeV}$.
- $2 \text{ GeV} < P_{K^\pm} < 15 \text{ GeV}$.
- $4 \text{ GeV} < P_{p(\bar{p})} < 15 \text{ GeV}$.

4.2.2 Reconstruction cuts

As was mentioned in sec. 3.5, the improved version of reconstruction HRC, the HTC reconstruction algorithm is used for parameter track reconstruction. It tries to bind selected single lepton or a pairs of lepton and hadron tracks with the beam-line to one vertex in presented

analysis, using probability criteria of Kalman filter procedure (for details see [80]) for tracks and found vertex. Following requirements for the event reconstruction were applied:

- vertex probability > 0.001 .
- track probability > 0.01 .

4.2.3 Geometric cuts

Geometric cuts discard regions of the spectrometer where tracks can not be safely reconstructed due to edge effects. These predominantly can appear near the spectrometer assemble: clamps, which defend spectrometer magnet (see fig. 4.1 a)), and on the edges of calorimeter. Cuts are separated into two sets, corresponding to "front" track and "back" track reconstruction (in front and behind the spectrometer magnet).

Front track:

- Vertex of track inside target cell:
 $-18 \text{ cm} < z_{\text{Vertex}} < 18 \text{ cm}$ (for 96-05 years),
 $5 \text{ cm} < z_{\text{Vertex}} < 20 \text{ cm}$ (for 06,07 years),
 assures that the track originates from target cell (see sec. 3.2).
- front field clamp position $|x_{\text{ffc}}| \leq 31 \text{ cm}$.
- rear field clamp position $|y_{\text{rfc}}| < 54 \text{ cm}$,
 avoids front and rear clamp's influence.
- septum plate position $|y_{\text{sp}}| > 7 \text{ cm}$,
 avoids region near to septum plate which encloses the pipe beam.

Back track:

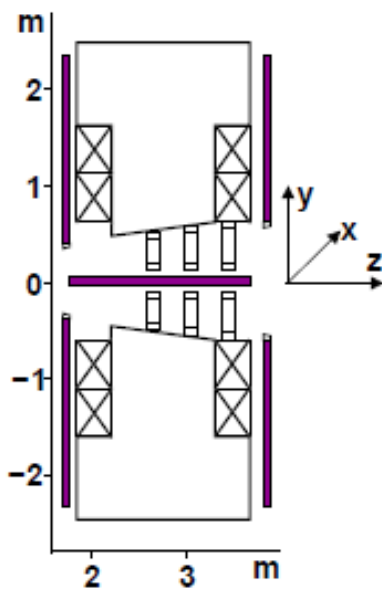
- rear clamp position $|x_{\text{rc}}| \leq 100 \text{ cm}$, $|y_{\text{rc}}| \leq 54 \text{ cm}$.
- calorimeter position: $|x_{\text{calo}}| \leq 175 \text{ cm}$ and $30 \text{ cm} \leq |y_{\text{calo}}| \leq 108 \text{ cm}$,
 avoid edges of calorimeter.

4.2.4 Kinematic cuts

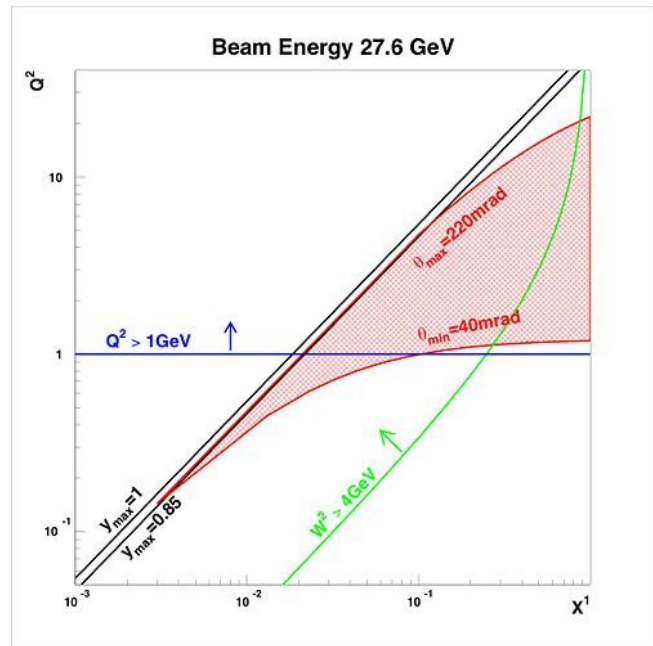
Each SIDIS event satisfies DIS kinematic cuts and has additional restrictions. Cuts are listed in table 4.2.

DIS	SIDIS	explanation
$Q^2 > 1 \text{ GeV}^2$	$Q^2 > 1 \text{ GeV}^2$...required for scattering processes in the deep-inelastic region
$W^2 > 4 \text{ GeV}^2$	$W^2 > 10 \text{ GeV}^2$...excludes events from resonance region
$0.1 < y < 0.85$	$0.1 < y < 0.85$...upper limit discards region with a large contribution by higher order QED effects. Lower limit is restricted by W^2 and Q^2 cuts
	$0.023 < x < 0.4$	Is restricted by the HERMES acceptance (see fig. 4.1). DIS events are used only for beam-balancing. Therefore, the cut is not necessary for DIS event

Table 4.2: Kinematic cuts for DIS and SIDIS events



a



b

Figure 4.1: a) Restrictions of the HERMES geometry acceptance caused by vertical front/rear clamps (shown violet) around spectrometer magnet and horizontal iron plate (shown in violet) around the beam pipe. b) Kinematic acceptance range of DIS events at HERMES (red area)

4.3 Extraction of $A_{LU}^{\sin \phi_h}$ asymmetries

In this analysis the asymmetry amplitudes were extracted using two methods:

Maximum likelihood method, ML:

The yields N^+ and N^- can be written as:

$$N^\pm(x, y, z, P_{h\perp}, \phi_h) = \epsilon(x, y, z, P_{h\perp}, \phi_h) \sigma^\pm(x, y, z, P_{h\perp}, \phi_h) L^\pm, \text{ where} \quad (4.1)$$

σ^\pm ...cross section for determined beam-spin state (positive or negative),

ϵ ...the acceptance function, which reflects the influence of the acceptance on the measured variables. It is (safely) assumed to not depend on the sign of polarization of the beam \pm .

From yields one can construct following extended probability density function (pdf):

$$pdf = dN = \epsilon \bar{\sigma}_{UU} [1 + A_{UU}^{\cos(\phi_h)} \cos \phi_h + A_{UU}^{\cos(2\phi_h)} \cos 2\phi_h + P_i A_{LU}^{\sin(\phi_h)} \sin(\phi_h)], \text{ where} \quad (4.2)$$

$\bar{\sigma}_{UU}$... the ϕ_h -independent unpolarized cross-section,

P_i ...the beam polarization value defined for each event

$A_{UU}^{\cos(\phi_h)}, A_{UU}^{\cos(2\phi_h)}, A_{LU}^{\sin(\phi_h)} \sin(\phi_h)$... azimuthal modulations

The eq. 4.2 can be simplified, while the $A_{UU}^{\cos(2\phi_h)}$ and $A_{UU}^{\cos(\phi_h)}$ are assumed to give a small impact to the measurements of $A_{LU}^{\sin(\phi_h)}$ (see for details in [43], [96]), and therefore, they can be neglected. The influence of spin-independent terms $A_{UU}^{\cos(2\phi_h)}$ and $A_{UU}^{\cos(\phi_h)}$ to the extraction of $A_{LU}^{\sin(\phi_h)}$ is presented in sec. 5.2.

The following extended probability density function can be written:

$$pdf = dN = \epsilon \bar{\sigma}_{UU} [1 + P_i A_{LU}^{\sin(\phi_h)} \sin(\phi_h)] \quad (4.3)$$

Since the measurements are all assumed to be independent, the probability to have the sequence of these measurements is contained in likelihood function (LF):

$$L(\theta, \phi_h, P_i) = \prod_i^N \frac{pdf(\theta, \phi_h, P_i)}{\mathbb{N}(\theta, \phi_h)}, \text{ where} \quad (4.4)$$

θ is set of parameters to be fit,

$\mathbb{N}(\theta, \phi_h)$ is the normalization of the pdf.

The normalization can be rewritten in following form:

$$\mathbb{N}(\theta) = \int d\phi_h d(\theta) d(P_i) pdf(\theta, \phi_h, P_i) \quad (4.5)$$

The acceptance efficiency ϵ and cross section $\bar{\sigma}_{UU}$ can be omitted in the numerator of eq. 4.4 since they do not depend on the fitting parameters θ . However they have to be taken into account in the normalization integral.

The LF should be maximized for the determination of the pdf parameters. Usually it is technically easier to minimize $-\ln[L(\theta, \phi_h, P_i)]$ [92].

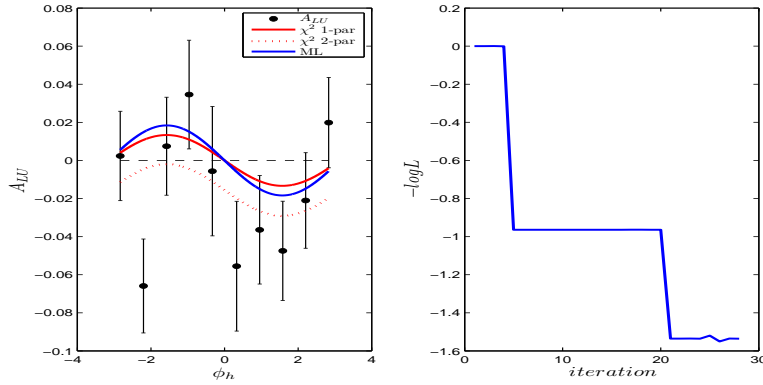


Figure 4.2: Left side: χ^2 1-parameter, χ^2 2-parameter and ML methods with corresponding $\sin(\phi_h)$ -amplitudes: 0.01040 ± 0.00880 , 0.01039 ± 0.00880 , 0.01143 ± 0.00822 . Right side: search of optimal parameter by minimizing logarithm of likelihood function

According to [91] the normalization integral can be ignored if the integrated polarization yields of both states are balanced:

$$P^+ L^+ = P^- L^- . \quad (4.6)$$

From this equation the *beam-balance weight* $\omega^- = \frac{P^+ L^+}{P^- L^-}$ is calculated, which scales down the higher polarization yield in eq. 4.4, so that for the smaller yield $\omega^+ = 1$. If positive polarization would be higher, than one has $\omega^+ = \frac{P^- L^-}{P^+ L^+}$ and $\omega^- = 1$. Implementation of weights in ML fit is explained in more details here [93]. Balancing of integrated yields in the χ^2 method is automatically implemented in eq. 4.9 via the ratio $\frac{N^\pm P^\mp}{L^\pm}$. The method described above gives following equation for the logarithm of the LF:

$$-\ln L = -\sum_{i=1}^{N^+} \omega^+ \ln[1 + P_i A_{LU}^{\sin \phi_h} \sin \phi_h] - \sum_{i=1}^{N^-} \omega^- \ln[1 + P_i A_{LU}^{\sin \phi_h} \sin \phi_h] \quad (4.7)$$

Minimizing eq. 4.7, the fit parameter $A_{LU}^{\sin \phi_h}$ is extracted. It is also usefull to take into account the dependence on the ratio of longitudinal and transverse photon flux, ε (see eq. 2.33 and 2.34) and extract $A_{LU}^{\sin \phi_h}$ without the dependence on this factor by adding this factor in

eq. 4.7:

$$-\ln L = -\sum_{i=1}^{N^+} \omega^+ \ln[1 + P_i \sqrt{2\varepsilon(1-\varepsilon)} A_{LU}^{\sin\phi_h} \sin\phi_h] - \sum_{i=1}^{N^-} \omega^- \ln[1 + P_i \sqrt{2\varepsilon(1-\varepsilon)} A_{LU}^{\sin\phi_h} \sin\phi_h] \quad (4.8)$$

To separate these two different kinds of $A_{LU}^{\sin\phi_h}$ asymmetries, the first one will be depicted on graphics with title $2\langle\sin\phi_h\rangle_{LU}$ (so called Lepton Beam Asymmetry, LBA) and the second one will be shown with title $\frac{2\langle\sin\phi_h\rangle_{LU}}{\sqrt{2\varepsilon(1-\varepsilon)}}$ (so called Virtual Photon Asymmetry, VPA). The ε factor takes into account the y-dependence of the asymmetry and allows to compare results from two experiments with different kinematic restrictions. The asymmetries have similar behavior and are compared in fig. 6.1 in sec. 6. To avoid a large number of figures for both VPA and LBA asymmetries, the VPA was chosen to be shown in all intermediate steps, while the final plots will be shown for both kinds of asymmetries. Methods χ^2 and ML give similar values of the extracted parameters. The ML method is less affected by the limited statistics and does not assume a Gaussian distribution of variable inside the bin. Therefore, it gives smaller statistical errors in case of restricted statistics.

χ^2 – method:

The asymmetries for each ϕ_h bin were calculated with the formula:

$$A_{LU}(\phi_h) = \frac{\frac{N^+(\phi_h)}{L^+} - \frac{N^-(\phi_h)}{L^-}}{\frac{N^+(\phi_h)P^-}{L^+} + \frac{N^-(\phi_h)P^+}{L^-}}, \quad (4.9)$$

where N^+ and N^- are the yields of SIDIS events in a certain ϕ_h -bin collected with positive or negative polarization states of the beam,

P^+ and P^- are mean beam polarizations of positive and negative polarization states respectively,

L^+ and L^- are number of DIS events or luminosities used for normalization of cross-sections and collected with positive or negative polarization states of the beam.

The asymmetry was fitted with a one-parameter function or a two-parameter function:

$$\text{fit}(A_{LU}(\phi_h))_{\chi^2} = A_{LU}^{\sin\phi_h} \sin\phi_h \quad (4.10)$$

$$\text{fit}(A_{LU}(\phi_h))_{\chi^2} = C + A_{LU}^{\sin\phi_h} \sin\phi_h, \text{ where} \quad (4.11)$$

C is a constant term, which is a non-physical parameter that should be zero in the ideal case.

The influence of the size of the data sample can be visualized in fig. 4.3. Here four MC samples with variable number of events were selected: 100, 1000, 10000, 50000 events. In each sample a constant asymmetry value equal to 0.02 (indicated by the vertical black line) was

implemented. The implementation was done 1000 times to estimate the influence of random numbers used in procedure. After each implementation MC sample was fitted with ML and χ^2 (10 ϕ -bins). It is easy to see, that ML method gives smaller fit uncertainties which decrease with statistical power of the sample.

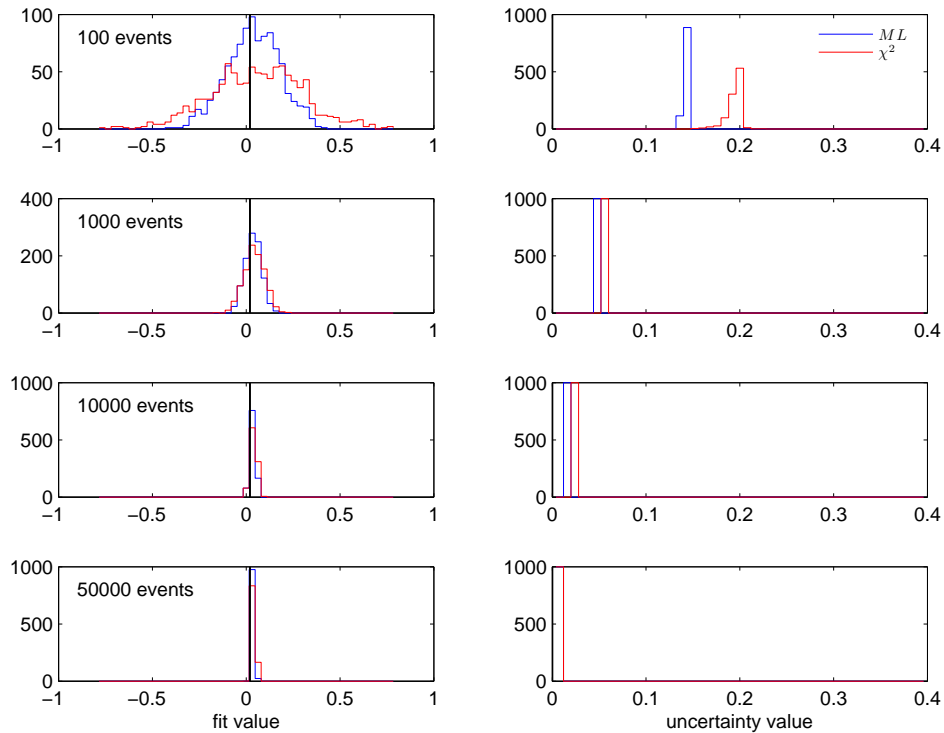


Figure 4.3: Asymmetries extracted with different fit methods from samples with variable generated number of events

The number of ϕ -bins for χ^2 method also can be varied. In fig. 4.4 one can see the results of two χ^2 fits with number of ϕ -bins equal to 4 and 14. The fit with 14 bins gives smaller uncertainties. The value of fit with 14 bins is also a bit closer to the value of implemented asymmetry.

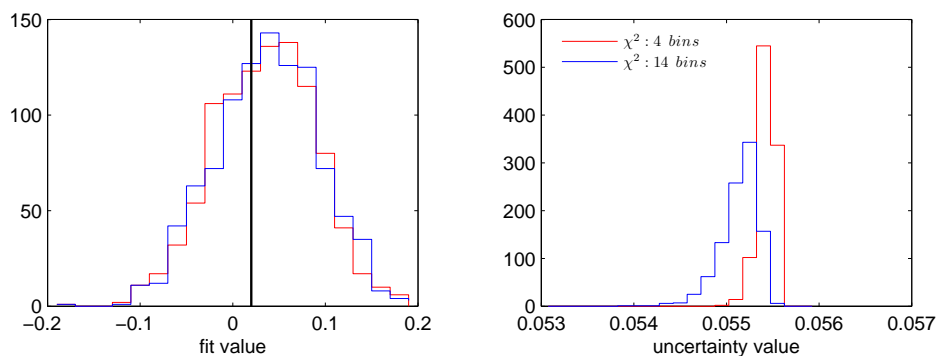


Figure 4.4: Asymmetries extracted with different fit methods from samples with variable generated number of events

These pictures demonstrate the need of adjustment of χ^2 method to the certain task. Therefore, the ML method was chosen. However, the χ^2 method can be used to extract the constant term. The constant term value is expected to be zero and can be used as an additional check for the physical validity of the extracted parameters. As can be seen from fig. 4.2, the constant term does not influence the amplitude of the $\sin \phi_h$ modulation.

4.4 Yields and kinematic bins

The numbers of DIS events and SIDIS events passing through the selection cuts can be found in table 4.3. The DIS events are written for both polarization states with $Pol > 0$ and $Pol < 0$ for data collected on hydrogen and deuterium targets.

yields	hydrogen	deuterium
DIS	53423845	20614905
DIS, $Pol > 0$	33201421	11083116
DIS, $Pol < 0$	20222424	9531789
π^+	4394716	2403572
π^-	3146129	1952891
K^+	746875	394355
K^-	304970	180296
p	458045	249478
\tilde{p}	69414	40784

Table 4.3: Collected DIS and SIDIS events for hydrogen and deuterium targets.

Kinematic distributions of DIS leptons are shown in fig. 4.5.

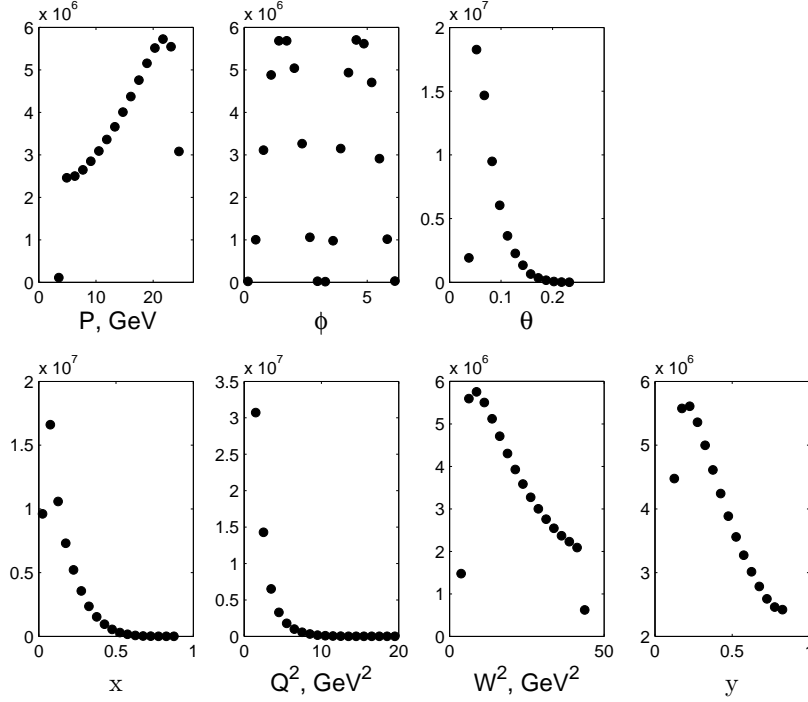


Figure 4.5: Kinematic distributions of selected DIS leptons

Obtained SIDIS events for each type of selected hadron are distributed in kinematic bins written in table 4.4. The kinematic range is separated in $4x$, $4z$ and $4P_{h\perp}$ bins. The results are presented in 3D for $4x \cdot 4z \cdot 4P_{h\perp} = 64$ bins. The boundaries of bins were set to fulfill the condition, that each bin has relatively same number of particles. This feature allows fit convergence (in other words extraction of asymmetry) for each bin.

x	0.023-0.071	0.071-0.104	0.104-0.149	0.149-0.4
z	0.2-0.3	0.3-0.37	0.37-0.47	0.47-0.7
$P_{h\perp}$, GeV	0.05-0.23	0.23-0.35	0.35-0.51	0.51-1.8

Table 4.4: Kinematic bins used in the present analysis.

It is convenient to show the distributions of selected hadrons in 2D view using three possible projections: $P_{h\perp} - x$, $z - x$, $P_{h\perp} - z$. Each projection is shown in fig. 4.6 according to particle type. Bin boundaries from table 4.4 are shown as solid black lines in the pads. For the $P_{h\perp} - z$ projection it can be seen, that z -distribution is highly influenced by the type of the mass : $z \sim M_h$.

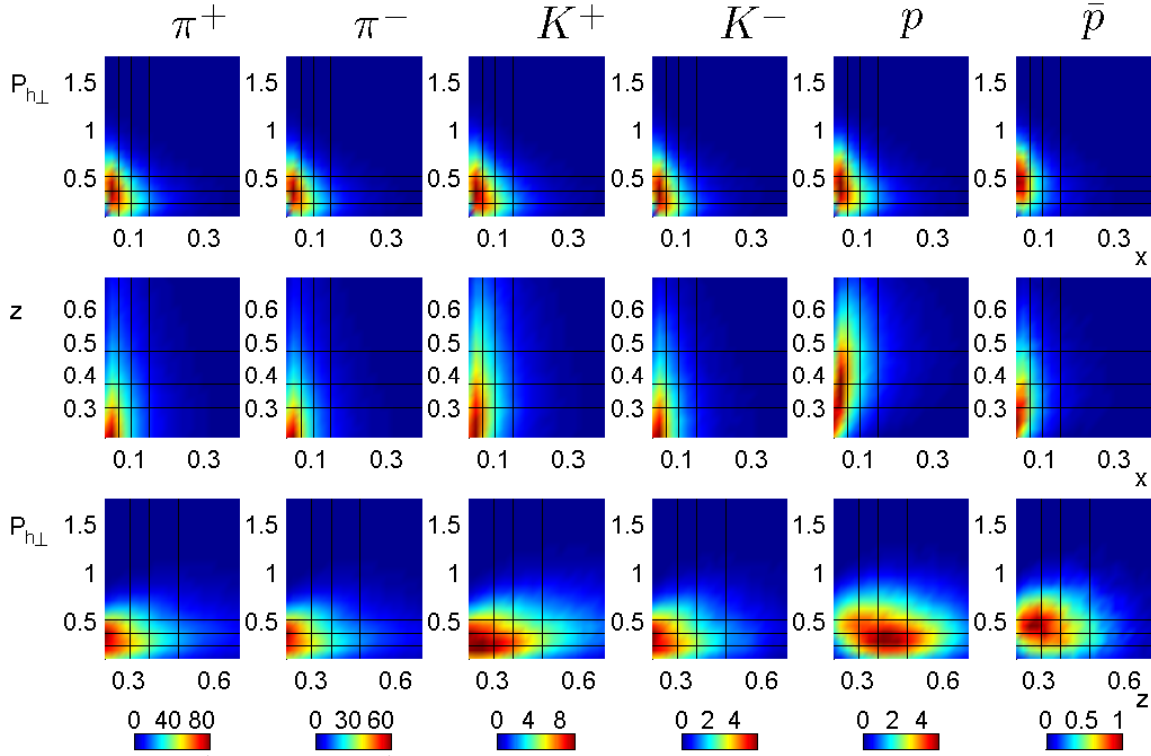


Figure 4.6: Kinematic distributions of selected SIDIS events. The legend for the density of events is given in multiplicative 10^3 in the colormap below the distributions.

In the high- z region ($z > 0.7$) the contributions of exclusive processes become sizeable:

- $e + p \rightarrow e' + p' + \rho^0$, $\rho^0 \rightarrow \pi^+\pi^-$
- $e + p \rightarrow e' + p' + \phi$, $\phi \rightarrow K^+K^-$
- $e + p \rightarrow e' + p' + \omega$, $\omega \rightarrow \pi^+\pi^-\pi^0$

High- z range asymmetries are extracted only in z because of lack of statistics, which prevents to show the results in all three dimensions. Also high z -range is not shown for SIDIS events with produced \bar{p} , again, because of lack of statistics for this particle.

In addition to 3D results, the 1D binning was also used. The 3D results serve theorist calculations, while 1D plots are easier to view and interpret for readers. For the 1D results was possible to increase the number of bins in each projection. The 1D binning is shown in tables 4.5- 4.7:

x-range	0.023-0.04	0.04-0.06	0.06-0.08	0.8-0.11	0.11-0.4
z-range	0.2-0.7				
$P_{h\perp}$ -range, GeV	0.05-1.8				

Table 4.5: Kinematic x-bins.

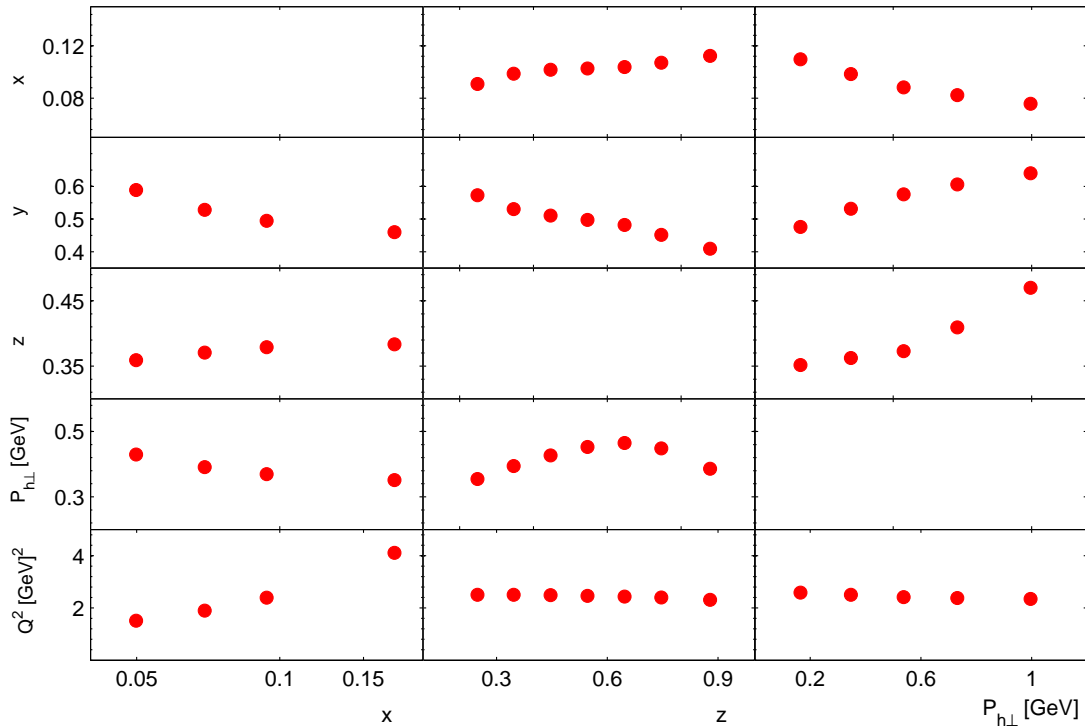
z-range, π^\pm, K^\pm, p	0.2-0.3	0.3-0.4	0.4-0.5	0.5-0.6	0.6-0.7	0.7-0.8	0.8-1.0
z-range, \tilde{p}	0.2-0.3	0.3-0.4	0.4-0.5	0.5-0.6	0.6-0.7		
x-range	0.023-0.4						
$P_{h\perp}$ -range, GeV	0.05-1.8						

Table 4.6: Kinematic z-bins .

$P_{h\perp}$ -range, GeV	0.05-0.25	0.25-0.45	0.45-0.65	0.65-0.85	0.85-1.8
z-range	0.2-0.7				
x-range	0.023-0.4				

Table 4.7: Kinematic $P_{h\perp}$ -bins.

For 1D binning the mean values of the kinematic variables are shown in each kinematic bin in fig. 4.7. For example, it can be seen, that Q^2 and z or Q^2 and $P_{h\perp}$ don't have the correlation. In contrast to theory (when an ideal spectrometer has full coverage of detected particles in the angle of 4π) the correlation between variables Q^2 and x appears because of the influence of acceptance of spectrometer.

**Figure 4.7:** Mean kinematic values of SIDIS events for produced hadrons of type π^+ in each bin.

4.5 Choice of normalization (DIS events/Luminosity)

Fit methods χ^2 and ML were explained in sec. 4.3 based on DIS-event balancing of yields with opposite polarization. Alternatively, the balancing procedure can be done through integrated luminosity measured by the luminosity monitor (see sec. 3.3.6).

The total integrated luminosity is calculated as:

$$L_{LUMI} = C_{LUMI} \cdot f \sum_{i=1}^{bursts} R_{LUMI} \cdot t_{DAQ} \cdot t_{burst}, \text{ where} \quad (4.12)$$

R_{LUMI} ... the coincidence rate of the luminosity monitor is read out once per burst i

t_{DAQ} ... fractional life-time of DAQ system (dead time correction)

t_{burst} ... time length of the burst

C_{LUMI} ... proportionality constant that relates the rate of the monitor to the luminosity per nucleon

f ... factor that reflects the ratio of electrons to nucleons for the target gas (f=1 for hydrogen, f=2 for deuterium)

The luminosity obtained from the monitor measurements has large systematic uncertainty due to the dependence of the luminosity monitor acceptance on the beam position. As it was mentioned in sec. 3.3.6 the uncertainty cancels out due to the ratios used in the balancing procedure for both methods. In fig. 4.8 it is shown that the difference between asymmetries extracted with DIS and Luminosity balancing is negligible. In present analysis the balancing procedure is based on the measurement of DIS.

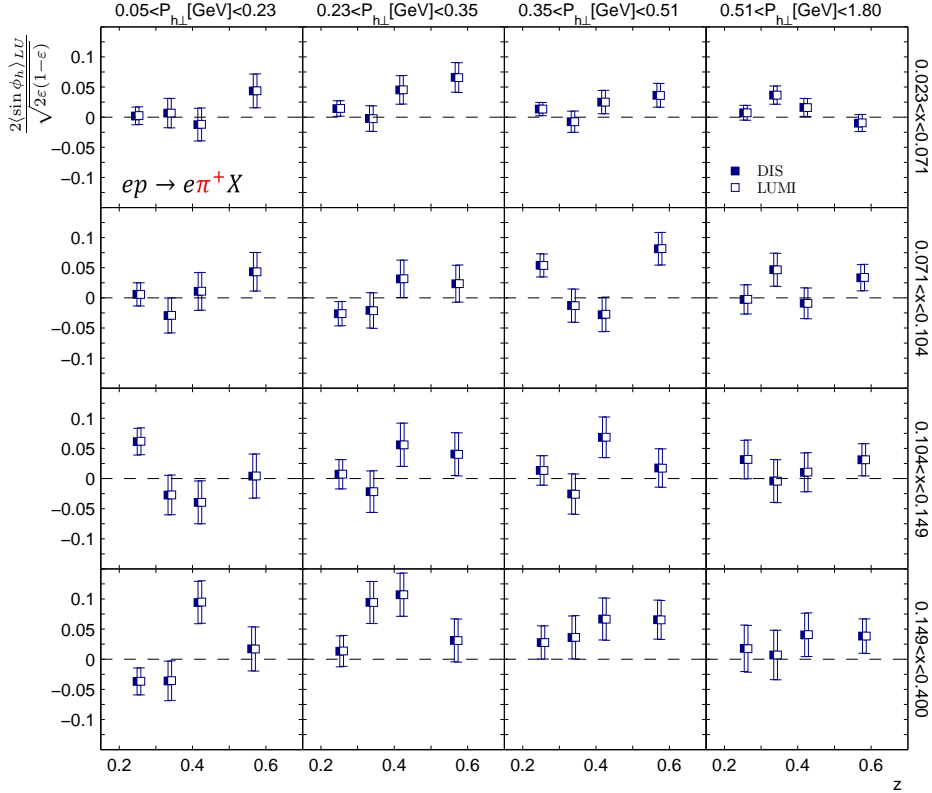


Figure 4.8: π^+ asymmetries obtained from data collected on the hydrogen target with using L_{DIS} (full symbols), L_{LUMI} (open symbols).

4.6 Charge symmetric background

Non-DIS processes such as the decay of real photons $\gamma \rightarrow e^+e^-$ and neutral pions $\pi^0 \rightarrow e^+e^-\gamma$ can lead to identification of DIS candidate leptons with one coming from produced pair, where the detected lepton is not scattered lepton, but instead originates from the former processes.

The leptons coming from these processes always appear in pairs with opposite charge and form the so called Charge Symmetric Background (CSB). In some events one of the produced leptons is not detected because of the detector acceptance constraints. Therefore, the requirement on the existence of oppositely charged leptons can not discard all CSB events. The following procedure is applied in order to account the CSB. To each SIDIS a weight $w_{CSB} = 1$ is assigned when the DIS lepton has the same charge as the beam lepton, and a weight $w_{CSB} = -1$ when the DIS lepton has the opposite charge.

After that all events with $w_{CSB} = 1$ form the number of events $N_{same} = \sum w_{CSB}$, while events with $w_{CSB} = -1$ form the number of events $N_{opposite} = |\sum w_{CSB}|$. Using these numbers the CSB fraction of events can be calculated for each kinematic bin:

$$CSB = \frac{N_{opposite}}{N_{same}} \quad (4.13)$$

The CSB fraction is shown in fig. 4.9. It is clearly seen, that the CSB fraction increases with

increasing $P_{h\perp}$ and decreases with increasing z . The maximum of CSB fraction is estimated to be less than 4%.

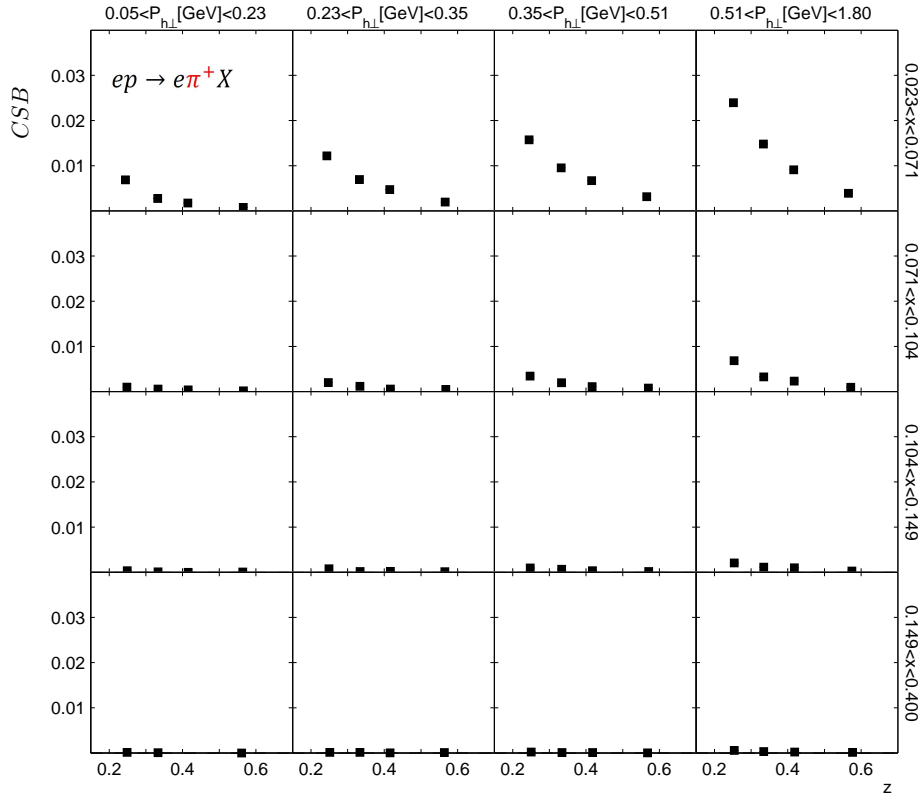


Figure 4.9: The CSB ratio for π^+ asymmetries. One point in the left bottom panel is absent due to $N_{opposite} = 0$ in eq. 4.13.

In order to account for CSB, the weight w_{CSB} is assigned to each event in the LF function (see eq. 4.7):

$$-\ln L = -\sum_{i=1}^{N^+} \omega^+ w_{CSB} \ln[1 + P_i A_{LU}^{\sin\phi_h} \sin\phi_h] - \sum_{i=1}^{N^-} \omega^- w_{CSB} \ln[1 + P_i A_{LU}^{\sin\phi_h} \sin\phi_h] \quad (4.14)$$

The comparison of asymmetries extracted with and without CSB correction is shown in fig. 4.10. The difference between the two sets of asymmetries is very small. In the following, the CSB correction is applied.

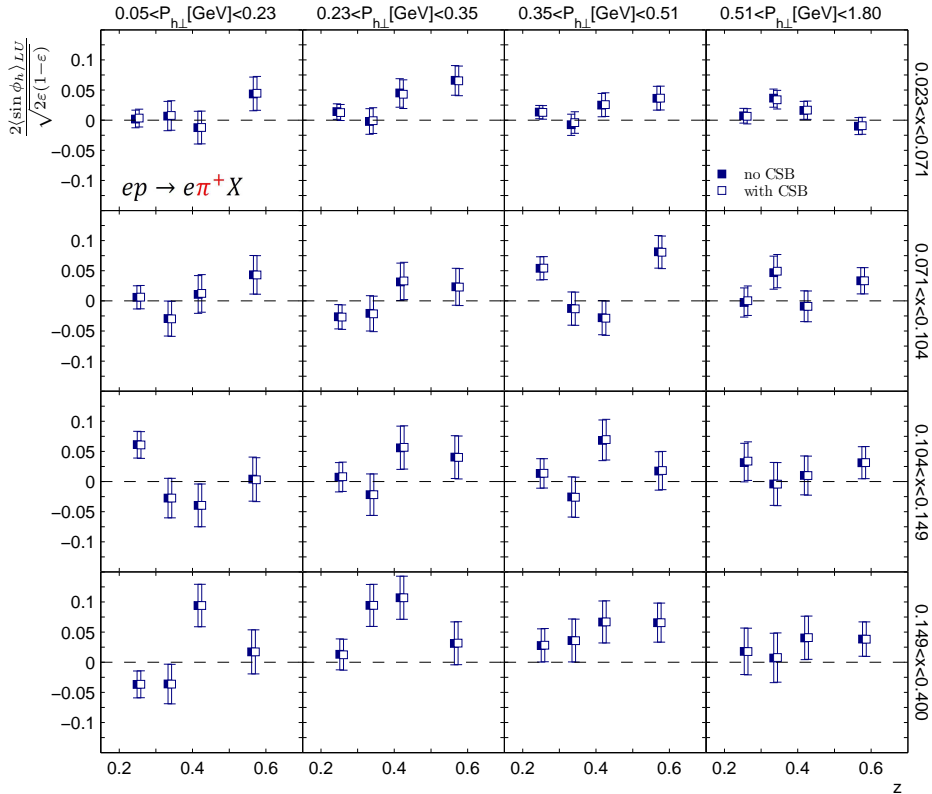


Figure 4.10: Influence of CSB correction on π^+ asymmetries for hydrogen sample. Uncorrected asymmetries are shown in full red symbols, while corrected ones are shown in open symbols

4.7 Data merging

In this analysis extracted asymmetries were constructed using data collected over nine years: 1996, 1997, 1998, 1999, 2000, 2004, 2005, 2006, 2007. During these periods the experimental setup was changed several times by exchanging detectors or their damaged part. In 1998 the Cherenkov threshold detector was replaced by the RICH detector. This change allowed not only to identify pions, but also kaons and (anti)protons, and also increased the momentum range of the detected pions from $4.5 \text{ GeV} < p < 13.5 \text{ GeV}$ to $2 \text{ GeV} < p < 15 \text{ GeV}$. In 2006, a new target cell shorter than the old one used in 1996-2005, was installed. The new cell was shifted downstream with respect to the old cell. In 2006 also a recoil detector was installed around the target cell. Moreover, running conditions regarding the beam and target could differ for different periods. In 1996, 1997, 1999, 2004, part of 2006 and 2007 a positron beam was used, while in 1998, 2005 and part of 2006 an electron beam was used. In 2004 and 2005 data with transversely polarized hydrogen target was collected, while in part of 1996, part of 1997, part of 1998, part of 1999 hydrogen data, and in 1998, 1999, 2000 deuterium data with longitudinal polarization were taken, correspondingly. In part of 1996, part of 1997, part of 1998, part of 1999, 2000, 2006 and 2007 data was collected on the unpolarized target. The data samples collected on longitudinally polarized and transversely polarized targets were taken

without identification of target polarization and are treated as data samples collected on the effectively unpolarized target. During some of the periods, data samples with high density and normal density gas were collected. Because of the changes of the experimental setup, four periods for data collection on a hydrogen target can be selected:

- 96, 97 (9697)... where long target cell contained unpolarized and longitudinally polarized gases. Cherenkov detector was used for pions identification in kinematic range of hadron momentum $4.5 \text{ GeV} < P_{\pi^\pm} < 13.5 \text{ GeV}$
- 98, 99, 00, 04, 05 (9805)... where long target cell contained unpolarized and longitudinally polarized gases. RICH detector was used for pions, kaons and anti(protons) identification in kinematic range of hadron momentum $2 \text{ GeV} < P_h^\pm < 15 \text{ GeV}$
- 04, 05 (0405) ... where long target cell contained transversely polarized gas. In comparison to 9805 period an influence of the transverse target magnet is assumed. RICH detector was used for pions, kaons and anti(protons) identification in kinematic range of hadron momentum $2 \text{ GeV} < P_h^\pm < 15 \text{ GeV}$
- 06, 07 (0607) ... where short target cell contained unpolarized gas. RICH detector was used for pions, kaons and anti(protons) identification in kinematic range of hadron momentum $2 \text{ GeV} < P_h^\pm < 15 \text{ GeV}$

For the data collected on deuterium target two periods can be selected:

- 98, 99, 00, 04, 05 (9805)... where long target cell contained unpolarized and longitudinally polarized gases. RICH detector was used for pions,kaons and anti(protons) identification in kinematic range of hadron momentum $2 \text{ GeV} < P_h^\pm < 15 \text{ GeV}$
- 06, 07 (0607)... where short target cell contained unpolarized gas. RICH detector was used for pions,kaons and anti(protons) identification in kinematic range of hadron momentum $2 \text{ GeV} < P_h^\pm < 15 \text{ GeV}$

A different momentum range for the detection of pions using the Cherenkov detector in 1996-1997 ($4.5 \text{ GeV} < P_{\pi^\pm} < 13.5 \text{ GeV}$) and 1998-2007 ($2 \text{ GeV} < P_{\pi^\pm} < 15 \text{ GeV}$) using the RICH detector can lead to incompatibilities of pion distributions, as shown in fig. 4.12, while the DIS lepton distributions stay unchanged, as shown in fig. 4.11. The most drastic difference of pion distributions can be seen for low-z range.

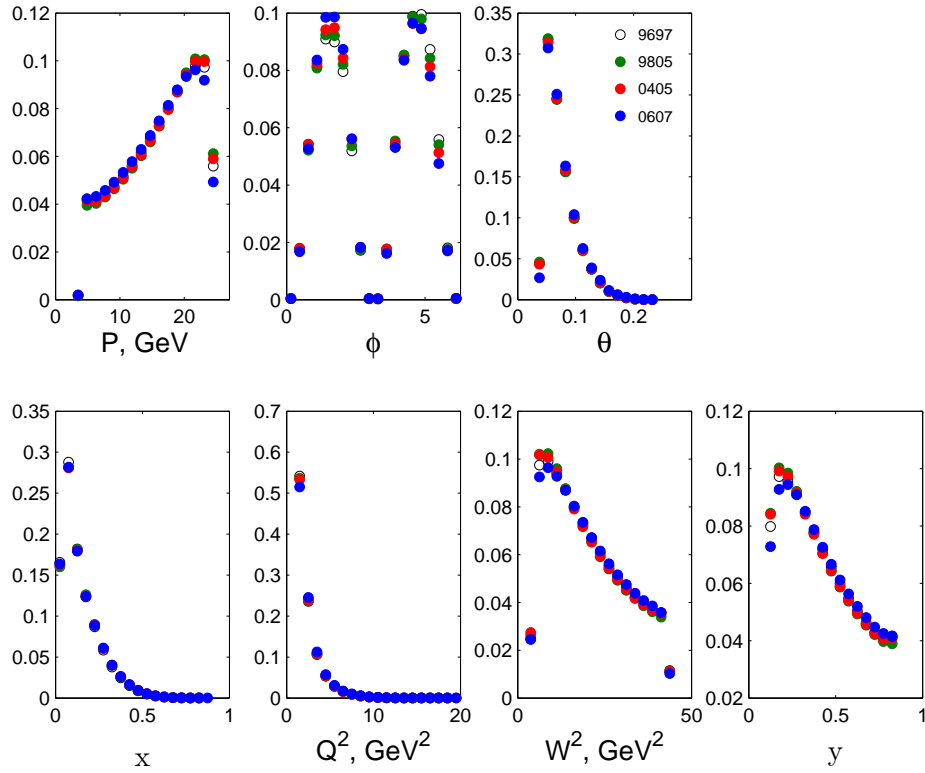


Figure 4.11: The DIS lepton distributions for the periods: 9697 (open black circles), 9805 (green circles), 0405 (red circles), 0607 (blue circles). Distributions are normalized to unity because of different statistics of each period

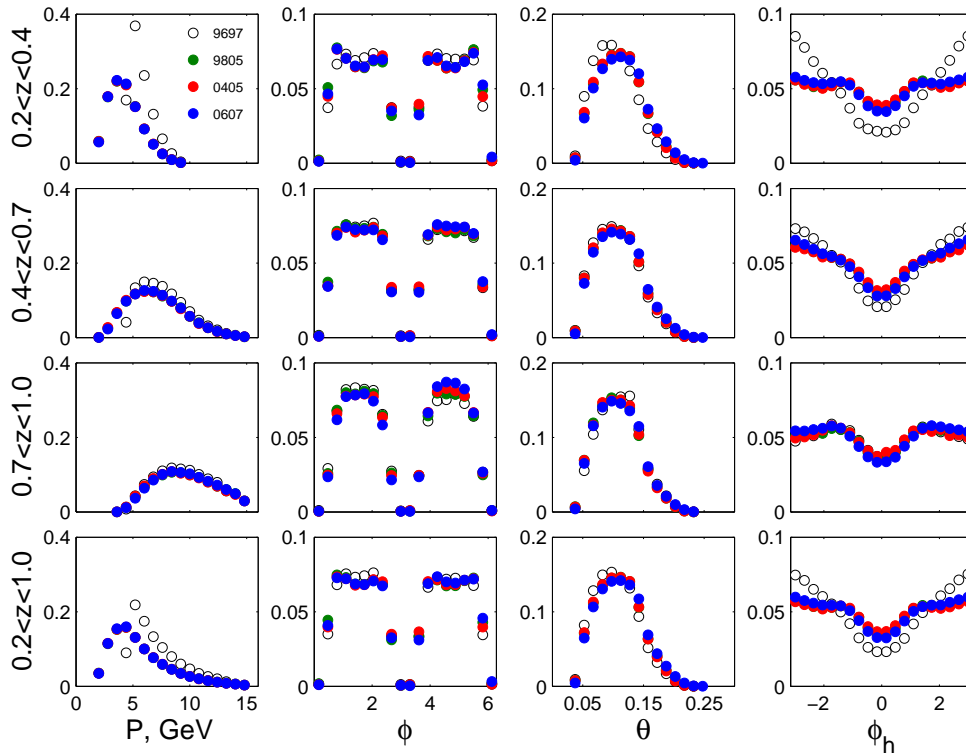


Figure 4.12: The SIDIS π^+ distributions for the periods: 9697 (open black circles), 9805 (green circles), 0405 (red circles), 0607 (blue circles). First row of plots reflects the low- z range, second row of plots shows the middle- z range, third row of plots depicts the high- z range and the last row presents the overall value over the whole z range

In order to check the influence of RICH and Cherenkov detectors on the momentum resolution, the data collected during 1998-2007 years was applied with the same momentum cut as for 1996-1997 data. In fig. 4.13 one can see that all data period distributions lie on the top of each other.

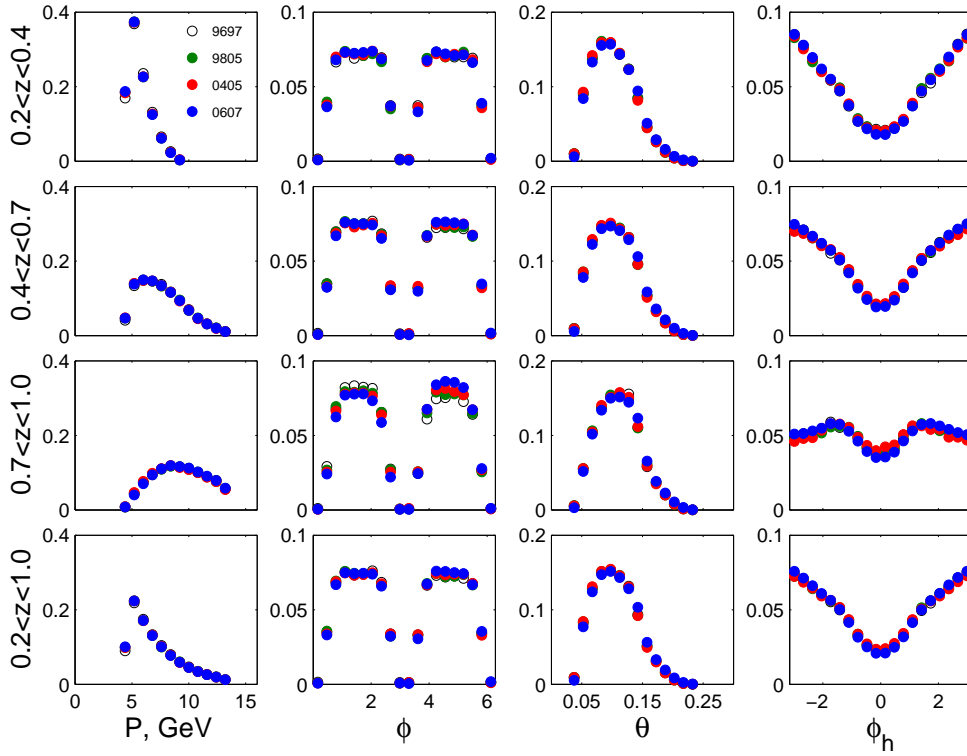


Figure 4.13: The SIDIS π^+ distributions for the periods: 9697 (open black circles), 9805 (green circles), 0405 (red circles), 0607 (blue circles). First row of plots reflects the low- z range, second row of plots shows the middle- z range, third row of plots depicts the high- z range and the last row presents the overall value over the whole z range. For the data collected in 1998-2007 a hadron momentum cut $4.5 \text{ GeV} < p_{\pi^\pm} < 13.5 \text{ GeV}$ was applied.

Apparatus changes could lead to misalignments and shifts between detector parts. All these differences should have been taken care of in the data production (e.g. the alignment procedure), but could result in systematic discrepancies between asymmetries extracted from different periods. In order to estimate the significance of the discrepancies between asymmetries based on data collected in different periods, the *deviation* technique is applied. For two sets of asymmetries $A1_{LU}^{\sin\phi}$ and $A2_{LU}^{\sin\phi}$ extracted from different data collecting periods their deviation is calculated as:

$$\text{dev} = \frac{A1_{LU}^{\sin\phi} - A2_{LU}^{\sin\phi}}{\sqrt{\sigma_1^2 + \sigma_2^2}}, \text{ where} \quad (4.15)$$

$\sigma_{1(2)}^2$ are the statistical uncertainties of the extracted asymmetries obtained from the fitting procedure.

Deviation technique shows how much the two data sets differ in units of *standard deviations*.

As an example, two sets of asymmetries are shown in fig. 4.14 for data collected on hydrogen target during 9805 and 0607 periods. In fig. 4.15 the deviation of corresponding asymmetries

is shown.

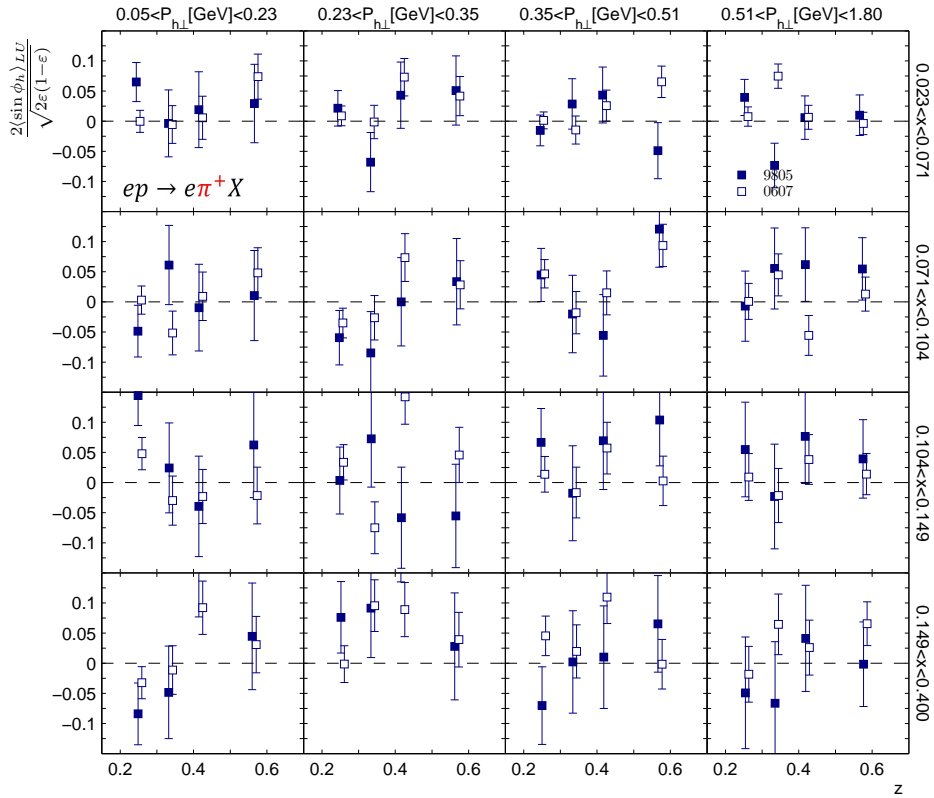


Figure 4.14: Asymmetries of 9805 and 0607 periods.

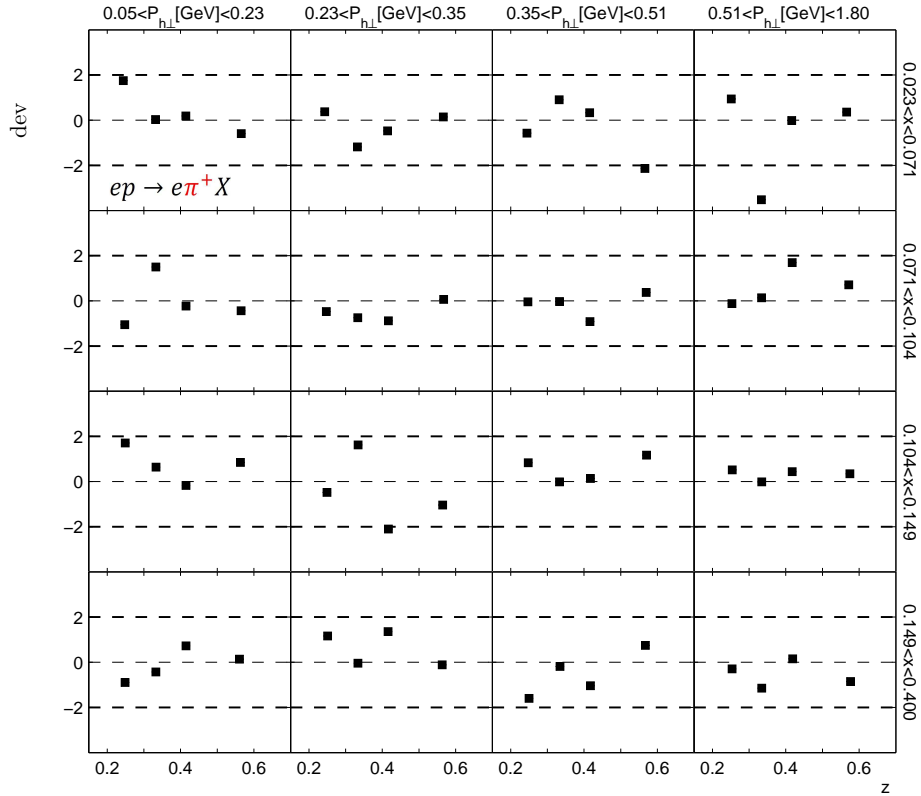


Figure 4.15: Asymmetry deviations of 9805 and 0607 periods.

For this comparison it can be seen that the majority of deviation points fluctuates around zero without systematic shifts and lies in 2σ -region. In a similar way, all other data periods were compared. The results can be found in fig. 4.16- 4.18. Based on this it can be concluded that there is no significant time-dependence that would have to be assigned as systematic uncertainty. The results from the fits from the various time periods (9805, 0405 and 0607) can thus be combined according to their individual uncertainties.

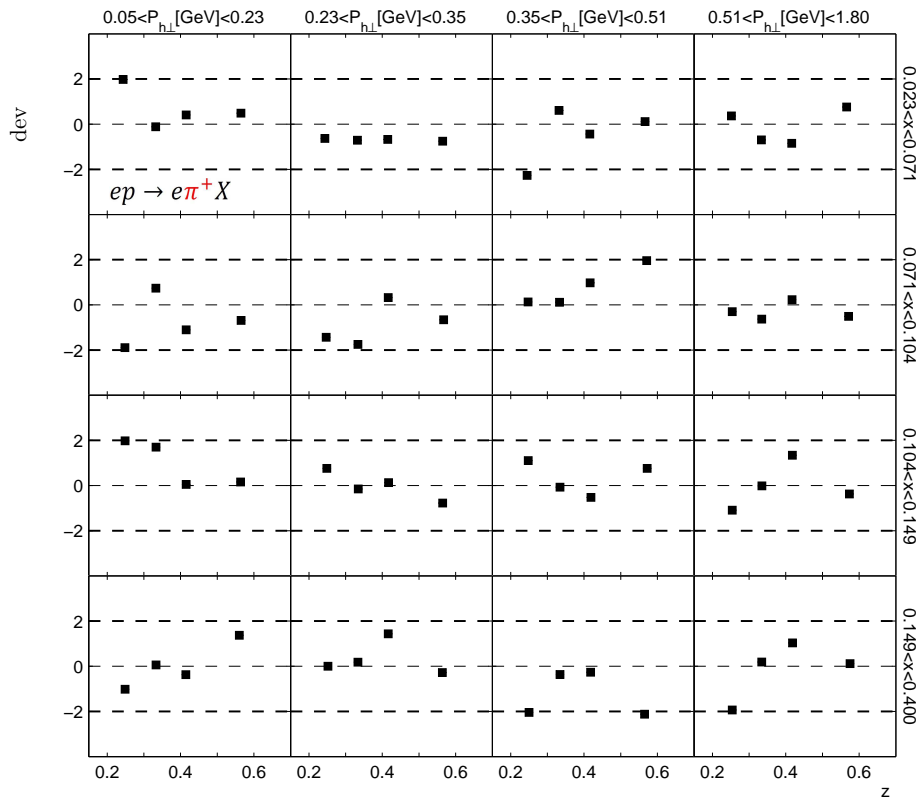


Figure 4.16: Asymmetry deviations of 9805 and 0405 periods.

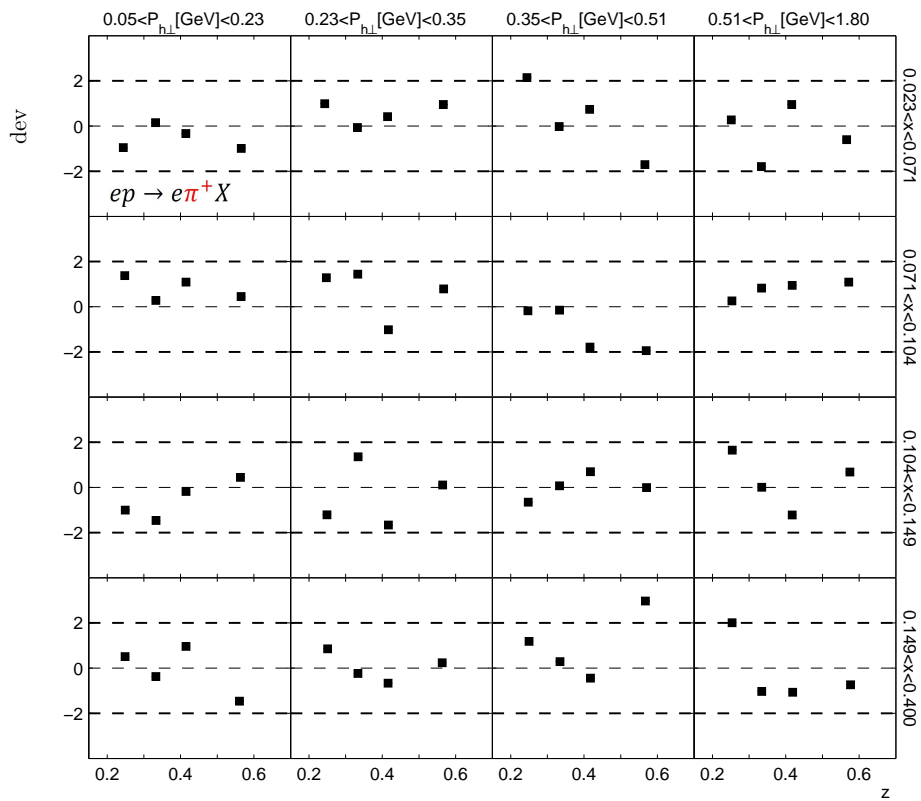


Figure 4.17: Asymmetry deviations of 0405 and 0607 periods.

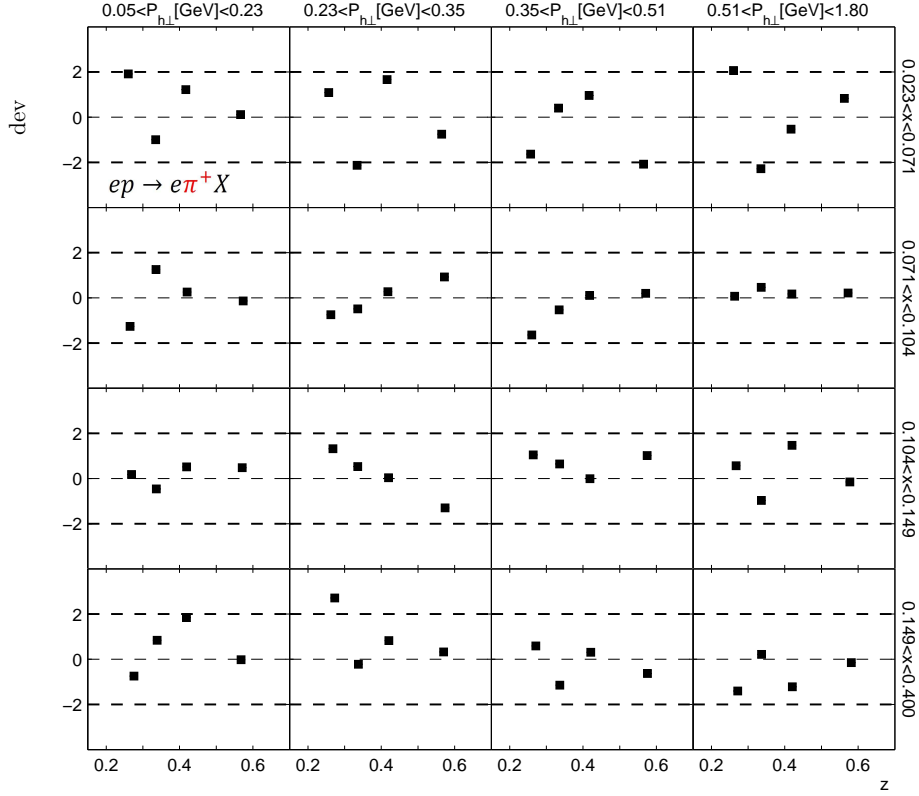


Figure 4.18: Asymmetry deviations of 9805 and 9697 periods.

In order to decide if the results of 1996-1997 are presented separately from the results of 1998-2007 or merged all together, one needs to not only compare the asymmetries through deviation technique, but also the total uncertainties corresponding to the two possible combinations of these data periods. Either the asymmetry and corresponding uncertainty is determined for the periods 1996-2007 as a whole, or the asymmetries for the period 1996-1997 and 1998-2007 are extracted separately and then averaged. The uncertainty corresponding to the former extraction is given by $\sigma_{total-I}^{9607}$ in eq. 4.16, while the uncertainty corresponding to the latter is given by $\sigma_{total-I}^{9607}$:

$$\frac{1}{(\sigma_{total-I}^{9607})^2} = \frac{1}{(\sigma_{comb}^{9697})^2} + \frac{1}{(\sigma_{comb}^{9807})^2}$$

$$(\sigma_{total-II}^{9607})^2 = (\sigma_{comb}^{9607})^2, \text{ where} \quad (4.16)$$

$$\sigma_{comb}^{period} = \sqrt{(\sigma_{stat}^{period})^2 + (\sigma_{sys}^{period})^2}$$

If $\sigma_{total-I}^{9607} \gg \sigma_{total-II}^{9607}$, then it is reasonable to merge the samples. In the opposite case the results of two data periods should be presented separately. The calculation of the systematic uncertainty is described in sec. 5.4. The results of the test can be found in fig. 4.19 and fig. 4.20. It can be seen that the total uncertainties fluctuate from bin to bin, and that there is no strong argument to present two separate sets of results. Therefore, the data collected during 1996-1997 was merged with the 1998-2007 data. In this way the phenomenology has to deal with only one set of data points for the whole HERMES data.

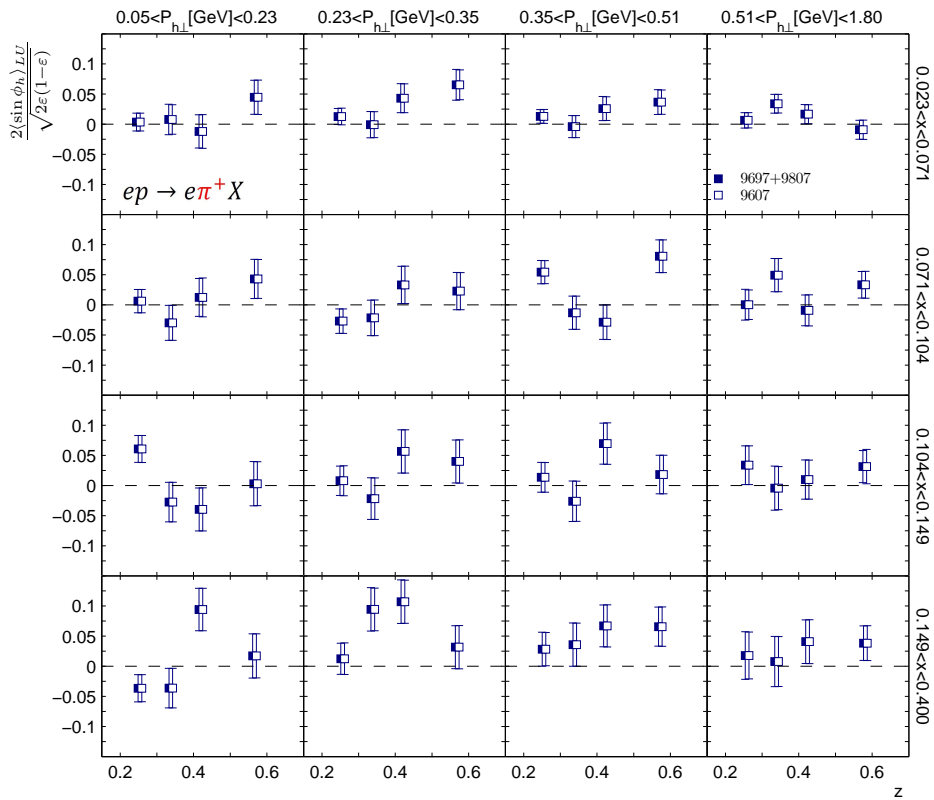


Figure 4.19: Comparison of asymmetries and their total uncertainties for the whole 1996-2007 (open symbols) and the combination of 1996-1997 + 1998-2007 (closed symbols) for the reaction $ep \rightarrow e\pi^+X$

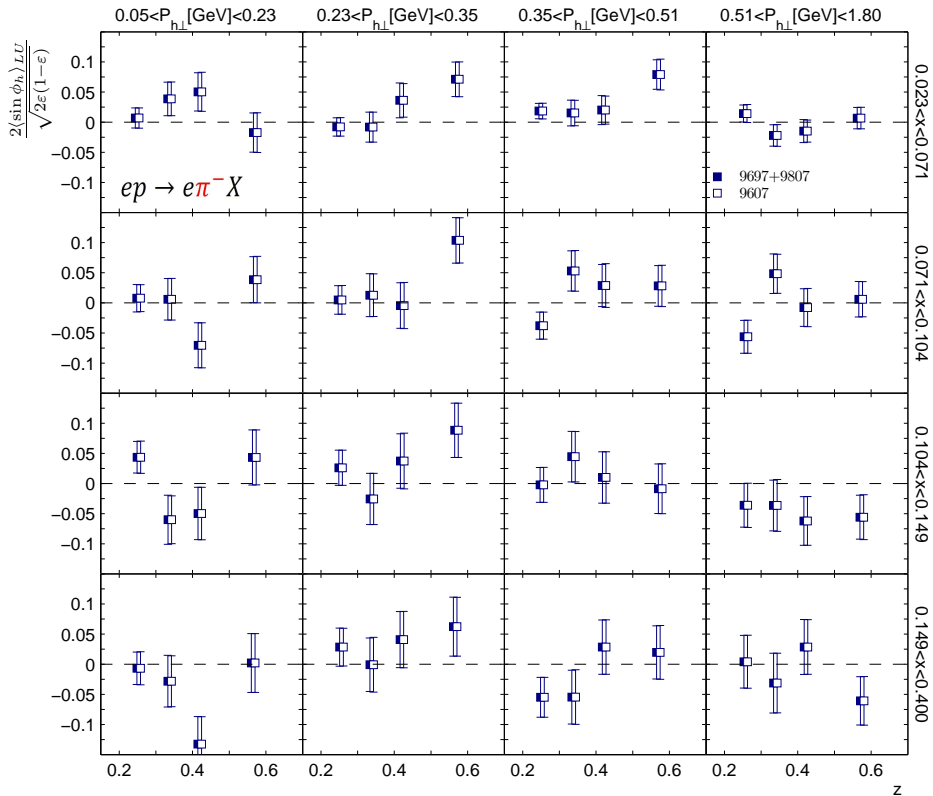


Figure 4.20: Comparison of asymmetries and their total uncertainties for the whole 1996-2007 (open symbols) and the combination of 1996-1997 + 1998-2007 (closed symbols) for the reaction $ep \rightarrow e\pi^- X$

4.8 Crosscheck of results

In order to control the obtained results, the asymmetries were extracted by a second analyzer with an independently written extraction code. The crosscheck of the results obtained for the hydrogen target can be found in figs 4.21, 4.22, 4.23. The same set of pictures for deuterium target is presented in figs. 4.24, 4.25, 4.26. Full symbols present results used in this analysis. Open symbols show the results of the second analyzer. The difference between the results is less than 1% and negligible compared to the statistical uncertainties, and can be assigned to machine inaccuracy resulting from the usage of different codes.

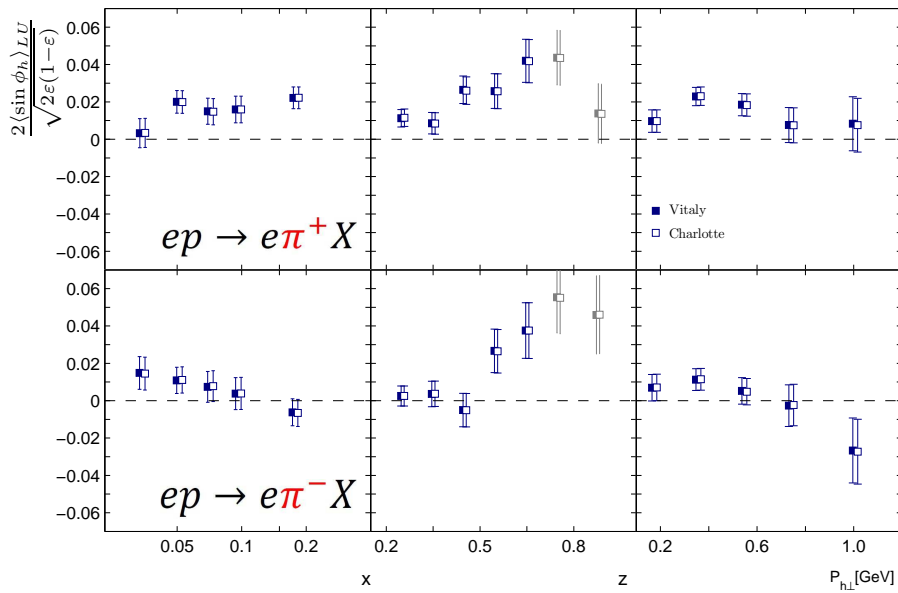


Figure 4.21: Crosscheck of pion asymmetries of 1998-2007 data collected on hydrogen target

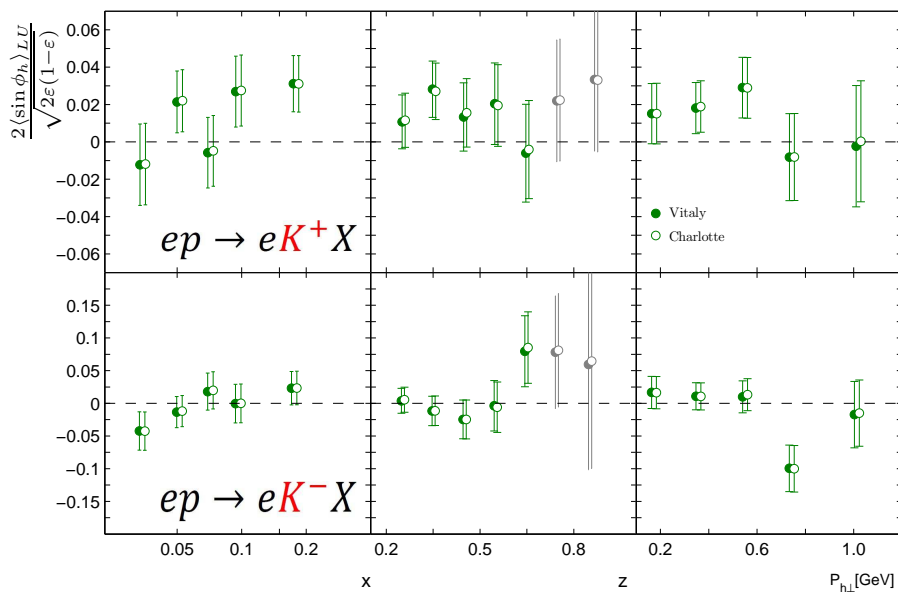


Figure 4.22: Crosscheck of kaon asymmetries of 1998-2007 data collected on hydrogen target

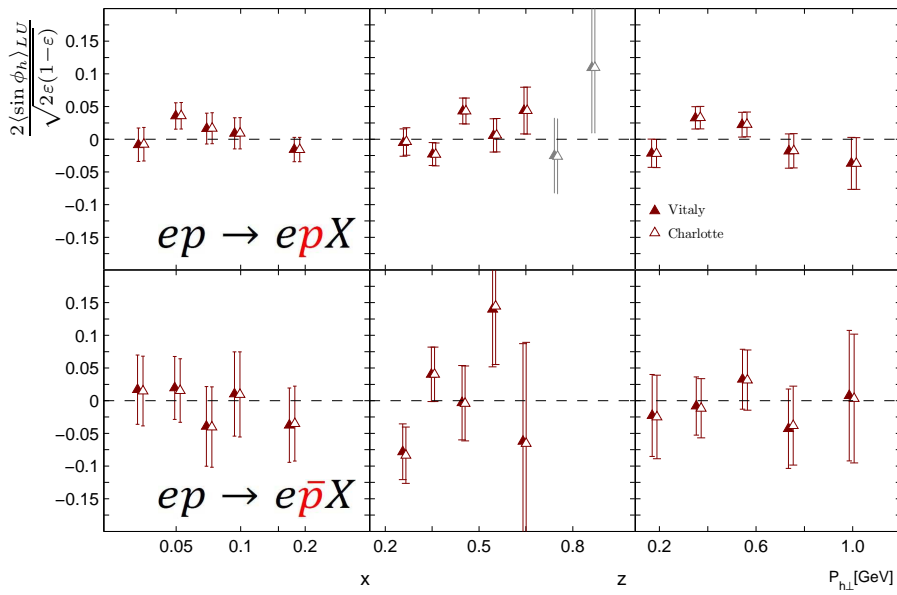


Figure 4.23: Crosscheck of (anti)proton asymmetries of 1998-2007 data collected on hydrogen target

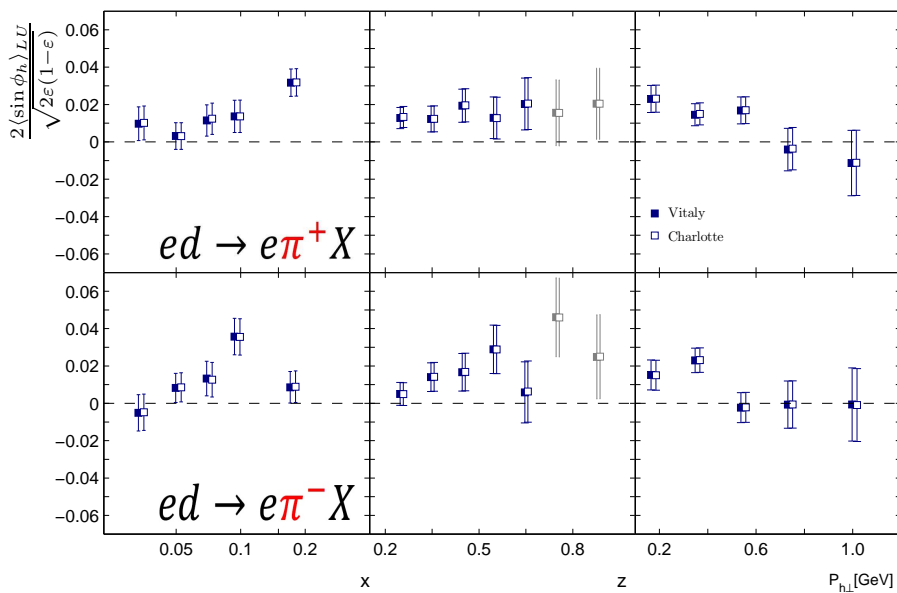


Figure 4.24: Crosscheck of pion asymmetries of 1998-2007 data collected on deuterium target

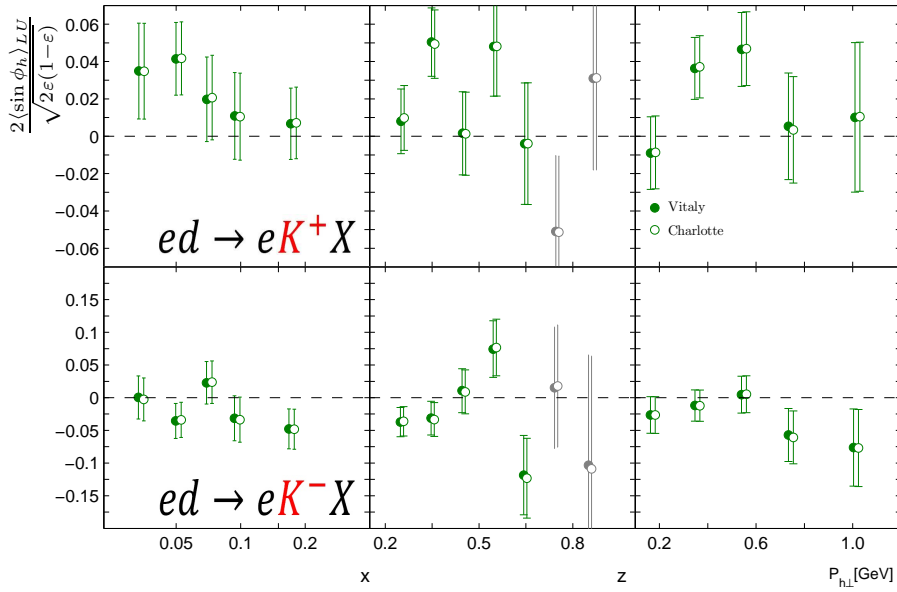


Figure 4.25: Crosscheck of kaon asymmetries of 1998-2007 data collected on deuterium target

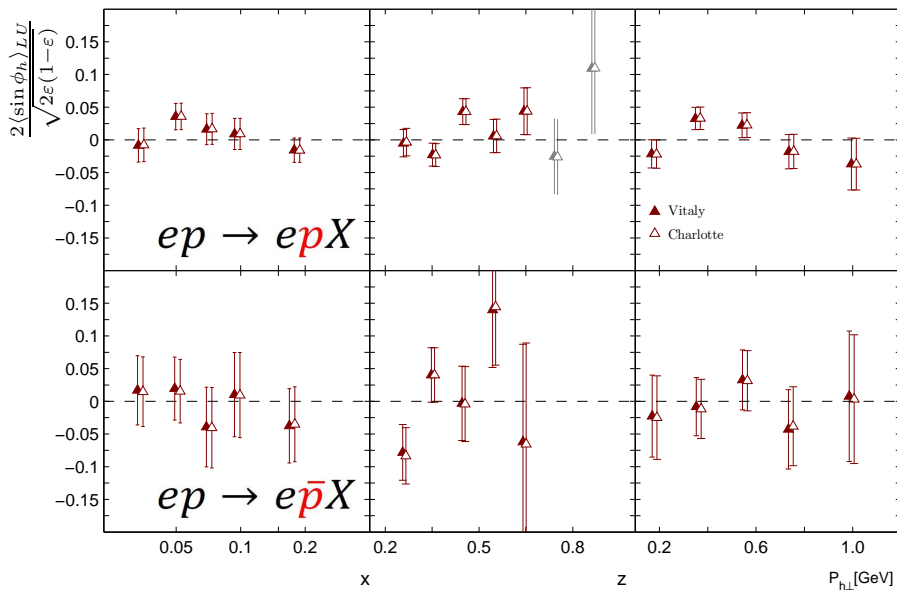


Figure 4.26: Crosscheck of (anti)proton asymmetries of 1998-2007 data collected on deuterium target

Chapter 5

Systematics

The extracted values of the asymmetries can be affected by systematic uncertainties, stemming from several sources. The contributions come from:

- RICH hadron identification.
- Fit function form
- Uncertainty in measurement of beam polarization
- Acceptance, smearing and radiative effects (3-in-1 procedure)

The final systematic uncertainty is the sum of all systematic sources except of uncertainty in measurement of beam polarization σ_{syst}^{beam} , added in quadrature, while the uncertainty from the beam polarization measurement is given as a scale uncertainty:

$$\sigma_{syst}^2 = \sigma_{syst}^{RICH^2} + \sigma_{syst}^{terms^2} + \sigma_{syst}^{3-in-1^2} \quad (5.1)$$

Taking into account also statistical uncertainty, σ_{stat} , which depends only on the number of events (statistical fluctuation), one can write next equation for value of measured variable.

$$VALUE = DATA \pm \sigma_{sys} \pm \sigma_{stat} \quad (5.2)$$

5.1 RICH unfolding procedure

As was described in section 3.3.5 the RICH detector is used to identify pions, kaons and protons at HERMES. The measured hadron yields were unfolded in the following momentum regions:

- $2 < P < 15$ GeV for pions and kaons

- $4 < P < 15$ GeV for (anti)protons

To each hadron track pion, kaon, (anti)proton weights were assigned for the efficiency of reconstruction of the track by RICH detector. It was explained in sec. 3.3.5, the weights are the elements of the P-matrices. The P-matrix values are influenced by the choice of Monte Carlo generator and the certain chosen background signal. According to the recommendations in [69] the "*disNG_{ownbkg}*" matrix values are taken as central ones. The P-matrix uses input values from SIDIS events, such as:

- momentum of the identified hadron
- type of the hadron identified by the RICH detector
- topology of the event (maximum number of tracks in one half of RICH detector)

It can be demonstrated, that the RICH unfolding procedure based on the P-matrix redistributes the yields of sign-like hadrons. On the right side of fig. 5.1 one can see the ratios of momentum distributions for corresponding hadron type before and after applying the unfolding procedure.

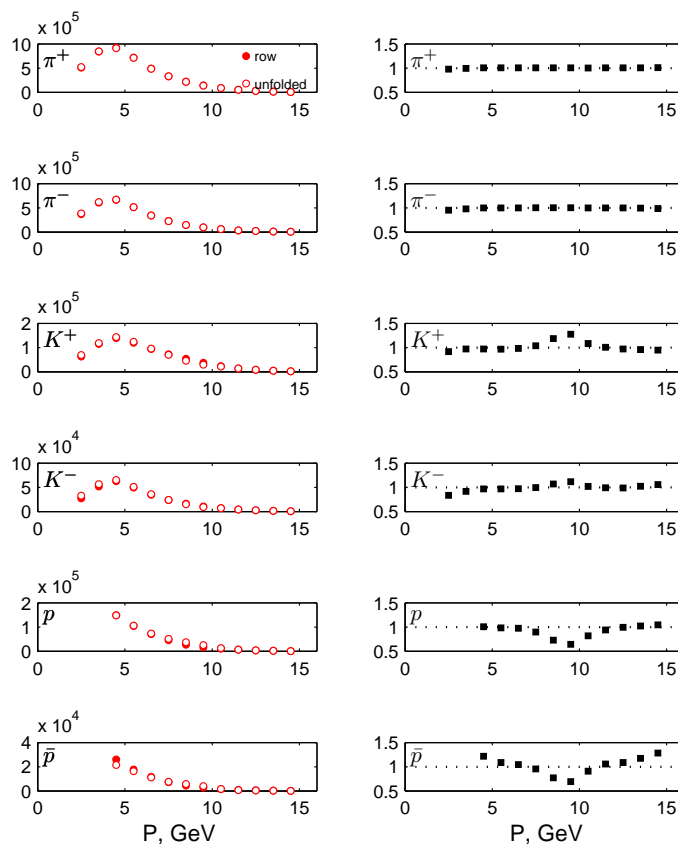


Figure 5.1: Redistribution of hadrons after the RICH unfolding procedure using P-matrix. Left side: momentum distributions of hadrons, identified by the RICH detector ("row") and corrected through P-matrix same momentum distributions ("unfolded"). Right side: ratio of "row" momentum distribution to "unfolded" one.

In fig. 5.2 asymmetries obtained after unfolding using different P-matrices are shown.

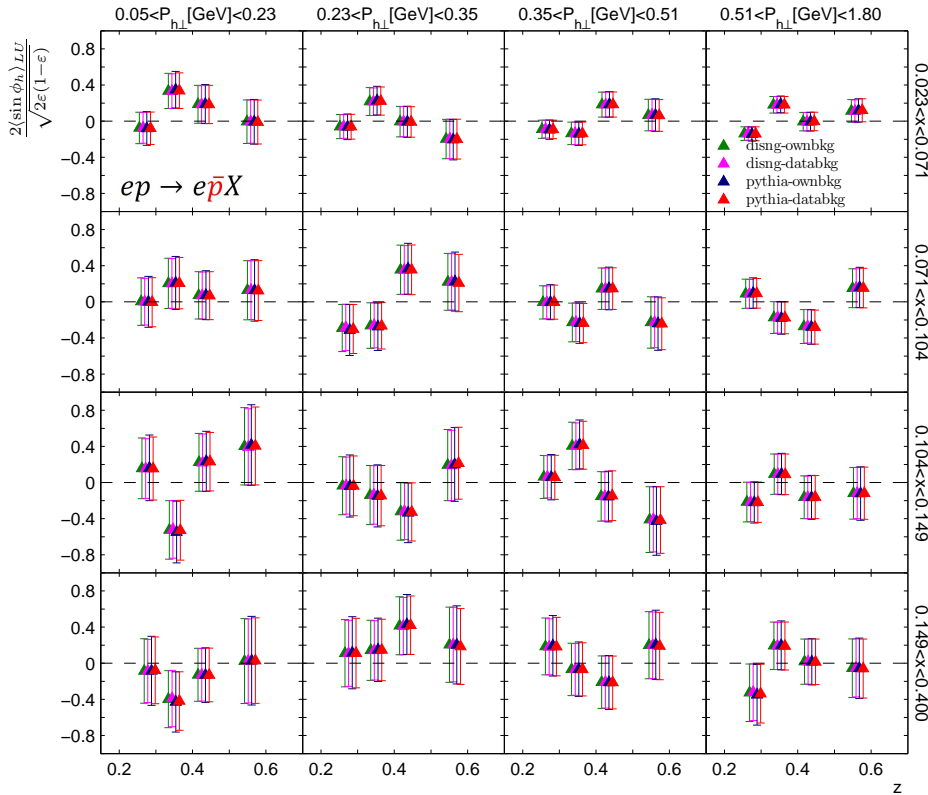


Figure 5.2: Influence of different p-matrices.

The systematic uncertainty resulting from the unfolding on the P-matrix calculated as the maximum difference between the central values (first of four triangles for each kinematic bin) and the values obtained with another P-matrix. The difference between the results obtained using different P-matrices (of the order of 1%) is tiny. It is visible only for kaons, (anti)protons. Nevertheless, for several bins it can reach up to 5% (see fig. 5.2, left bottom corner, second z-bin). Therefore, the corresponding uncertainty is taken into account.

5.2 Additional azimuthal modulations

It is expected, that they have a negligible impact on the $\sin \phi_h$ term. As a check of the stability of the fit function and of the influence of additional azimuthal terms following combinations of azimuthal modulations were proposed:

- $1 + P_i A_{LU}^{\sin \phi_h} \sin \phi_h \dots$, 1 parameter fit, which is selected in this analysis as the final one
- $1 + P_i (A_{LU}^{\sin \phi_h} \sin \phi_h + A_{LU}^{\sin 2\phi_h} \sin 2\phi_h) \dots$, 2 parameter fit, where $\sin 2\phi_h$ term only appears with the proposal of two-photon exchange (see [83]).
- $1 + A_{UU}^{\cos \phi_h} \cos \phi_h + A_{UU}^{\cos 2\phi_h} \cos 2\phi_h + P_i A_{LU}^{\sin \phi_h} \sin \phi_h \dots$, 3 parameter fit, where $\cos \phi_h$ and $\cos 2\phi_h$ are extracted unpolarized terms.

- $1 + A_{UU,fix}^{\cos \phi_h} \cos \phi_h + A_{UU,fix}^{\cos 2\phi_h} \cos 2\phi_h + P_i A_{LU}^{\sin \phi_h} \sin \phi_h \dots$, 1 parameter fit, where $A_{UU,fix}^{\cos \phi_h}$ and $A_{UU,fix}^{\cos 2\phi_h}$ are parametrizations of these terms dependent on $x, y, z, P_{h\perp}$ taken from [96]).

Extracted $A_{UU}^{\cos \phi_h}$ and $A_{UU}^{\cos 2\phi_h}$ are physical modulations convoluted with the acceptance function (see eq. 5.4). Thus, they can not be considered as pure physical modulations, like these ones extracted through elaborate technique in [96]. It can be seen from fig. 5.3 that all fits give similar results. In some bins there are not enough data points available for 3 parameter fit. In fig. 5.4 one can find the 1D results for pions. Here it is clear that the extraction of $A_{UU}^{\cos \phi_h}$ and $A_{UU}^{\cos 2\phi_h}$ terms or the extraction of $A_{LU}^{\sin 2\phi_h}$ slightly influence on $\sin \phi$ modulation. But the results stay compatible with each other. However, these modulations cause only small fluctuations of $A_{LU}^{\sin \phi_h}$. The inclusion of the parametrization of $A_{UU,fix}^{\cos \phi_h} \cos \phi_h$ and $A_{UU,fix}^{\cos 2\phi_h}$ terms leads also to negligible effect. In fig. 5.5 the extracted $A_{LU}^{\sin \phi_h}$ and $A_{LU}^{\sin 2\phi_h}$ for 1D binning are presented. It is seen, that $A_{LU}^{\sin 2\phi_h}$ fluctuates around zero, while $A_{LU}^{\sin \phi_h}$ is positive. No systematic uncertainties related to the inclusion of additional azimuthal terms were taken into account.

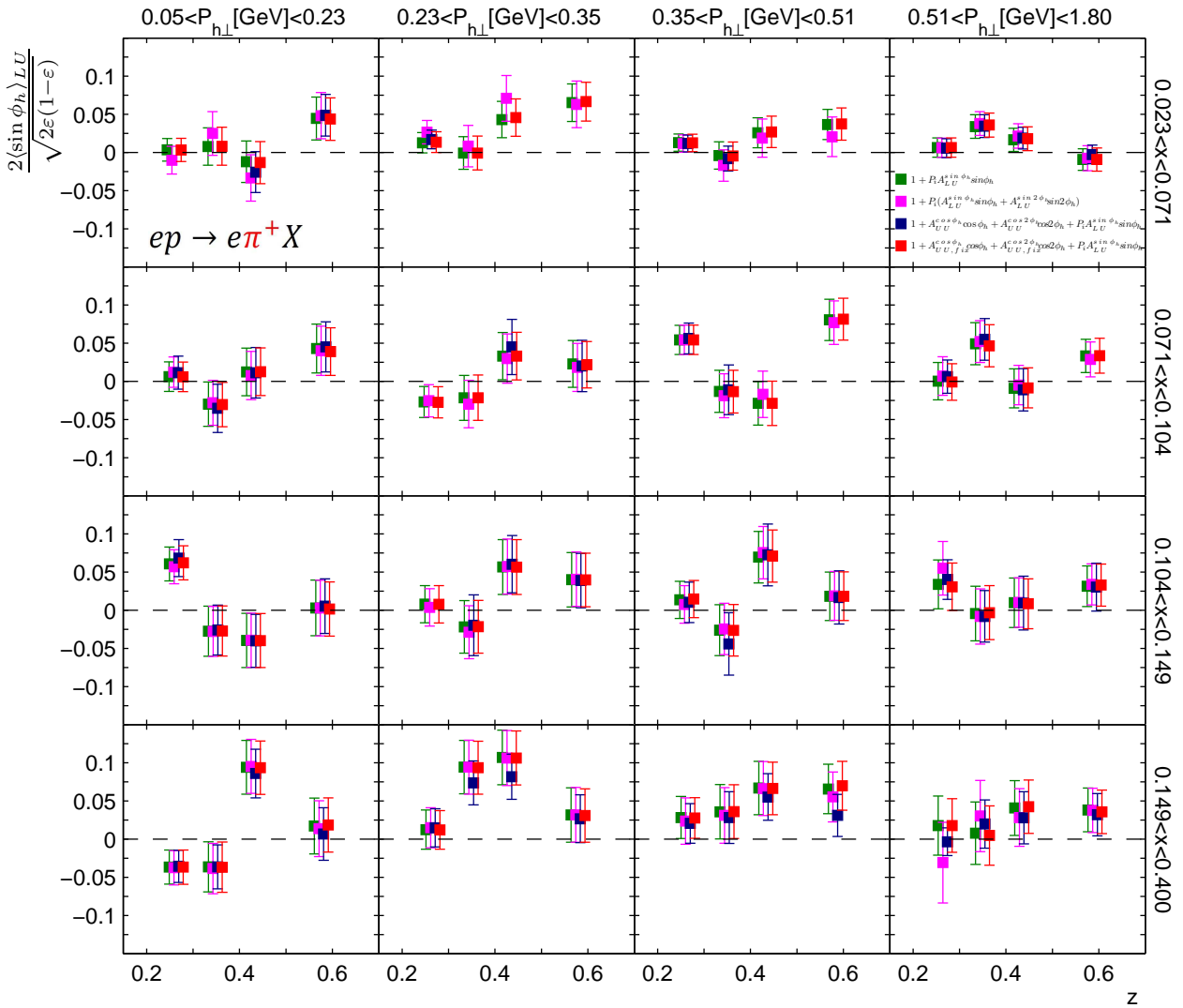


Figure 5.3: Influence of additional azimuthal modulations in 3D binning on $\sin \phi_h$ modulation

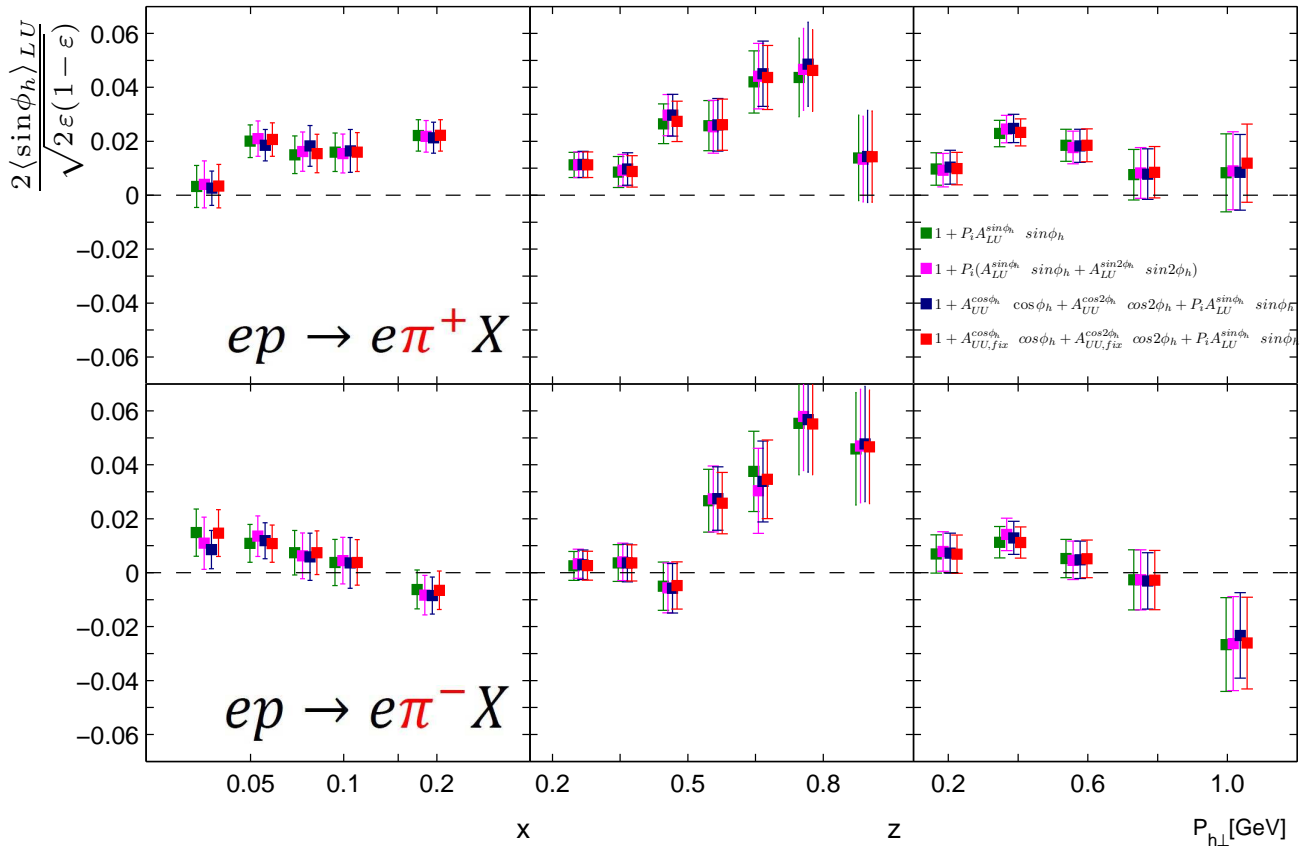


Figure 5.4: Influence of additional azimuthal modulations in 1D binning on $\sin \phi_h$ modulation

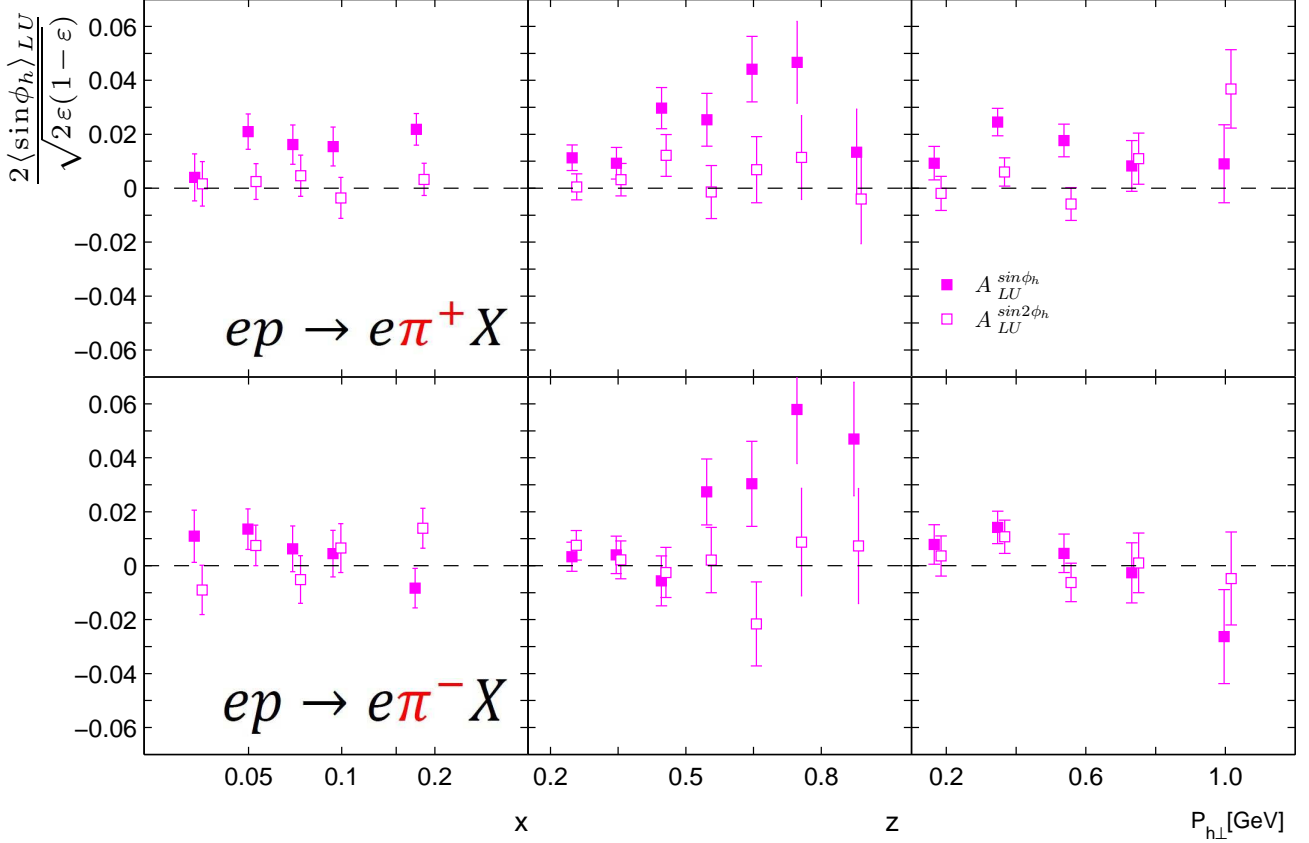


Figure 5.5: Influence of additional azimuthal modulations in 1D binning on $\sin \phi_h$ modulation

5.3 Uncertainty of measurement of beam polarization

During data collecting two polarimeters, LPOL and TPOL were used to measure the longitudinal and transverse lepton polarization. Different systematic uncertainties are induced on their respective measurements. The total uncertainty on the polarization measurement can be estimated (see [59]):

$$\sigma = \frac{L_{LPOL}}{L_{LPOL} + L_{TPOL}} \delta \frac{P}{P_{LPOL}} + \frac{L_{TPOL}}{L_{LPOL} + L_{TPOL}} \delta \frac{P}{P_{TPOL}}, \text{ where} \quad (5.3)$$

L_{LPOL} (L_{TPOL}) are collected DIS events using the LPOL (TPOL) polarimeter. The individual systematic uncertainties related to each polarization measurement are indicated as $\delta \frac{P}{P_{LPOL}}$ and $\delta \frac{P}{P_{TPOL}}$ shown in tables 5.1, 5.2 (for details see [88]):

The total uncertainty for data collected on hydrogen and deuterium targets amounts to $\sigma_{total} = 2.58\%$ and $\sigma_{total} = 2.69\%$ respectively.

A common conservatively estimated uncertainty $\sigma_{total} = 3\%$ is assigned to the results extracted on both target types.

year	DIS_{LPOL}	$\delta_{\frac{P}{P_{LPOL}}}$	DIS_{TPOL}	$\delta_{\frac{P}{P_{TPOL}}}$
96-97	0	1.6	5173915	3.26
98-00	5065353	1.6	1448871	3.26
04	1399373	2.01	896129	1.87
05	3854235	4.93	630975	4.27
06	11597696	2.75	7672796	2.45
07	14260703	2.19	6597714	2.0

Table 5.1: Beam polarization uncertainties for TPOL and LPOL for data collected on hydrogen target.

year	DIS_{LPOL}	$\delta_{\frac{P}{P_{LPOL}}}$	DIS_{TPOL}	$\delta_{\frac{P}{P_{TPOL}}}$
96-97	0	1.6	4192579	3.26
98-00	2628921	1.6	9340451	3.26
04	2225641	2.01	505897	1.87
05	4720388	4.93	499722	4.27
06	2851431	2.75	1401836	2.45
07	1650712	2.19	3142694	2.0

Table 5.2: Beam polarization uncertainties for TPOL and LPOL for data collected on deuterium target.

5.4 3-in-1 procedure

The procedure described in [91] is applied to estimate the influence of smearing, QED radiative effects and acceptance effects. Measured distributions differ from ideal ones due to smearing effects, and caused by a finite detector resolution. Radiative effects involve the possibility of photon radiation by the incoming or scattered beam lepton. The radiated photon carries a fraction of the lepton energy and therefore influences the reconstruction of the kinematic distributions. The number of events is also affected by acceptance of the spectrometer. In the ideal case, the acceptance would comprise the whole 4π phase space. The HERMES spectrometer was designed as a "forward" spectrometer and, thus, it can not detect particles flying in direction opposite to the beam. The influence of the acceptance can be represented through the acceptance function, $\epsilon(x, y, z, P_{h\perp})$. The $\epsilon(x, y, z, P_{h\perp})$ is convoluted with the cross-section according to:

$$N^{\pm}(x, y, z, P_{h\perp}, \phi_h) \sim \int \epsilon(x, y, z, P_{h\perp}, \phi_h) \sigma(x, y, z, P_{h\perp}, \phi_h) \quad (5.4)$$

The usage of a MC allows to reconstruct all generated events and estimate a possible dis-

tortion of measured distributions caused by the above described effects, σ_{3-in-1} .

The estimation of the systematic uncertainty through the 3-in-1 procedure was used for previous HERMES publications (see [91]) and consists of three steps:

- The kinematic dependence of $A_{LU}^{MODEL}(x, y, z, P_{h\perp}; a_{0\dots i})$ is extracted from the data using a Taylor expansion in the kinematic variables $x, y, z, P_{h\perp}$ around their average respective kinematics.
- The obtained model of the asymmetry is implemented in unpolarized MC sample using the true kinematics of the event.
- Asymmetries are reconstructed from a MC sample generated according to previous steps and are then compared to implemented values. The difference between the reconstructed and implemented asymmetries, $|A_{LU}^{REC} - A_{LU}^{MODEL}(x, y, z, P_{h\perp}; a_{0\dots i})|$ is taken as a systematic uncertainty of the data.

5.4.1 Parametrization of asymmetry

The kinematic dependence of A_{LU}^{MODEL} was extracted from data through a fit based on a fully differential probability density function (see Eq. 4.7). Here the $A_{LU}^{\sin\phi_h}$ amplitude is parametrized as a polynomial dependence of the asymmetry on kinematic variables. The polynomial form proposed in [91] is used, it contains terms of a Taylor expansion up to the 3^d order:

$$\begin{aligned}
A_{LU}^{MODEL}(x, y, z, P_{h\perp}; a_i) = & \\
& a_0 + a_1 \cdot x' + a_2 \cdot y' + a_3 \cdot z' + a_4 \cdot P'_{h\perp} + \\
& + a_5 \cdot x'^2 + a_6 \cdot z'^2 + a_7 \cdot P'^2_{h\perp} + a_8 \cdot x' \cdot z' + \\
& + a_9 \cdot x' \cdot P'_{h\perp} + a_{10} \cdot z' \cdot P'_{h\perp} + a_{11} \cdot x'^3 + a_{12} \cdot x' \cdot z'^2 + \\
& + a_{13} \cdot x'^2 \cdot z' + a_{14} \cdot x'^2 \cdot P'_{h\perp} + a_{15} \cdot x' \cdot P'^2_{h\perp} + a_{16} \cdot z'^2 \cdot P'_{h\perp} + \\
& + a_{17} \cdot z' \cdot P'^2_{h\perp} + a_{18} \cdot (x' \cdot P'_{h\perp})^2 + a_{19} \cdot (z' \cdot P'_{h\perp})^2 + a_{20} \cdot x' \cdot z' \cdot P'_{h\perp} + a_{21} \cdot x'^2 \cdot z' \cdot P'_{h\perp} \quad (5.5)
\end{aligned}$$

Here $x' = x - \langle x \rangle$, where x - is kinematic of the event, and $\langle x \rangle$ is the average kinematic for the data.

a_i - extracted parameters.

This function was shown in [94] to be relevant for description of transverse asymmetries. Several fit function forms inspired from the above written function were tested. The selection of the number and type of terms to be included was done using χ^2 criterion:

$$\chi^2 = \sum_n [A_{LU}^{MODEL}(x, y, z, P_{h\perp}; a_i) - A_{LU}^{DATA}]^2, \text{ where} \quad (5.6)$$

$A_{LU}^{MODEL}(x, y, z, P_{h\perp}; a_i)$... value of the model in certain kinematic bin,

A_{LU}^{DATA} ... data asymmetry in certain kinematic bin,

n ... number of kinematic bins ($n = 4 \times 4 \times 4 = 64$).

In fig. 5.6 the search of the optimal function parametrization is shown. Each blue point shows the result of χ^2 calculation for a different combination of parameters, while each panel corresponds to a different number of function parameters. The 1st panel from the left contains only one fit result for the linear form:

$$A_{LU}^{MODEL}(x, y, z, P_{h\perp}; a_i) = a_0 + a_1 \cdot x' + a_2 \cdot z' + a_3 \cdot P'_{h\perp} \quad (5.7)$$

The second panel contains the χ^2 results for the function containing four parameters $a_0 - a_3$ and additional 5th term. In the following panels each model parametrization contains an additional parameter, which is any of non-linear terms of eq. 5.5. The parameter that corresponds to the lowest χ^2 value is selected. The lowest χ^2 value is marked by a red line. Iteratively, fixing one-by-one the parameters of the model function, the final function form is:

$$\begin{aligned} A_{LU}^{MODEL}(x, y, z, P_{h\perp}; a_i) = & a_0 + a_1 \cdot x' + a_2 \cdot y' + a_3 \cdot z' + a_4 \cdot P'_{h\perp} + \\ & + a_5 \cdot z'^2 + a_6 \cdot P'^2_{h\perp} + a_7 \cdot x' \cdot z' + a_8 \cdot z' \cdot P'_{h\perp} + \\ & + a_9 \cdot z' \cdot P'^2_{h\perp} + a_{10} \cdot P'^3_{h\perp} \end{aligned} \quad (5.8)$$

It can be seen, that already with 11 parameters χ^2 stops to decrease. The found 11-parameter fit form (see eq. 5.8) was also checked to have meaningful parameter values. It means, that the parameter should not have large values (see fig. 5.7).

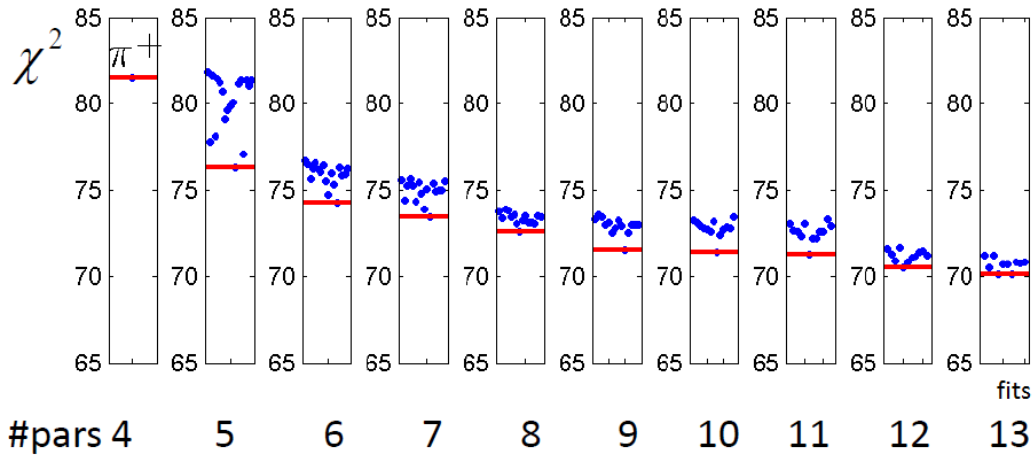


Figure 5.6: Search of model form using χ^2 criterion.

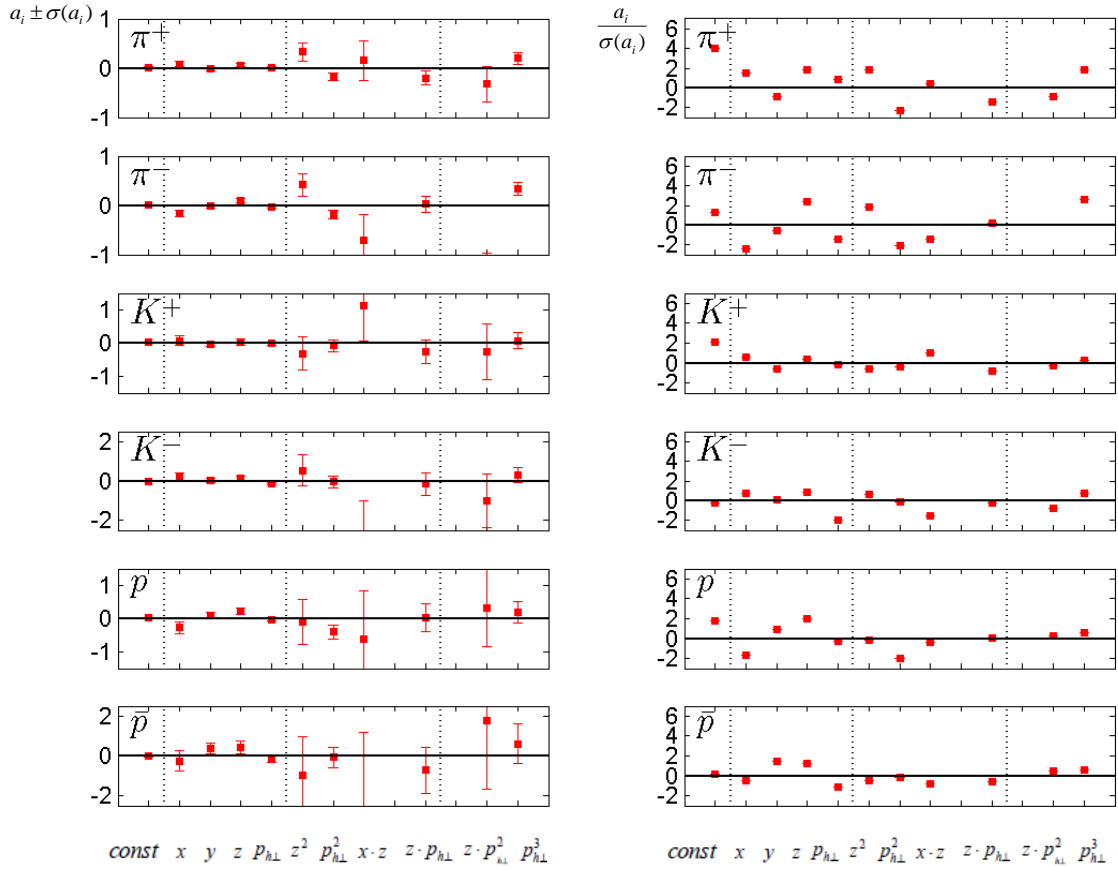


Figure 5.7: Parameter values of the model (left) and the ratio of the parameter value to its uncertainty (right).

A similar search was done with using $\chi^2_{\text{restricted}}$ criterion:

$$\chi^2_{\text{restricted}} = \frac{\sum [A_{LU}^{\text{MODEL}}(x, y, z, P_{h\perp}; a_i) - A_{LU}^{\text{DATA}}]^2}{n - p - 1}, \text{ where} \quad (5.9)$$

n - number of points ($n = 64$), p - number of parameters in fit function. The denominator ($n - p - 1$) is also called *degrees of freedom*.

The results are shown in fig. 5.8. The $\chi^2_{\text{restricted}}$ criterion has its best value already with 6 terms. However, it is expected to have more terms in the fit function for appropriate description of $A_{LU}^{\sin \phi_h}$. The following model function with 6 terms was determined:

$$A_{LU}^{\text{MODEL}}(x, z, P_{h\perp}; a_i) = a_0 + a_1 \cdot x' + a_2 \cdot z' + a_3 \cdot P'_{h\perp} + a_4 \cdot z' \cdot P'_{h\perp} + a_5 \cdot z'^2 \cdot x' \quad (5.10)$$

In figs. 5.9- 5.11 the comparison of the $A_{LU}^{\sin \phi_h}$ (stars) and its parametrizations with 6 terms (open symbols) and 11 terms (full symbols) is presented. It is clear, that the parametrization with 6 terms has worth description in $P_{h\perp}$ -projection and doesn't pass the criterion for appropriate values ($|a_i| \sim \sigma(a_i) < 1$) of the last parameter in eq. 5.10. Also, the function doesn't

contain the y-dependence, that takes into account possible correlations. Therefore, the model function with 11 parameters was chosen as the final one.

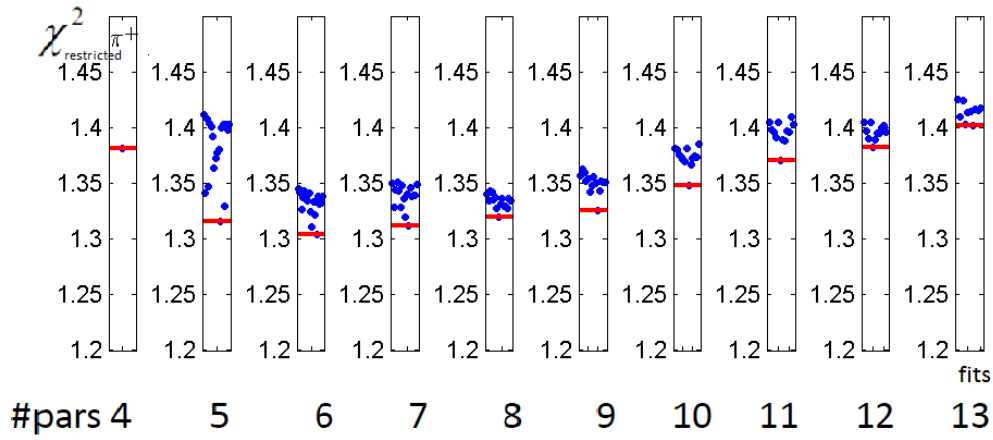


Figure 5.8: Search of model form using $\chi^2_{\text{restricted}}$ criterion.

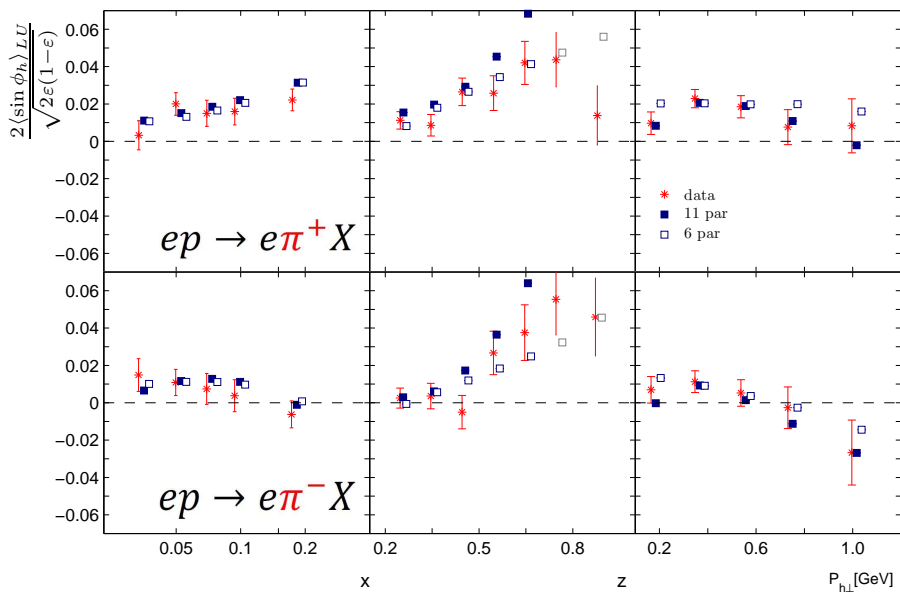


Figure 5.9: Pion asymmetries obtained from data collected on hydrogen target (stars) compared to the parametrization model with 6 terms (open symbols) and compared to parametrization model with 11 terms (full symbols)

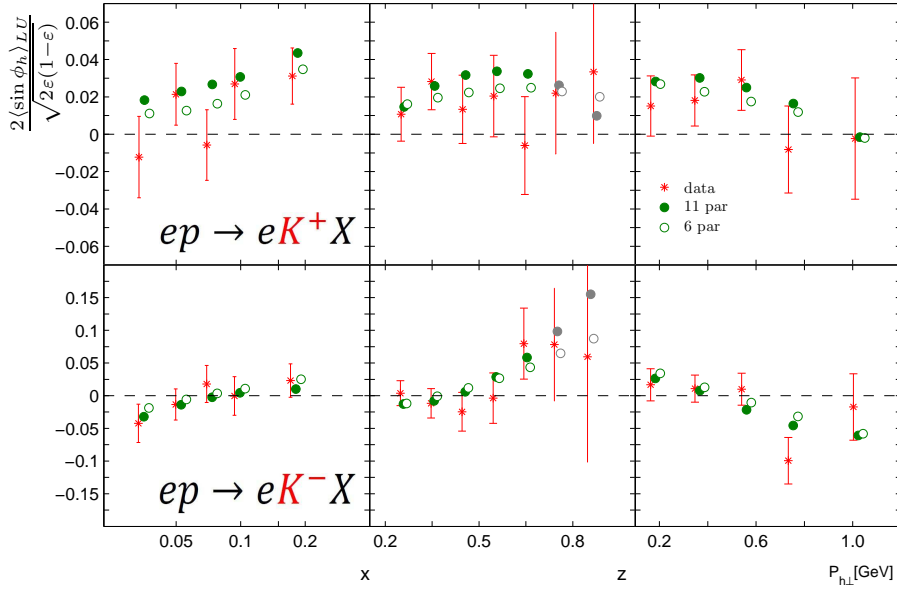


Figure 5.10: Kaon asymmetries obtained from data collected on hydrogen target (stars) compared to the parametrization model with 6 terms (open symbols) and compared to parametrization model with 11 terms (full symbols).

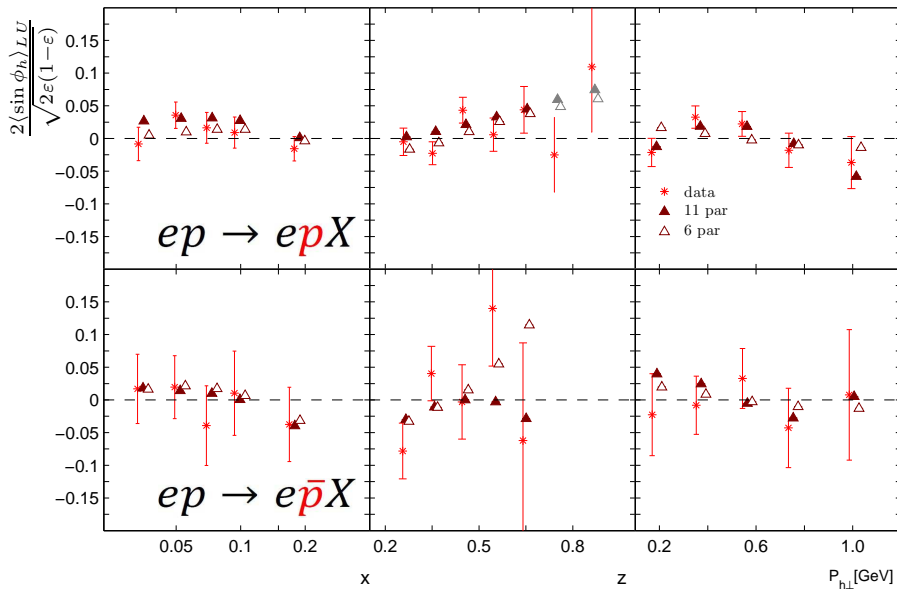


Figure 5.11: Proton and antiproton asymmetries obtained from data collected on hydrogen target (stars) compared to the parametrization model with 6 terms (open symbols) and compared to parametrization model with 11 terms (full symbols).

One can find the 3D comparison of the data model and extracted asymmetries in fig. 5.12, while the 1D is shown in figs. 5.13, 5.14, 5.15. Similar pictures are shown for the data collected on deuterium target: fig. 5.16, 5.17, 5.17.

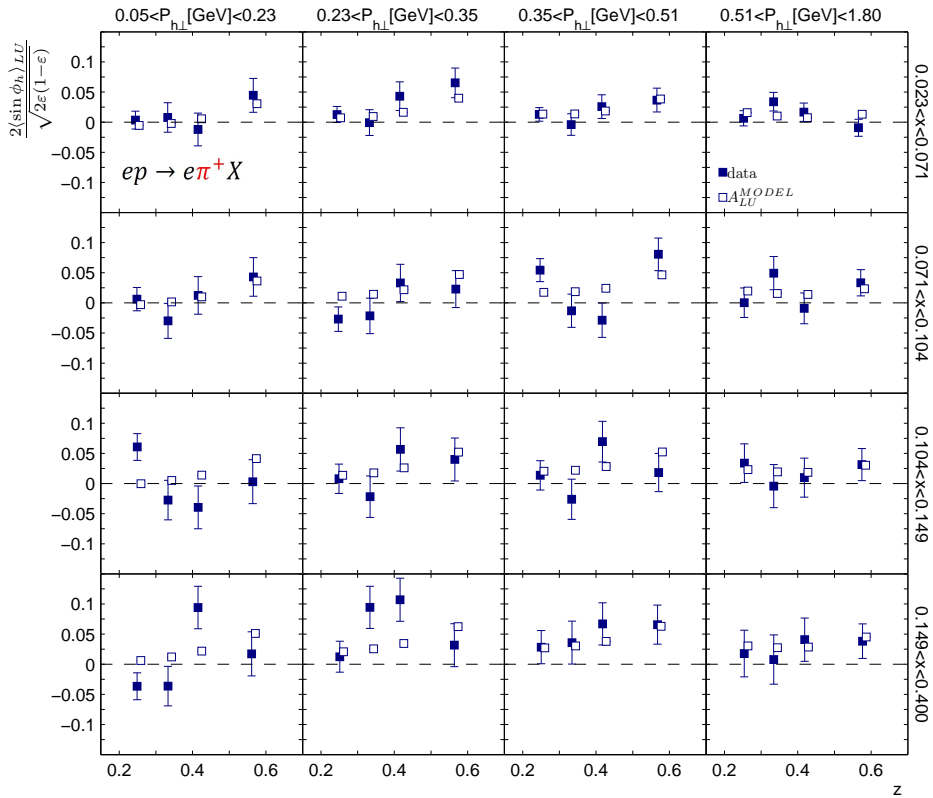


Figure 5.12: The π^+ asymmetries obtained from data collected on hydrogen target (full symbols) compared to the parametrization model (open symbols).

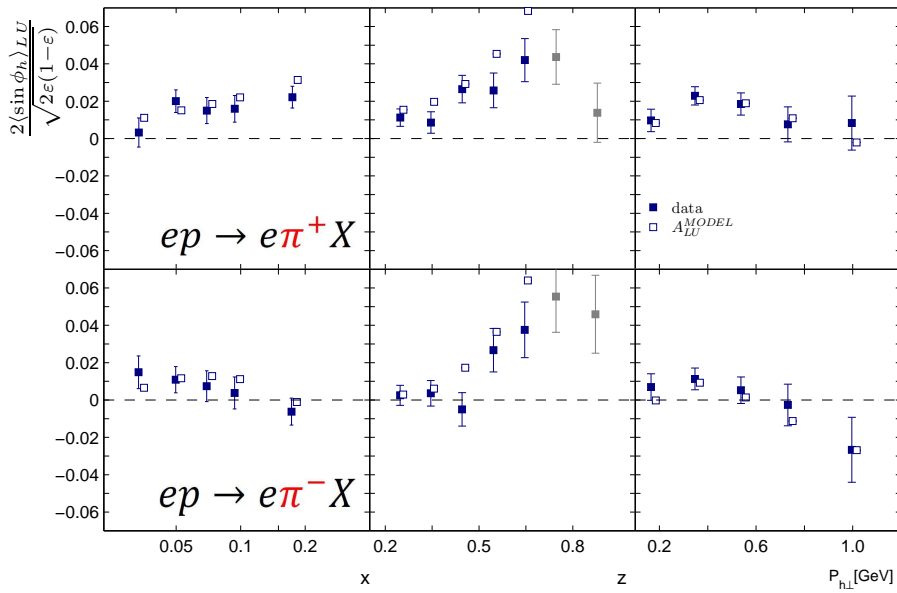


Figure 5.13: Pion asymmetries obtained from data collected on hydrogen target (full symbols) compared to the parametrization model (open symbols).

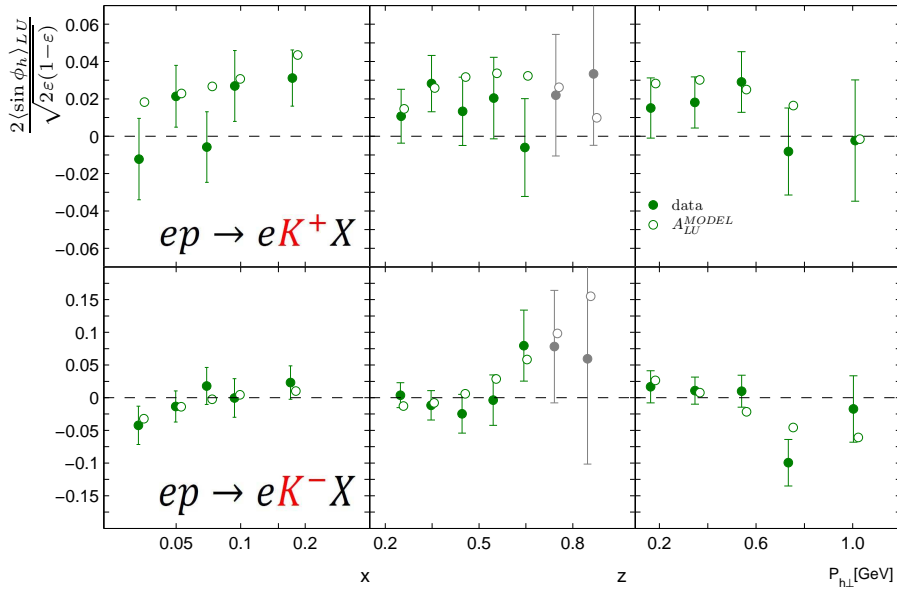


Figure 5.14: Kaon asymmetries obtained from data collected on hydrogen target (full symbols) compared to the parametrization model (open symbols).

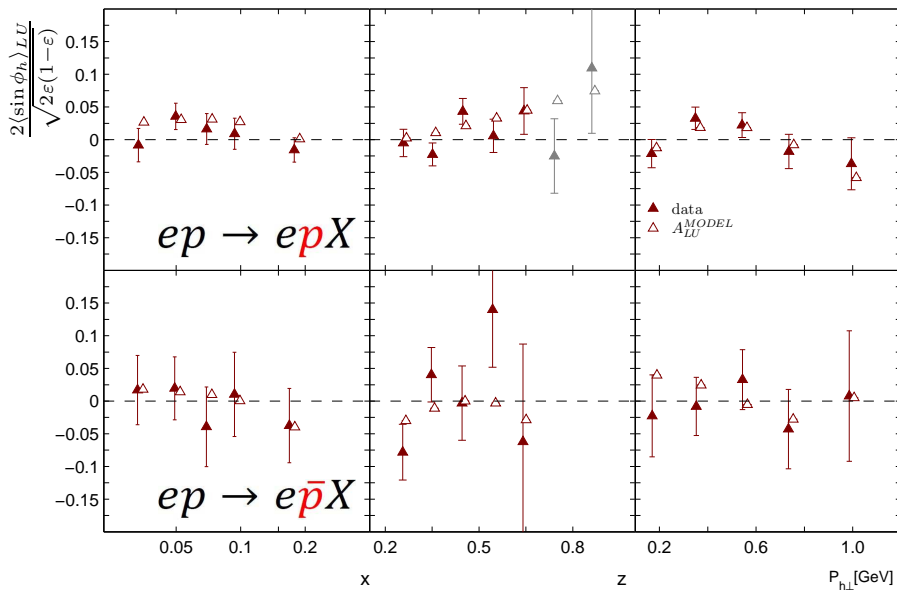


Figure 5.15: Proton and antiproton asymmetries obtained from data collected on hydrogen target (full symbols) compared to the parametrization model (open symbols).

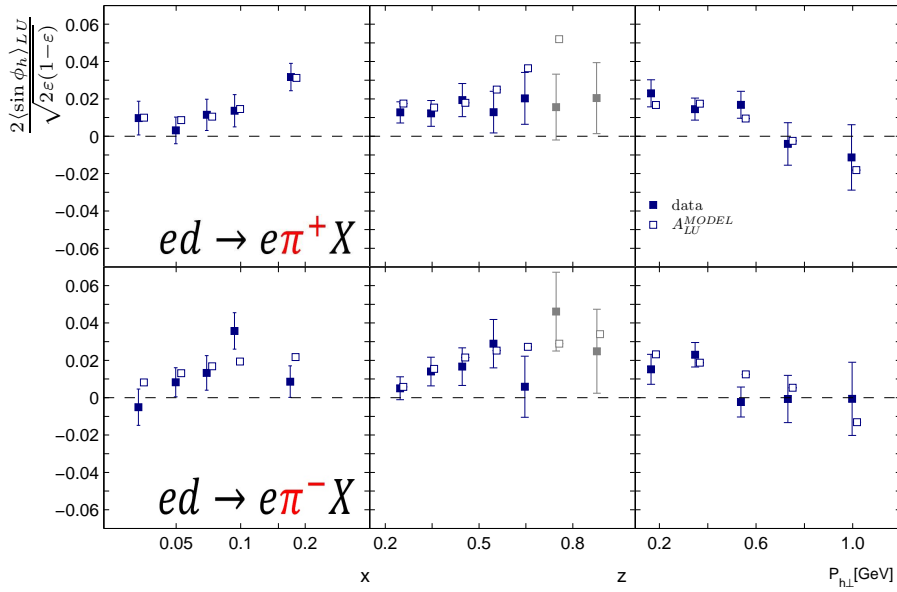


Figure 5.16: Pion asymmetries obtained from data collected on deuterium target (full symbols) compared to the parametrization model (open symbols).

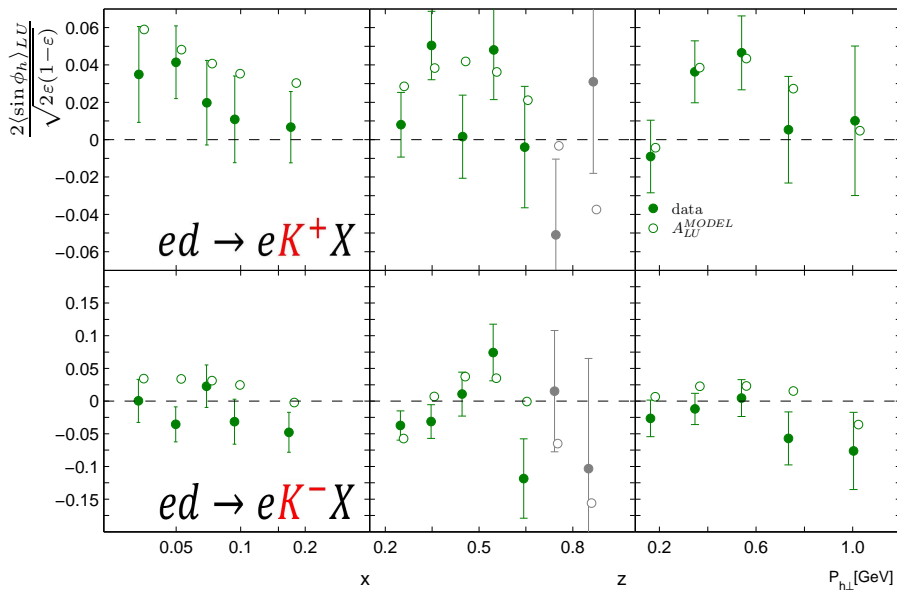


Figure 5.17: Kaon asymmetries obtained from data collected on deuterium target (full symbols) compared to the parametrization model (open symbols).

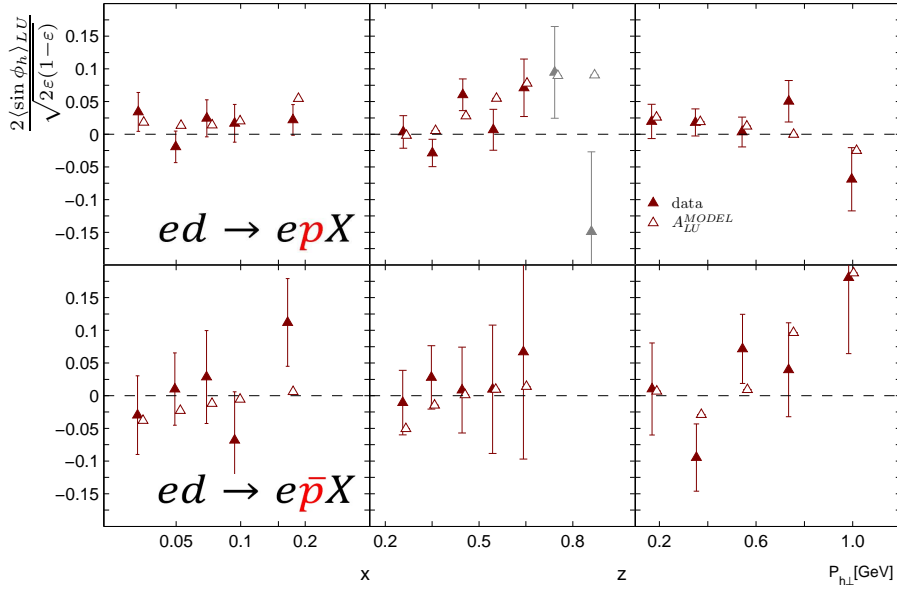


Figure 5.18: Proton and antiproton asymmetries obtained from data collected on deuterium target (full symbols) compared to the parametrization model (open symbols).

5.4.2 Implementation of asymmetries in MC

Based on eq. 4.3 we can write the spin-dependent cross-section for event with positive or negative polarization, Pol, as:

$$\begin{aligned}
 \text{Pol} > 0 : \quad \sigma^+ &= \frac{1}{2} [1 + P_i \cdot A_{LU}^{MODEL} \cdot \sin \phi_h] \\
 \text{Pol} < 0 : \quad \sigma^- &= \frac{1}{2} [1 - P_i \cdot A_{LU}^{MODEL} \cdot \sin \phi_h]
 \end{aligned} \tag{5.11}$$

In practice the implementation of asymmetry dependence into MC sample is done by assigning polarization to each event according to A_{LU}^{MODEL} applied with using true kinematics of the event from MC sample, and a uniformly distributed number r from 0 to 1:

$$\begin{aligned}
 P_i &= +1, \quad \text{if } r < \frac{1}{2} (1 + A_{LU}^{\sin \phi_h} \cdot \sin \phi_h) \\
 P_i &= -1, \quad \text{if } r > \frac{1}{2} (1 + A_{LU}^{\sin \phi_h} \cdot \sin \phi_h)
 \end{aligned} \tag{5.12}$$

The estimation of smearing and radiative effects is realized by implementing the beam-polarization dependence into MC using the true kinematics of the event. Reconstruction of the asymmetry from MC sample is done with using kinematics of reconstructed events. Therefore, the difference between the implemented asymmetry dependence A_{LU}^{MODEL} built in each kinematic bin at reconstructed kinematics and reconstructed asymmetries obtained also at reconstructed kinematics, can be taken as the summary influence (e.g. uncertainty) due to acceptance, smearing and radiation effects to the final results.

5.4.3 MC validation check

The investigation of the influence of the all described above effects is done with the help of a large sample (10 times larger than the data sample) of Monte Carlo events. Monte Carlo events were produced with the help of the PYTHIA generator [84], Radgen software [85], JETSET software based on the LUND string model [86] and the GEANT package [87]. The scheme of producing the MC event can be shown as:

$$PYTHIA \rightarrow RADGEN \rightarrow JETSET \rightarrow GEANT \rightarrow ADAMO TABLES \quad (5.13)$$

It starts from the generation of proton-electron collisions generated by PYTHIA. After that the radiative effects are taken into account by RADGEN. The fragmentation of quarks into final-state hadrons is described by the JETSET package. Finally, produced particles traverse the HERMES spectrometer. The simulation of this step is done with the help of the GEANT package. The information of the generated and reconstructed particles, their detector responses is stored in ADAMO tables in the same way as data, i.e. using the same software chain. The cross-sections of the processes and the passage of the particles through the spectrometer was tuned to HERMES kinematics. The comparison of experimental and simulated data is shown in fig. 5.19 for DIS lepton. As can be seen, the MC simulation describes the experimental data reasonably well. Similar comparison is shown in fig 5.20 for kinematics of SIDIS events.

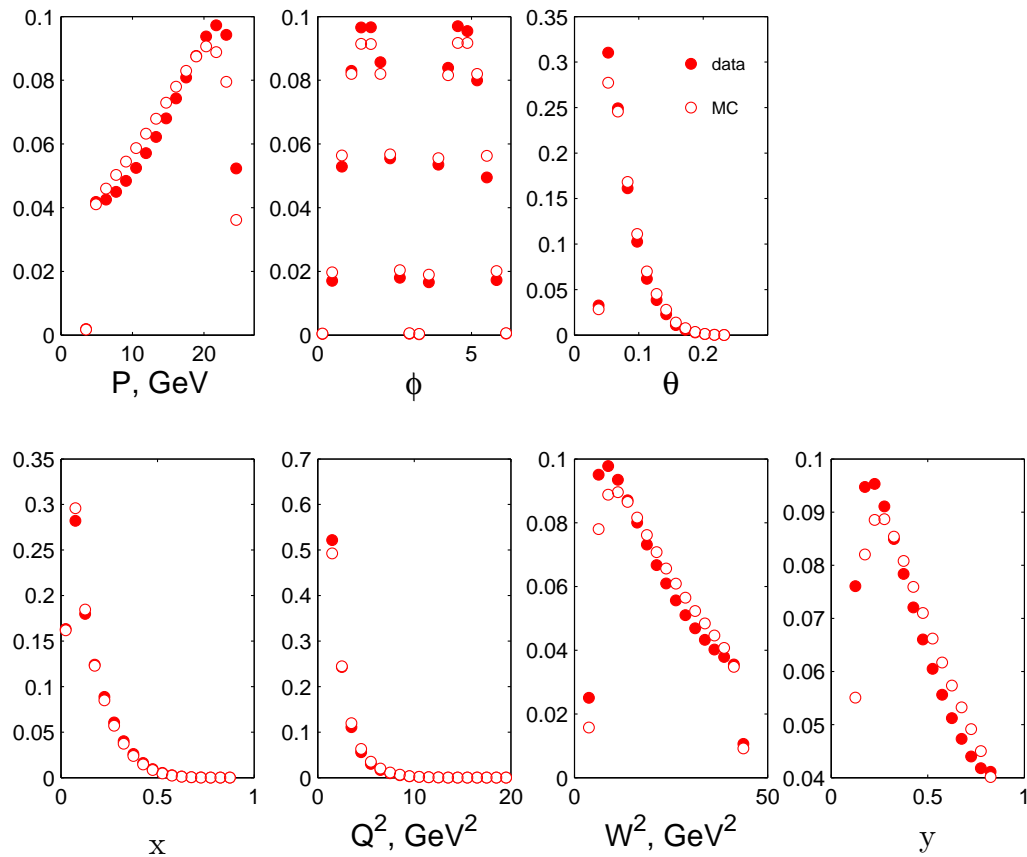


Figure 5.19: Comparison of data and MC distributions of DIS lepton

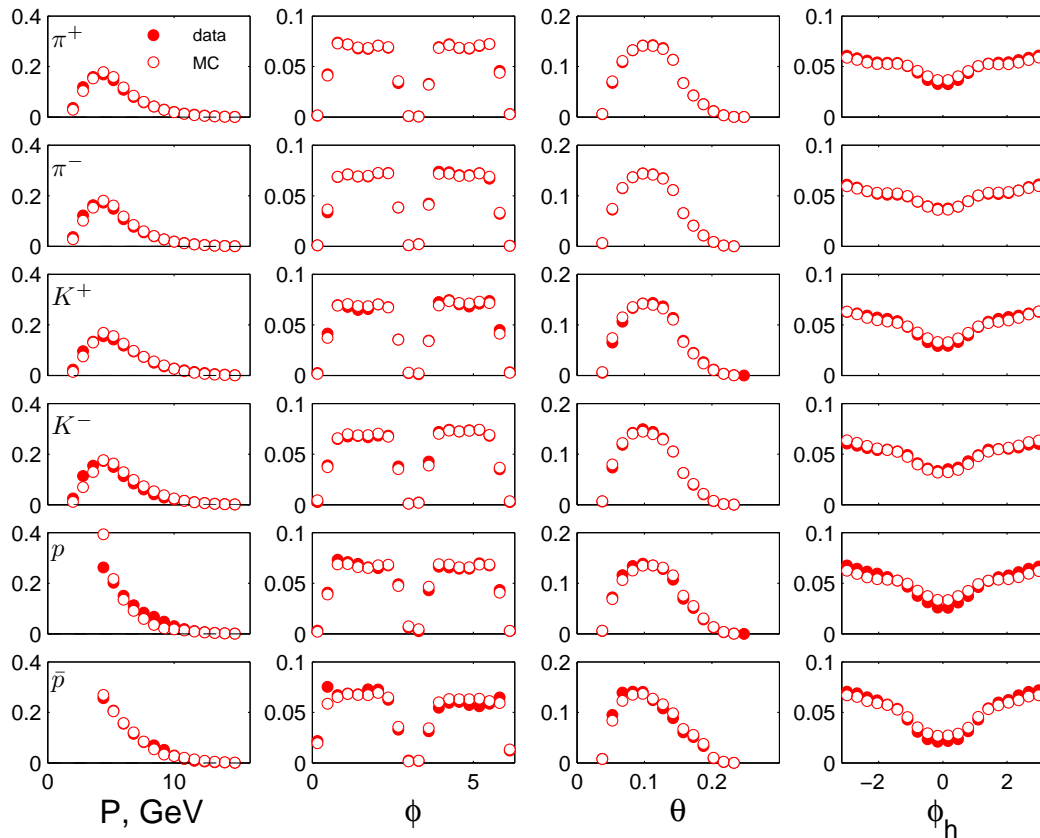


Figure 5.20: Comparison of data and MC distributions of SIDIS event

Checking only the kinematic distributions of data and MC samples is not sufficient to estimate the appropriateness of MC sample for 3-in-1 procedure. The reason that the MC does not contain the physic processes related to $A_{LU}^{\sin \phi_h}$ asymmetry or neither any of the other modulations. This is illustrated in fig. 5.21, where the asymmetries from data are shown (full symbols) as well as the asymmetries from the MC (open symbols). It is clearly seen, that MC asymmetries are consistent with zero. Therefore, the MC does not contain $\sin \phi_h$ modulation.

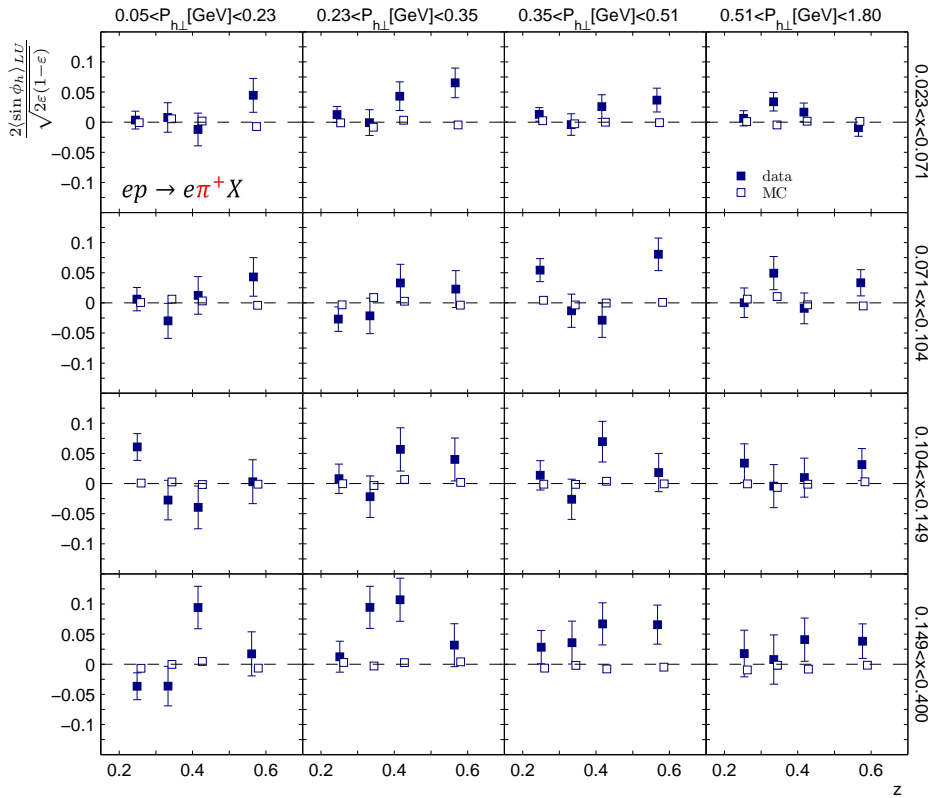


Figure 5.21: Comparison of data asymmetries (full symbols) with MC asymmetries (open symbols), extracted from MC sample, polarized by assigning completely randomly beam helicities.

The data sample also can be checked in the similar way. One can polarize the data sample in equal fractions. In fig. 5.22 it is seen, that data asymmetries are non-zero, while the asymmetries extracted from completely randomly polarized data sample fluctuate around zero. Probably for 3D case it is not obvious, but for 1D the result (see fig. 5.23) is clear. It means, that data sample doesn't contain fake asymmetry.

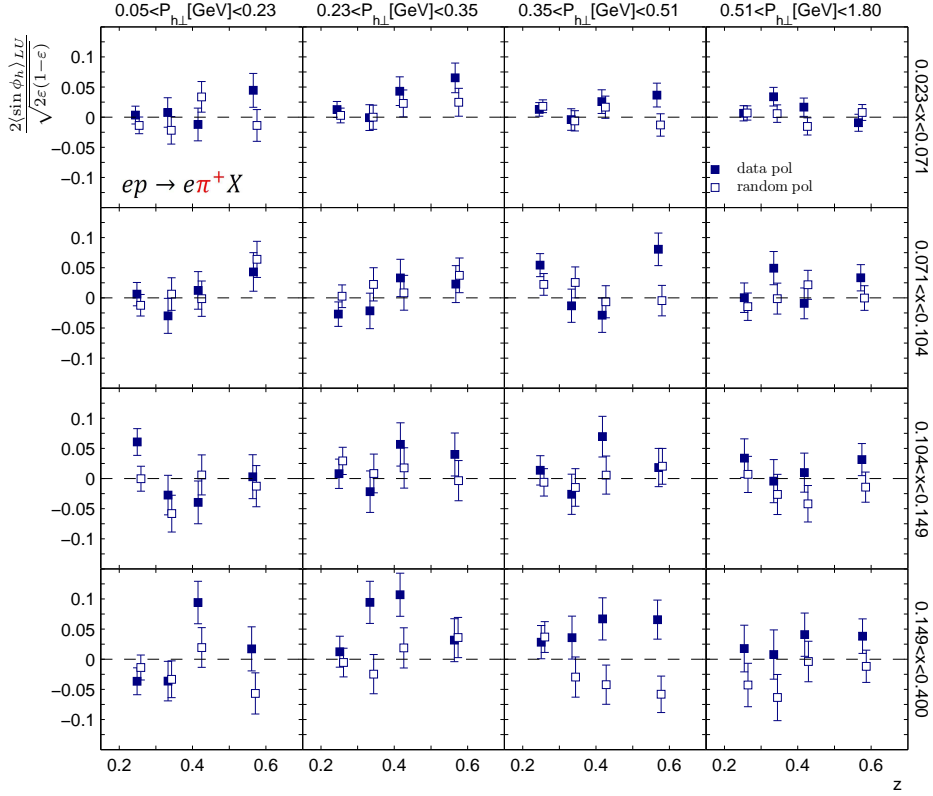


Figure 5.22: Comparison of data asymmetries (full symbols) with data asymmetries (open symbols), extracted from data sample, polarized in equal fractions

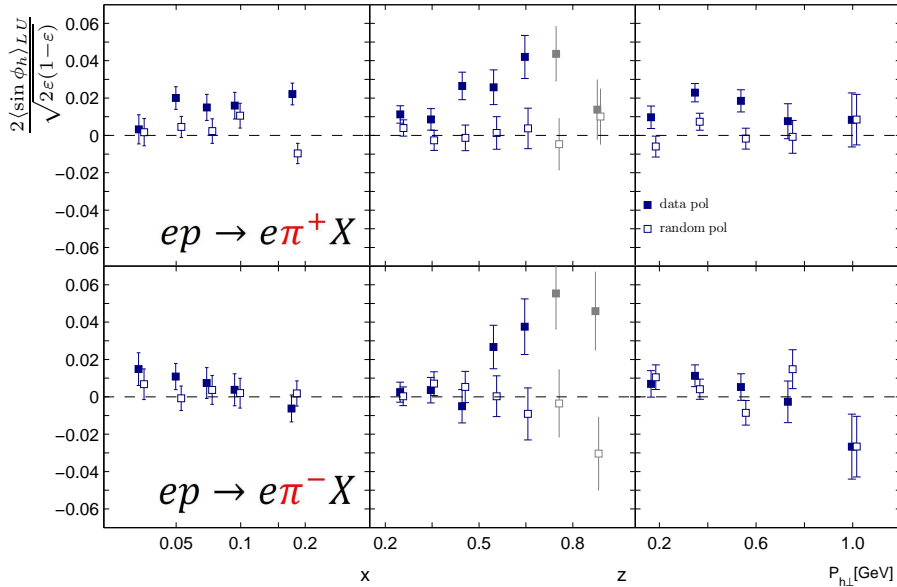


Figure 5.23: Comparison of data asymmetries (full symbols) with data asymmetries (open symbols), extracted from data sample, polarized in equal fractions

It is useful to estimate the description of the data asymmetries by the MC reconstructed asymmetries. The comparison of asymmetries extracted from data collected on hydrogen target (data) and its corresponding reconstructed from MC asymmetries (A_{LU}^{REC}) in fig. 5.24 for 3D results and in figs. 5.25- 5.27 for 1D is presented. One can see reasonable description of the data by MC.

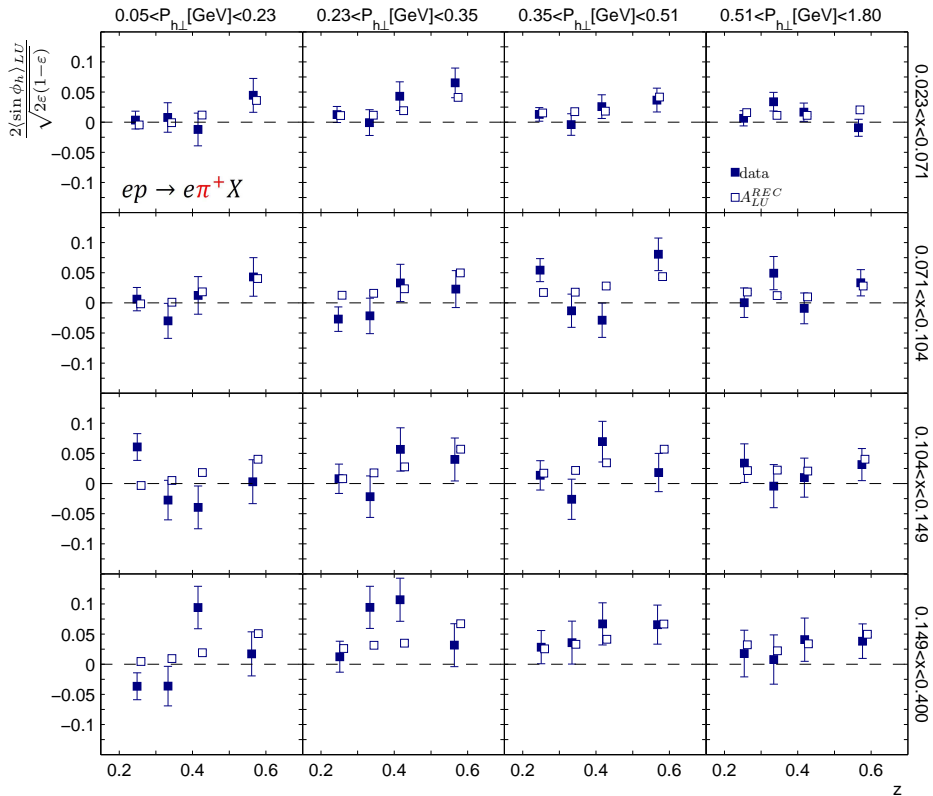


Figure 5.24: Comparison of data asymmetries (full symbols) with reconstructed MC asymmetries (open symbols) that used in the simulation a model parametrization of the asymmetry fit to HERMES data.

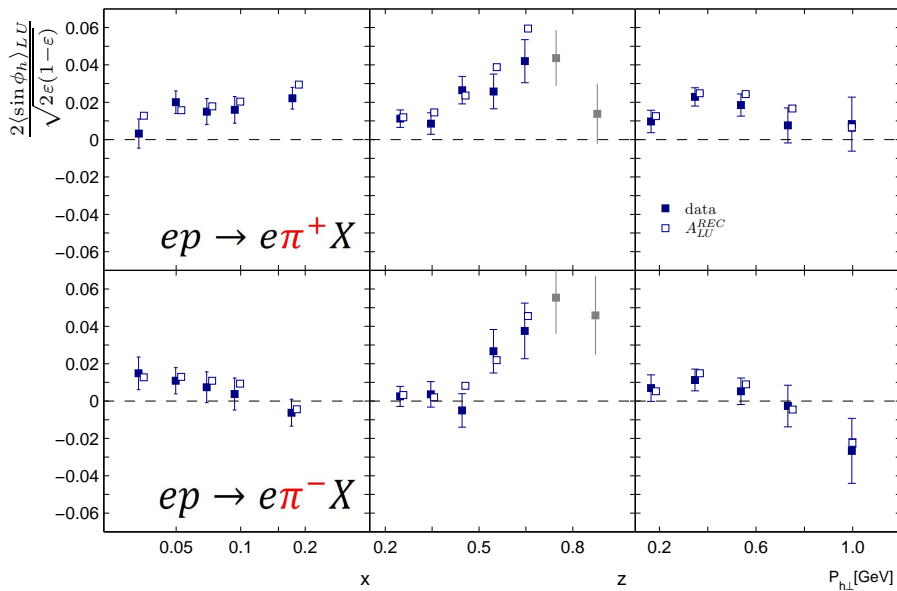


Figure 5.25: Comparison of data asymmetries (full symbols) with reconstructed MC asymmetries (open symbols) that used in the simulation a model parametrization of the asymmetry fit to HERMES data.

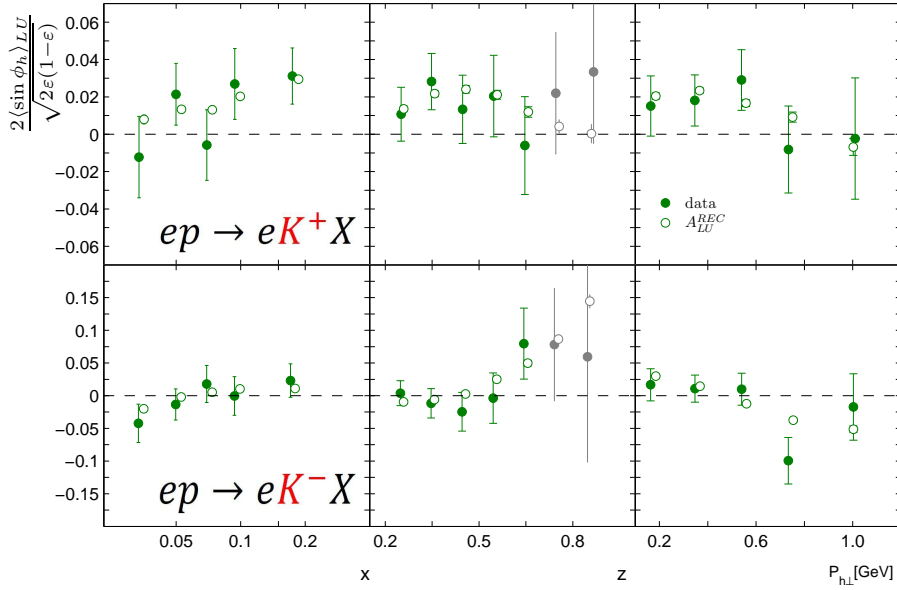


Figure 5.26: Comparison of data asymmetries (full symbols) with reconstructed MC asymmetries (open symbols) that used in the simulation a model parametrization of the asymmetry fit to HERMES data.

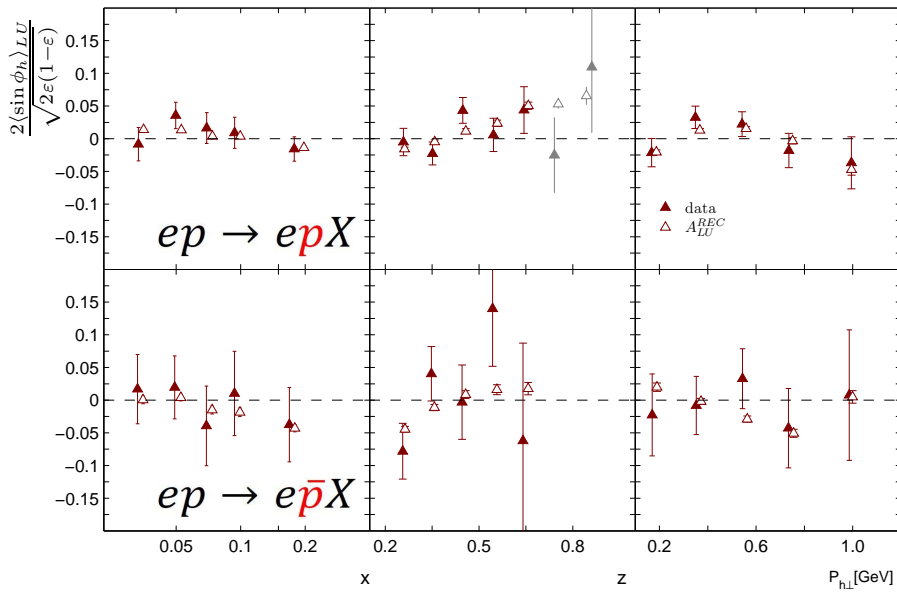


Figure 5.27: Comparison of data asymmetries (full symbols) with reconstructed MC asymmetries (open symbols) that used in the simulation a model parametrization of the asymmetry fit to HERMES data.

The shown above comparisons allow to use the MC sample in 3-in-1 procedure.

5.4.4 Uncertainty due to acceptance, smearing and radiation effects

The difference between the reconstructed asymmetries and the implemented model, $|A_{LU}^{REC} - A_{LU}^{MODEL}(x, y, z, P_{h\perp}; a_{0..i})|$, can be obtained from fig. 5.28 for the 3D and from fig. 5.30 for the 1D binning respectively. The observed difference is taken as the systematic uncertainty of 3-in-1 procedure. The comparison between statistical and systematic uncertainties is shown in

fig. 5.29 for the 3D and in fig 5.31 for the 1D respectively. For the 3D case the uncertainties obtained from 3-in-1 procedure are quite small, while for the 1D case these uncertainties are compatible to the statistical uncertainties.

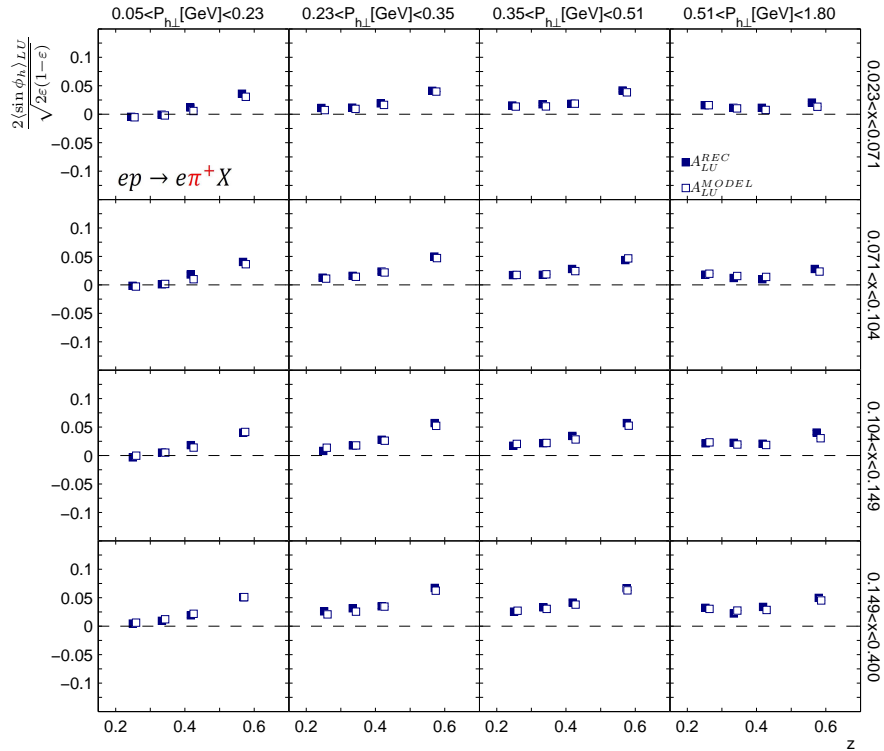


Figure 5.28: Comparison in 3D of reconstructed MC (full symbols) asymmetries with the implemented model (open symbols).

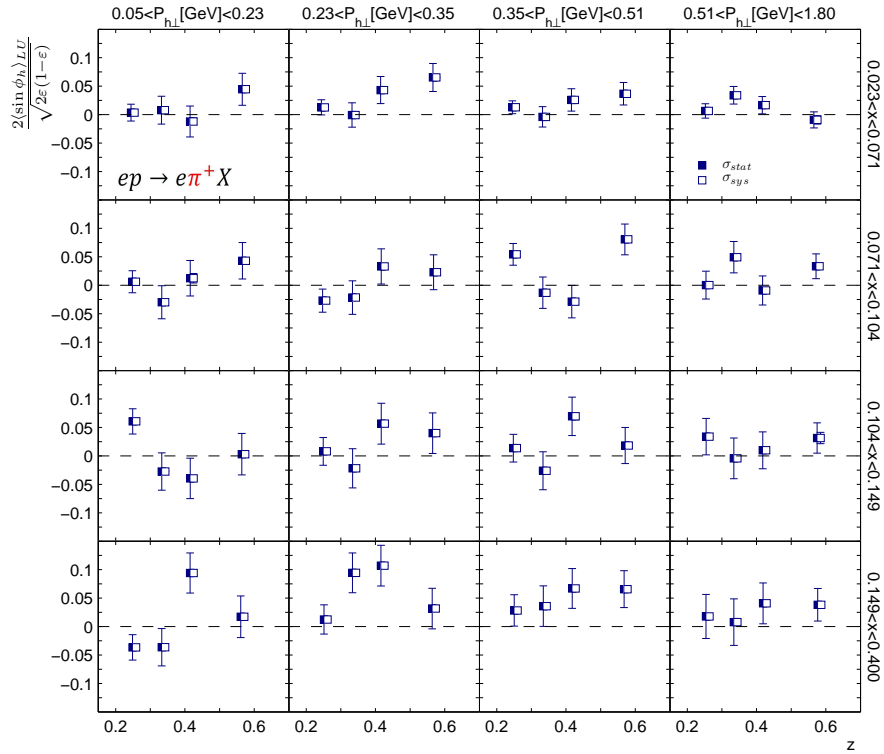


Figure 5.29: Comparison in 3D of the statistical (vertical bars going from full symbols) and systematic (vertical bars going from empty symbols) uncertainties of the data.

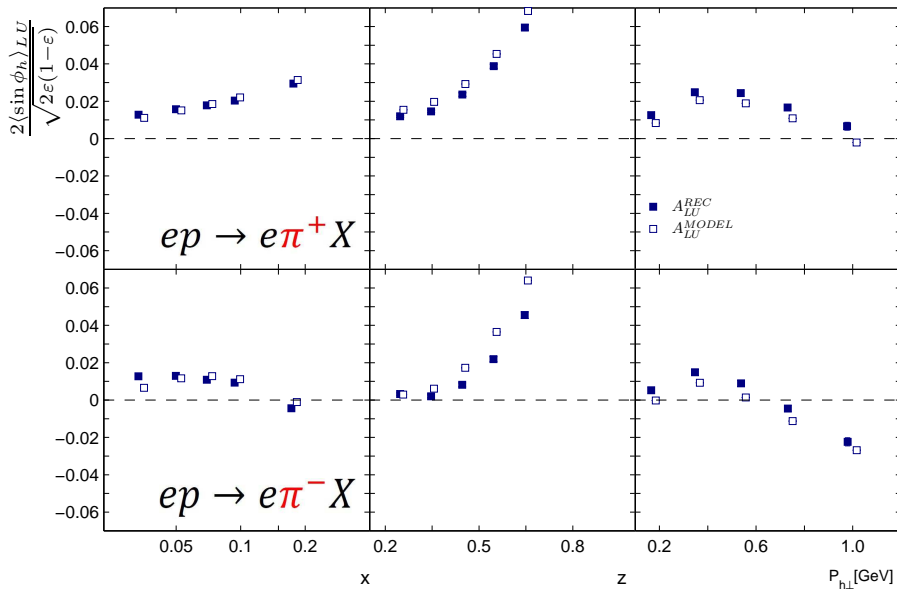


Figure 5.30: Comparison in 1D of reconstructed MC (full symbols) asymmetries with the implemented model (open symbols).

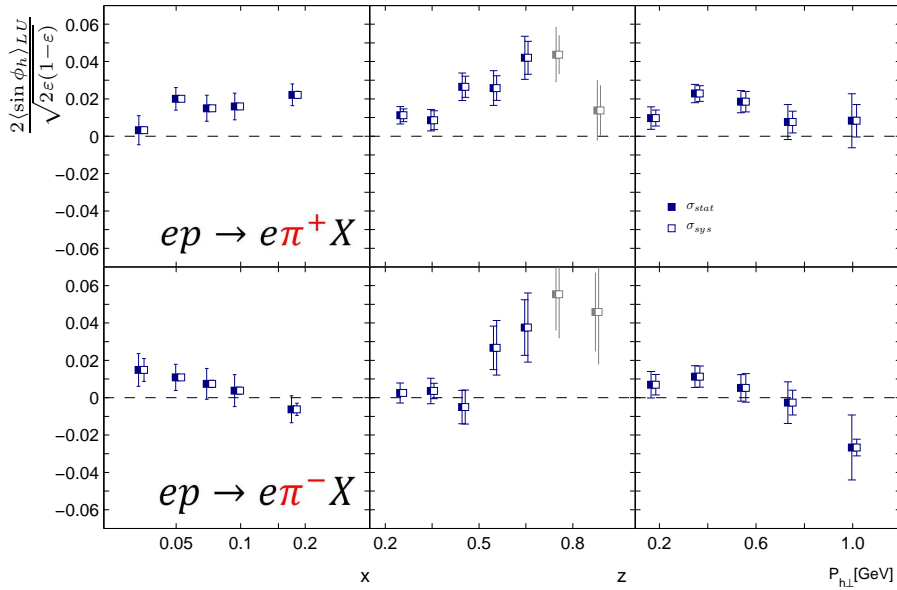


Figure 5.31: Comparison in 1D of the statistical (vertical bars going from full symbols) and systematic (vertical bars going from empty symbols) uncertainties of the data.

5.5 Total systematics

The total systematic uncertainty consists of the sum of uncertainties originating from the P-matrices in the RICH unfolding procedure and from the uncertainty of 3-in-1 procedure, which is an estimate of acceptance, radiation and smearing effects. The total uncertainty σ of the data point is represented in the figures as $\sigma = \sqrt{\sigma_{stat}^2 + \sigma_{sys}^2}$, with the statistical and systematic uncertainties indicated as σ_{stat} and σ_{sys} respectively. The beam polarization uncertainty is not taken into quadrature, but is assigned as scaling uncertainty in percents of asymmetry value.

Chapter 6

Final results

As explained in sec. 4.3, the two kinds of $A_{LU}^{\sin\phi_h}$ asymmetries are extracted. Both are shown in fig. 6.1 for SIDIS reaction $ep \rightarrow e\pi^+X$. It is seen, that both asymmetries have similar kinematic dependence, but VPA asymmetry has larger amplitudes and larger statistical uncertainties because of ε factor taken into account.

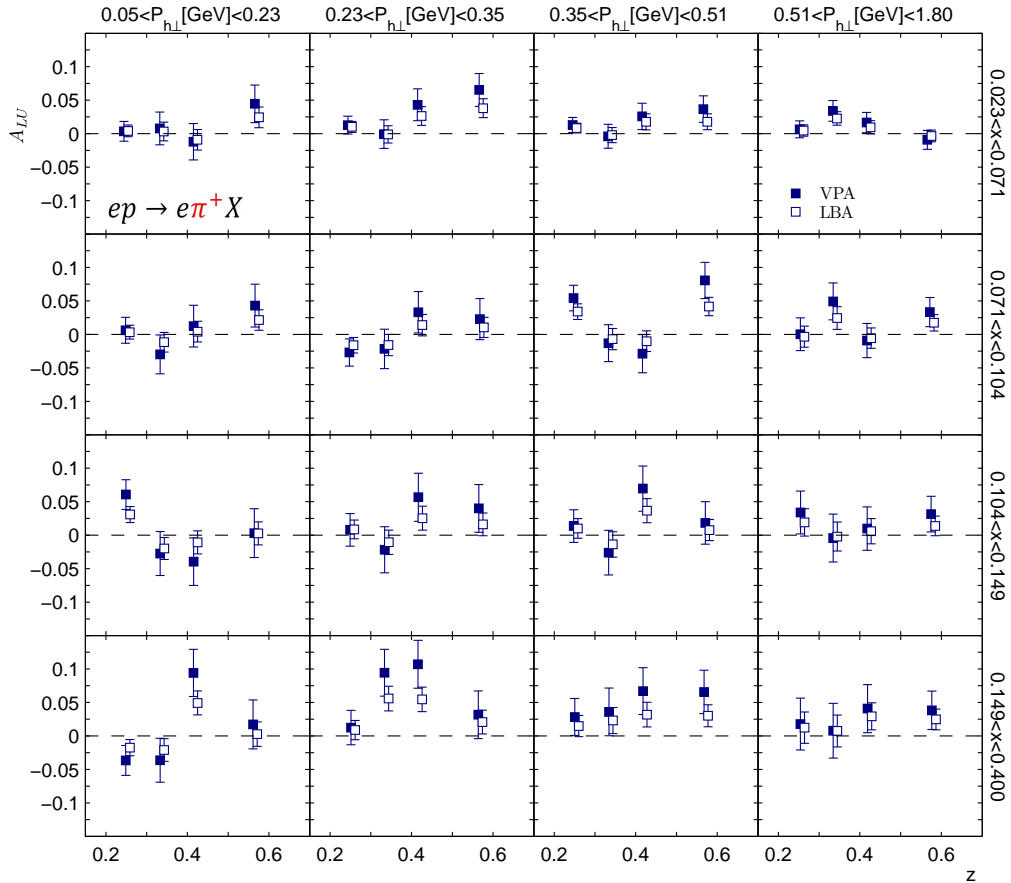


Figure 6.1: The π^+ asymmetries obtained from hydrogen data according to eq. 4.8 (full symbols) and according to eq. 4.7 (empty symbols).

The LBA and VPA spin asymmetries were extracted through ML fits using formulas 4.7,

4.8. Asymmetry values were corrected as indicated in chapters 4, 5, for different contributions such as charge symmetric background, RICH and polarimeter efficiency and the spectrometer acceptance. In fig. 6.2, 6.3 the asymmetries extracted in 3D case from the hydrogen target are indicated as full symbols, and asymmetries extracted from the deuterium target are indicated as open symbols. For the 1D case the asymmetries can be found: for pions in fig. 6.5, 6.4, for kaons in fig. 6.7, 6.6, for protons and antiprotons in fig. 6.9, 6.8. One can see in the 1D plots that π^+ and π^- asymmetries extracted from hydrogen and deuterium targets both are positive, in general increase with increasing z for the low- z and middle- z and slightly decrease in the high- z region. For the $P_{h\perp}$ -projection, general trend of decreasing asymmetries with increasing $P_{h\perp}$ is observed. The K^+ asymmetries are slightly positive for all projections without showing any pronounced dependence. The K^- , p , and \bar{p} asymmetries are consistent with zero. The lack of statistics precludes conclusive observations of special kinematic dependencies.

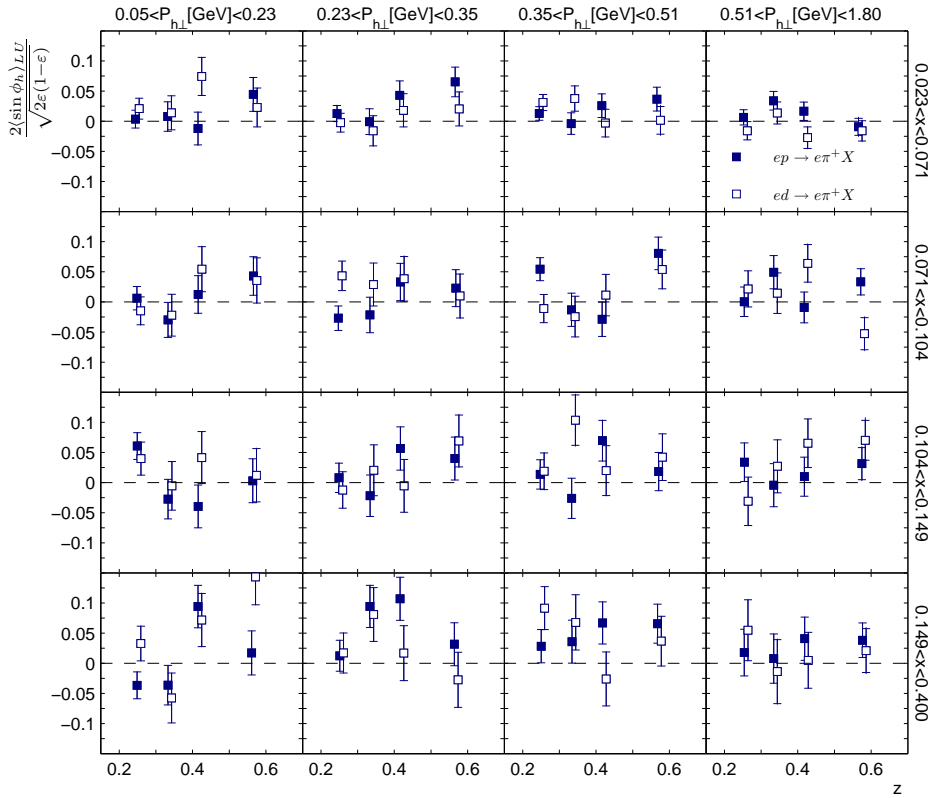


Figure 6.2: Comparison in 3D of VPA π^+ asymmetries for data collected on the hydrogen target (full symbols) versus asymmetries for data collected on the deuterium target (open symbols).

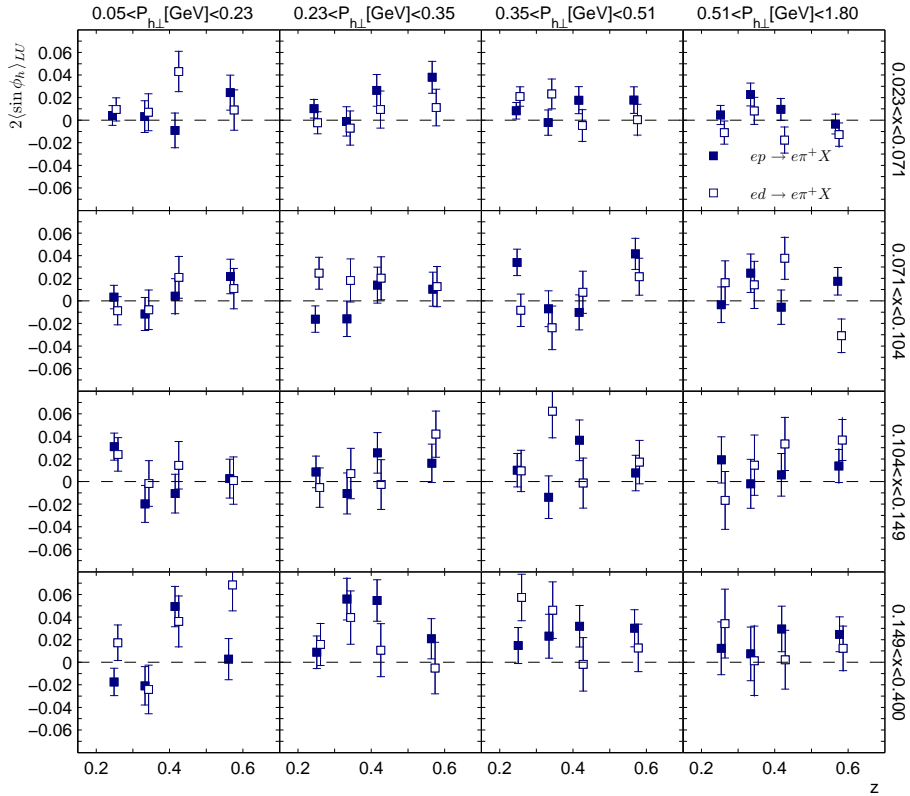


Figure 6.3: Comparison in 3D of LBA π^+ asymmetries for data collected on the hydrogen target (full symbols) versus asymmetries for data collected on the deuterium target (open symbols).

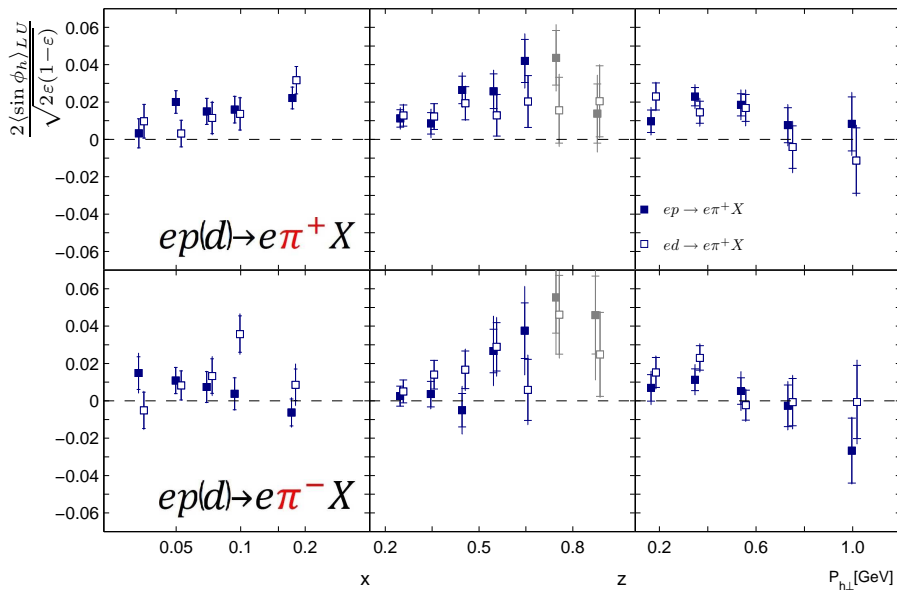


Figure 6.4: Comparison in 1D of VPA π^\pm asymmetries for data collected on the hydrogen target (full symbols) versus asymmetries for data collected on the deuterium target (open symbols).

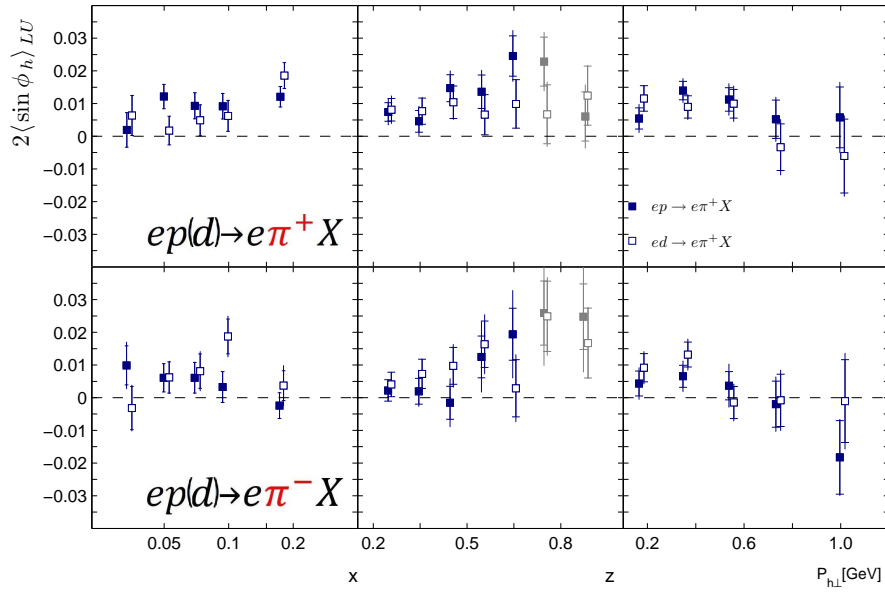


Figure 6.5: Comparison in 1D of LBA π^\pm asymmetries for data collected on the hydrogen target (full symbols) versus asymmetries for data collected on the deuterium target (open symbols).

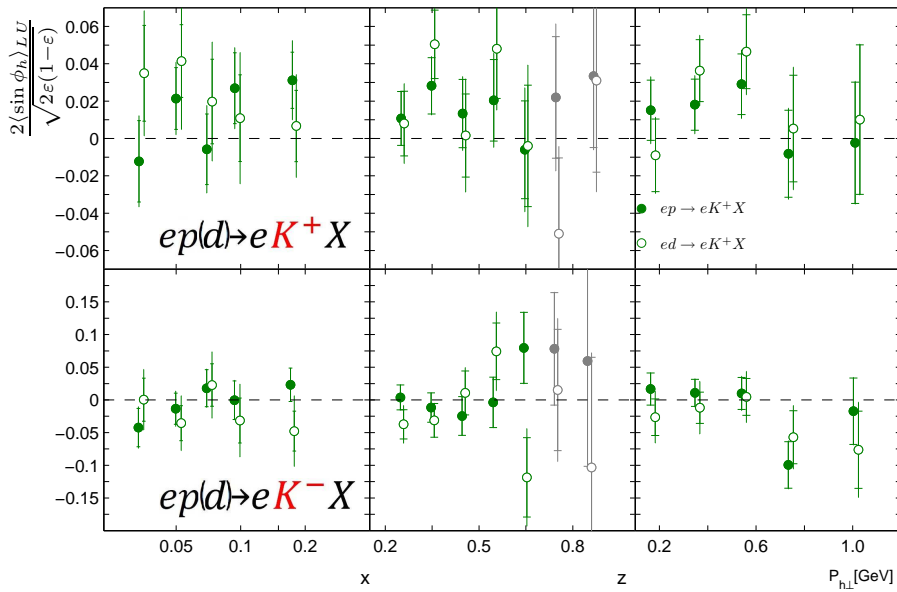


Figure 6.6: Comparison in 1D of VPA K^\pm asymmetries for data collected on the hydrogen target (full symbols) versus asymmetries for data collected on the deuterium target (open symbols).

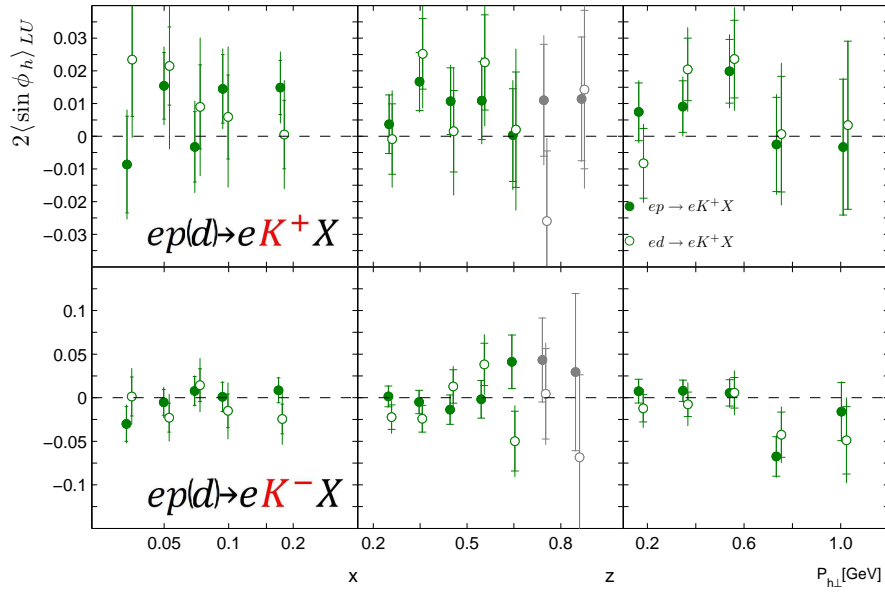


Figure 6.7: Comparison in 1D of LBA K^\pm asymmetries for data collected on the hydrogen target (full symbols) versus asymmetries for data collected on the deuterium target (open symbols).

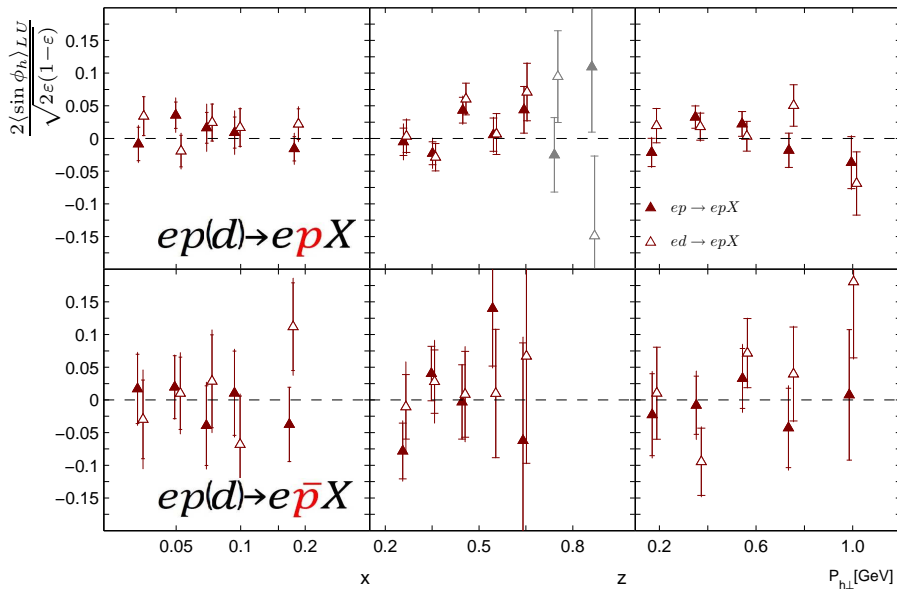


Figure 6.8: Comparison in 1D of VPA p, \bar{p} asymmetries for data collected on the hydrogen target (full symbols) versus asymmetries for data collected on the deuterium target (open symbols).

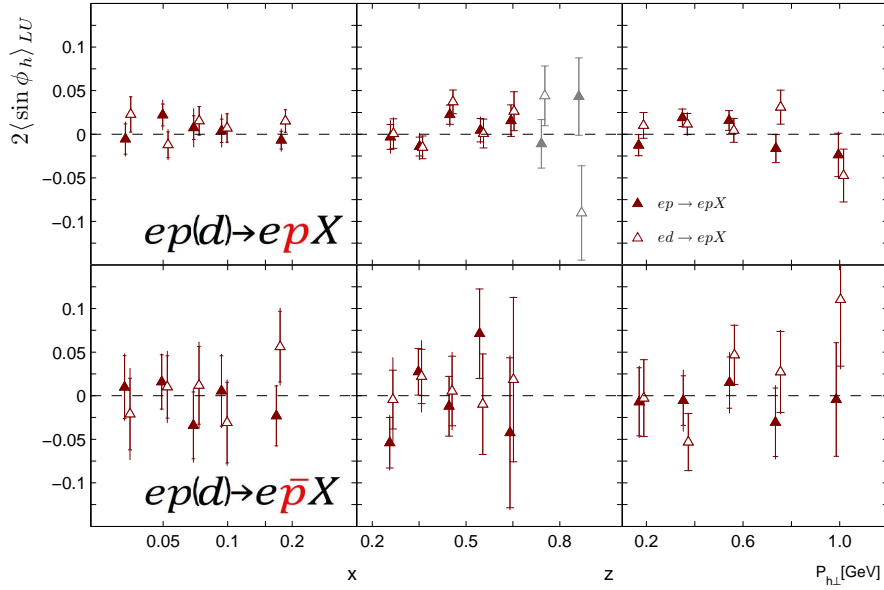


Figure 6.9: Comparison in 1D of LBA p, \bar{p} asymmetries for data collected on the hydrogen target (full symbols) versus asymmetries for data collected on the deuterium target (open symbols).

6.1 Comparison with CLAS and COMPASS experiments

In the present subsection the obtained results are compared to the available results from other experiments, i.e. with results from COMPASS (see [102]) and CLAS (see [103]). The COMPASS experiment uses a muon beam at an energy of 160 GeV and ${}^6\text{LiD}$ fixed target. The target can be considered as a deuterium target and compared with corresponding asymmetries from HERMES. The CLAS experiment uses an electron beam at the energy of 5.5 GeV and a fixed liquid hydrogen target. At HERMES experiment both hydrogen and deuterium fixed targets, and an electron or positron beams at the energy of 27.6 GeV, that lies in between the energies of COMPASS and CLAS experiments, were used. For the comparison with CLAS results the asymmetries at HERMES were extracted on the hydrogen target in the same z -range, $0.4 < z < 0.7$, and their values were multiplied on Q due to $\frac{1}{Q}$ factor, that appears in the structure function (see eq. 2.40) is, contrary to final HERMES results, taken into consideration. This factor can change significantly for different experiments, and experiment depends on the configuration and type of detectors etc., energy of the experiment, and whether it concerns a collider or fixed target. The HERMES results are compared to COMPASS and CLAS in fig. 6.10, 6.11 respectively.

The HERMES asymmetries are compatible with the COMPASS asymmetries in z and $P_{h\perp}$ projections. For the x -projection one can see that the experiments cover different kinematic ranges and overlap only partially. In the region of overlap the comparison with the CLAS results shows an overall agreement for the π^+ asymmetries. The x -projection again demonstrates the different kinematic coverage of the experiments, but the trend is compatible: the π^+ asymmetries increase with increasing of x , and the π^- asymmetries decrease with increasing of x . Also for

the z and $P_{h\perp}$ dependencies a good agreement for the π^+ asymmetries is observed. For the π^- asymmetries in z -dependence one can see a "mirror" picture: the asymmetries are opposite in sign and have similar amplitude values. This opposite behavior can be explained by at least one of four contributions in eq. 2.40, which can have different impact due to difference x-range of two experiments. The role of contribution containing Collins function, eH_1^\perp , could be excluded through the measurements on the deuterium target. This contribution is suppressed for the deuterium target, due to the opposite signs of favored and disfavored fragmentation functions (see [97]) for u and d quarks indicated as $H_1^{\perp h/u}$, $H_1^{\perp h/d}$ respectively, and can be written as:

$$(e^u + e^d) \otimes (H_1^{\perp h/u} + H_1^{\perp h/d}), \text{ where} \quad (6.1)$$

e^u , e^d ... twist-3 PDFs for u and d quarks respectively,

In absence of CLAS data on deuterium this is hard to verify. For $P_{h\perp}$ -projection one can see reasonable compatibility between the results.

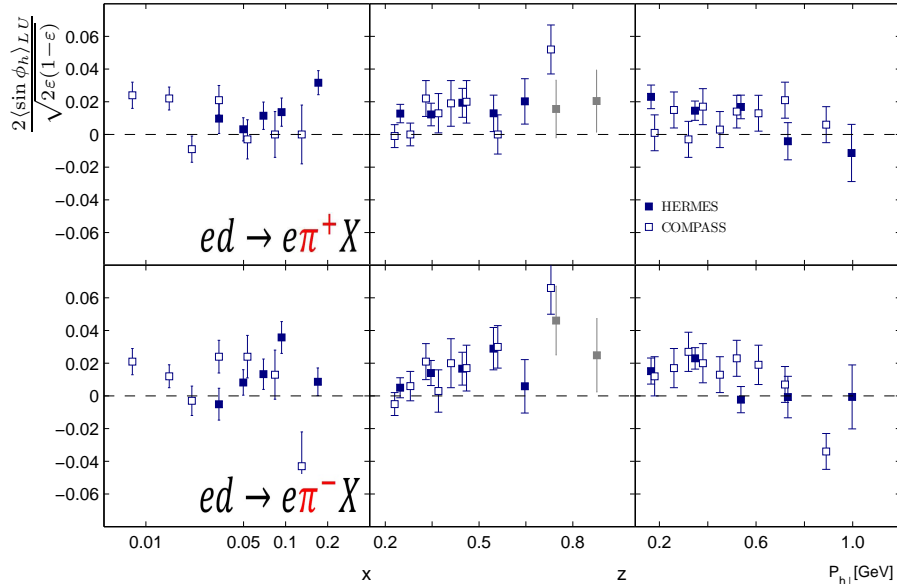


Figure 6.10: Comparison of asymmetries extracted from data collected on deuterium target at HERMES (full symbols) versus asymmetries extracted from data collected on ${}^6\text{LiD}$ target at COMPASS.

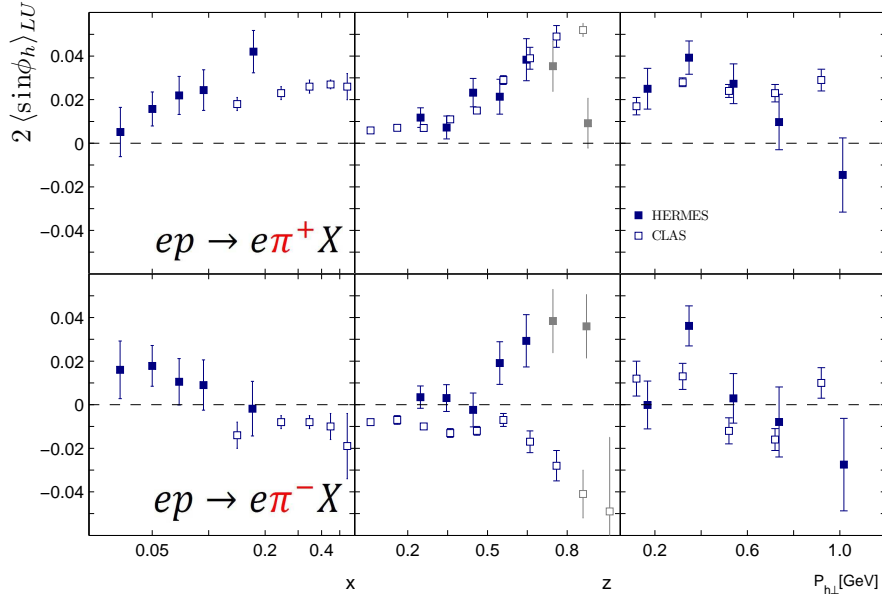


Figure 6.11: Comparison of asymmetries at HERMES (full symbols) versus asymmetries from CLAS both extracted from data collected on hydrogen target.

6.2 Comparison with theory

As it was shown in sec. 2.6, the A_{LU} asymmetry receives contributions from four possible convolutions of PDFs and FFs (see eq. 2.41). In sec. 2 it was explained that at present it is not possible to make proper models of each contribution and include them simultaneously. In the theoretical approach used for the previously published data in [49], only two contributions were calculated simultaneously: eH_1^\perp and $g^\perp D_1$. The two other were neglected using the Wandzura-Wilczek approximation [52]. This theoretical calculation considers two sets of models, which use different possible parametrizations of twist-3 pdf e and g^\perp (see [49], [50], [51]). The asymmetries obtained on a hydrogen target and compared to theory models of Set 1 can be found in figs. 6.12, 6.14, 6.16, and the same asymmetries compared to Set 2 can be found in figs. 6.13, 6.15, 6.17. The same comparison of the asymmetries extracted on deuterium a target with the models of Set 1 and Set 2 is presented in fig. 6.18, 6.20, 6.22 and in fig. 6.19, 6.21, 6.23 respectively. In the figures the HERMES asymmetries are shown as black symbols, the convolutions eH_1^\perp and $g^\perp D_1$ are indicated by the green and blue dashed lines, while their sum is indicated by the red solid line. In comparison plots one can see that two sets (Set 1 and Set 2) lead in particular to different roles of convolutions for hydrogen and deuterium targets. For Set 1 the role of eH_1^\perp for deuterium target is small compared to the its role for hydrogen target and is, as it was explained in previous section, connected with the equal magnitudes of Collins favored and disfavored fragmentation functions. For π^+ asymmetries on hydrogen, Set 2 shows reasonable agreement, although it slightly underestimates data, while it is inconsistent with π^- asymmetries. Set 1 fails to describe both π^+ and π^- asymmetries. For deuterium target Set 2, again shows reasonable agreement of results with π^+ asymmetries, while it fails for description of π^- asymmetries. For K^+ asymmetries obtained on hydrogen, Set 1 shows

positive results and reasonable agreement with data, while Set 2 gives smaller asymmetries consistent with zero, and shows poor agreement. The same is observed for K^+ asymmetries obtained on deuterium. The models for K^- , p and \bar{p} asymmetries of both sets for both targets are consistent with zero. The same is observed for the extracted asymmetries.

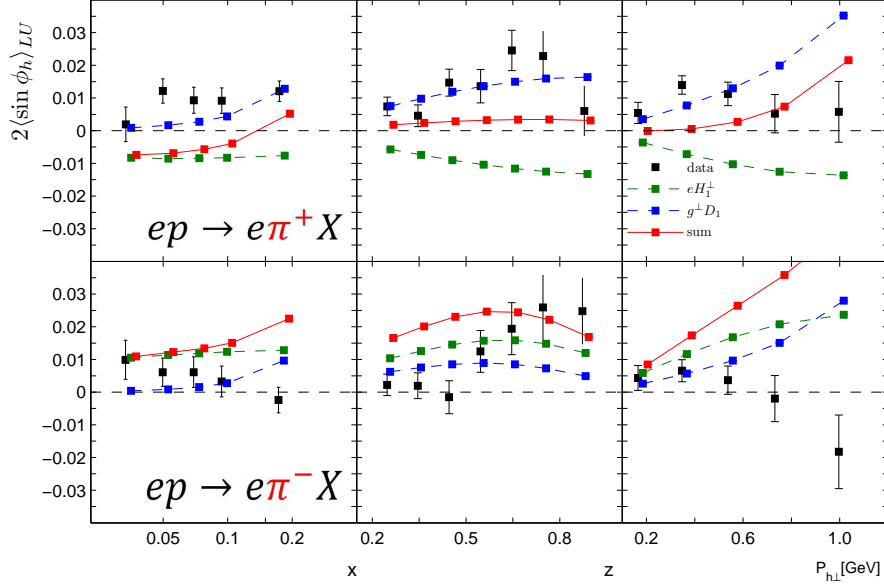


Figure 6.12: Comparison of pion asymmetries extracted for data collected on hydrogen target at HERMES versus asymmetry models from Set 1. The symbols are interconnected with legend description.

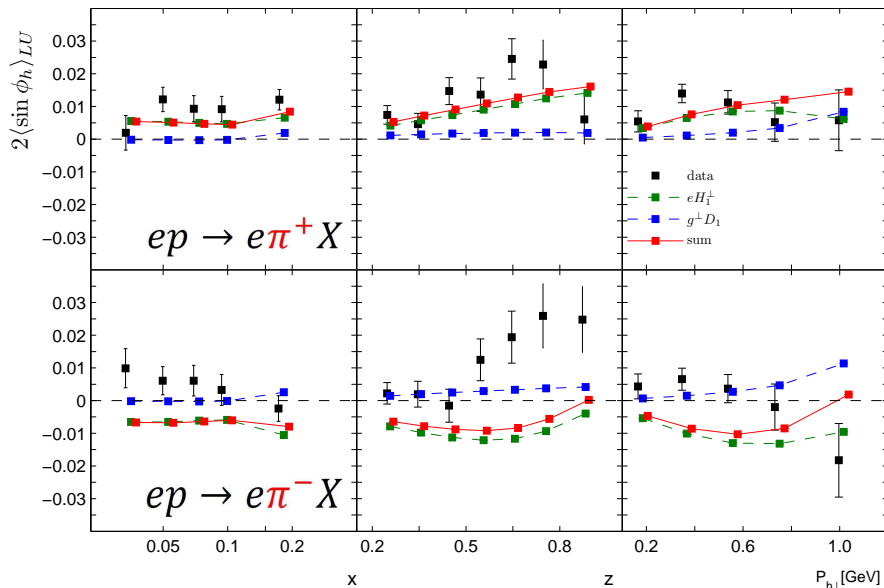


Figure 6.13: Comparison of pion asymmetries extracted for data collected on hydrogen target at HERMES versus asymmetry models from Set 2. The symbols are interconnected with legend description.

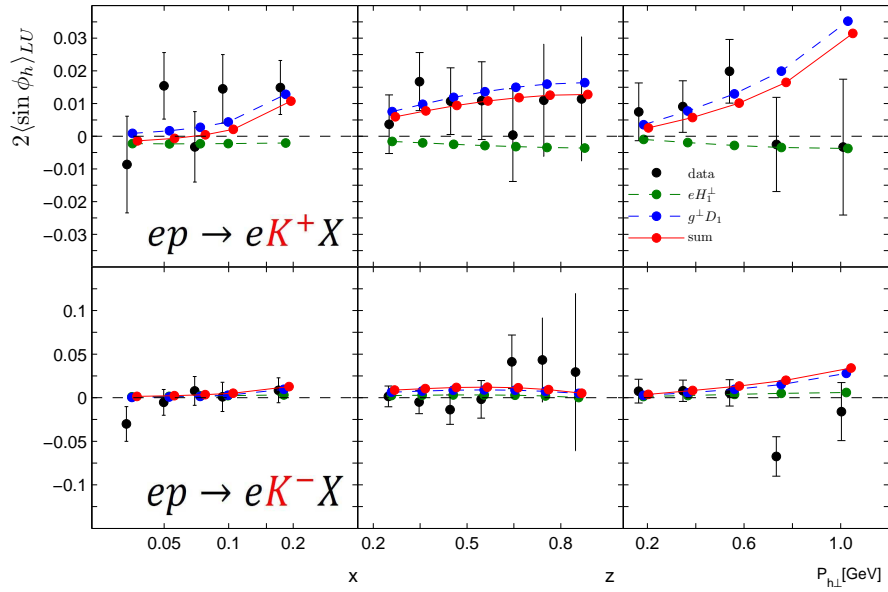


Figure 6.14: Comparison of kaon asymmetries extracted for data collected on hydrogen target at HERMES versus asymmetry models from Set 1. The symbols are interconnected with legend description.

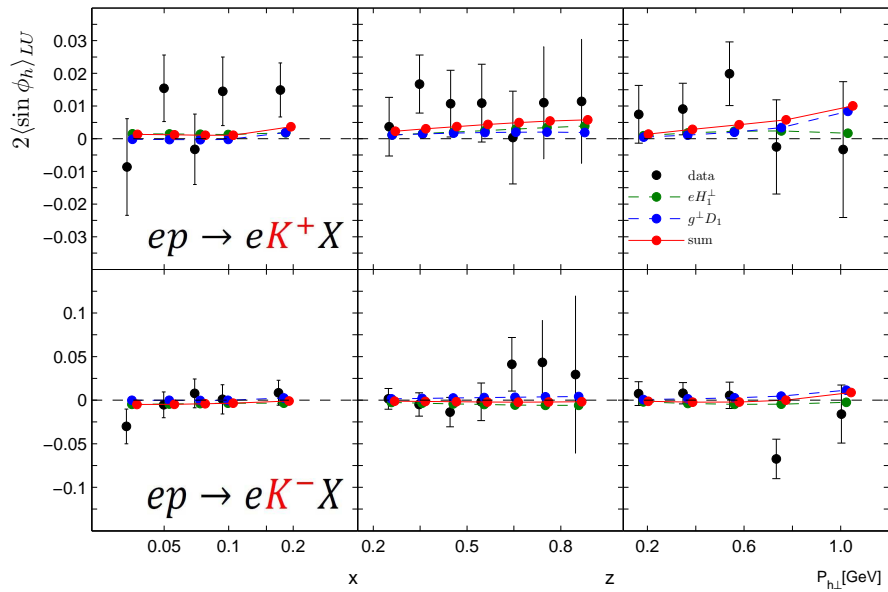


Figure 6.15: Comparison of kaon asymmetries extracted for data collected on hydrogen target at HERMES versus asymmetry models from Set 2. The symbols are interconnected with legend description.

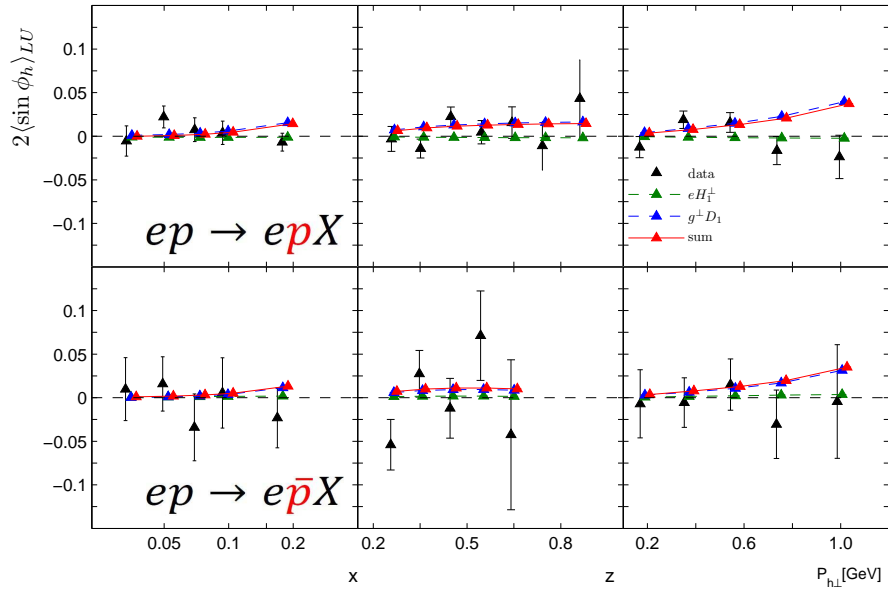


Figure 6.16: Comparison of (anti)proton asymmetries extracted for data collected on hydrogen target at HERMES versus asymmetry models from Set 1. The symbols are interconnected with legend description.

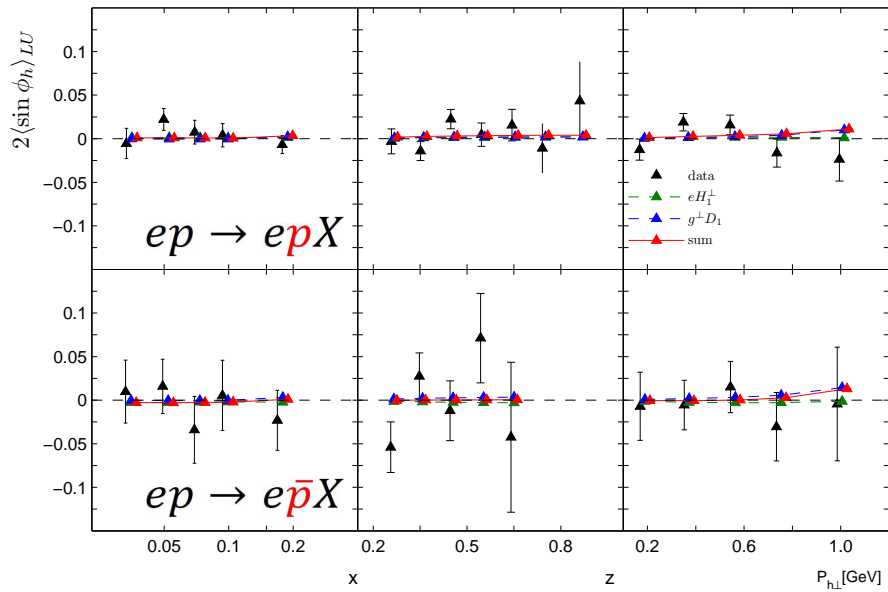


Figure 6.17: Comparison of (anti)proton asymmetries extracted for data collected on hydrogen target at HERMES versus asymmetry models from Set 2. The symbols are interconnected with legend description.

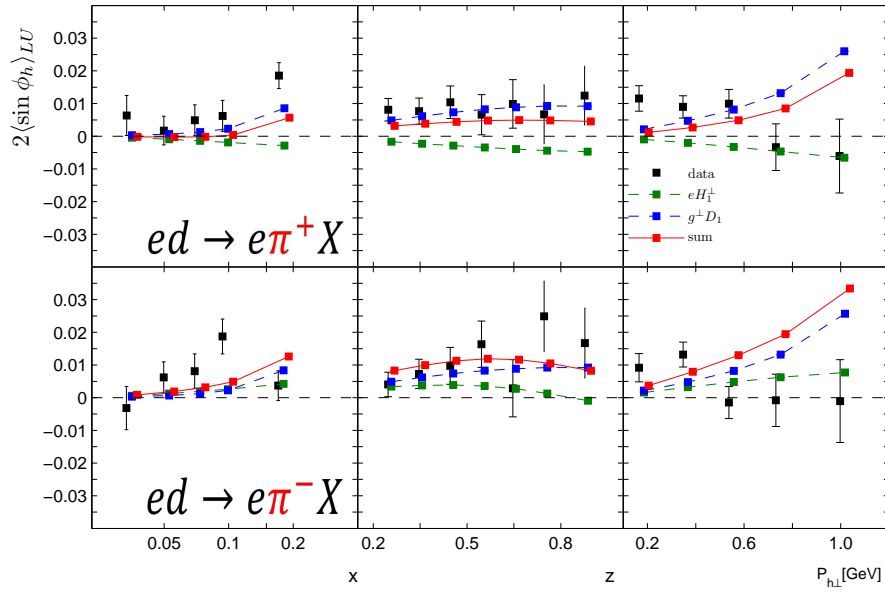


Figure 6.18: Comparison of pion asymmetries extracted for data collected on deuterium target at HERMES versus asymmetry models from Set 1. The symbols are interconnected with legend description.

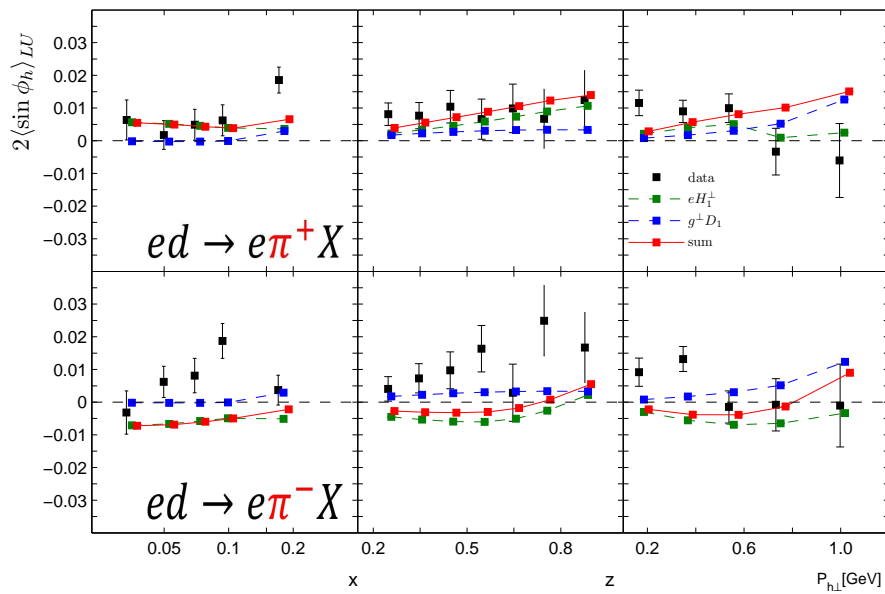


Figure 6.19: Comparison of pion asymmetries extracted for data collected on deuterium target at HERMES versus asymmetry models from Set 2. The symbols are interconnected with legend description.

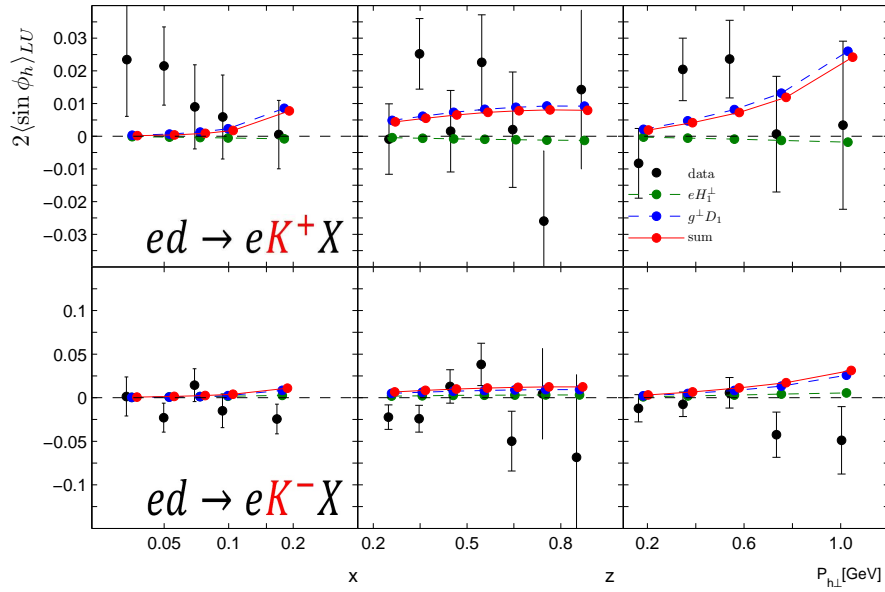


Figure 6.20: Comparison of kaon asymmetries extracted for data collected on deuterium target at HERMES versus asymmetry models from Set 1. The symbols are interconnected with legend description.

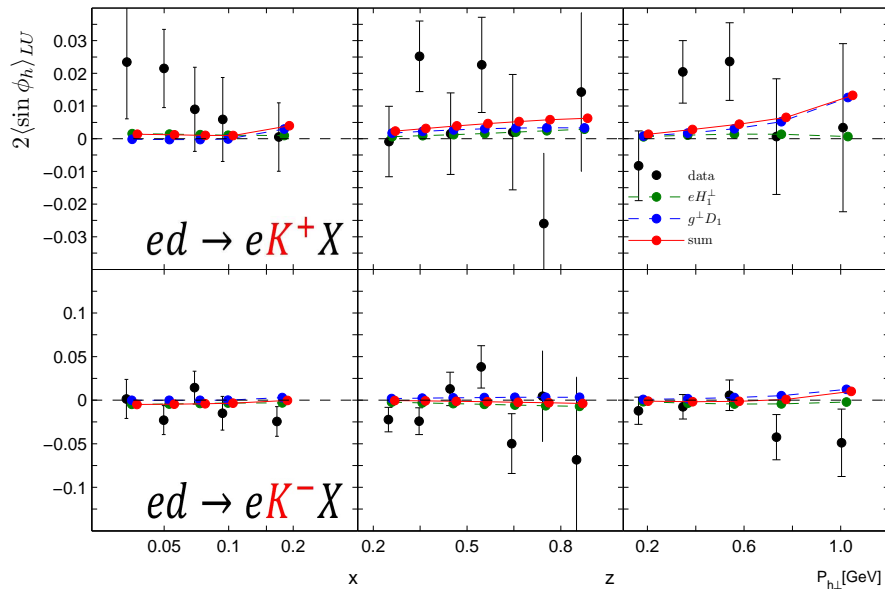


Figure 6.21: Comparison of kaon asymmetries extracted for data collected on deuterium target at HERMES versus asymmetry models from Set 2. The symbols are interconnected with legend description.

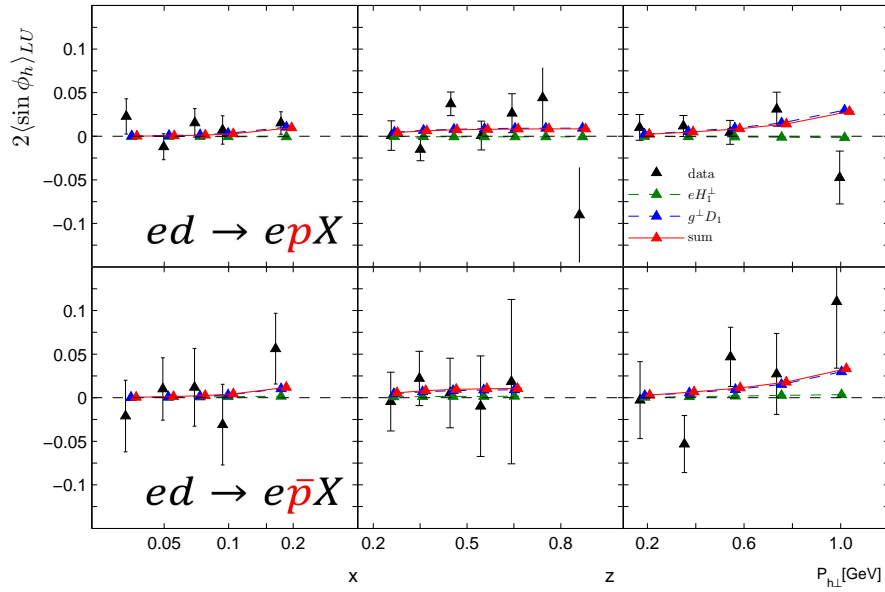


Figure 6.22: Comparison of (anti)proton asymmetries extracted for data collected on deuterium target at HERMES versus asymmetry models from Set 1. The symbols are interconnected with legend description.

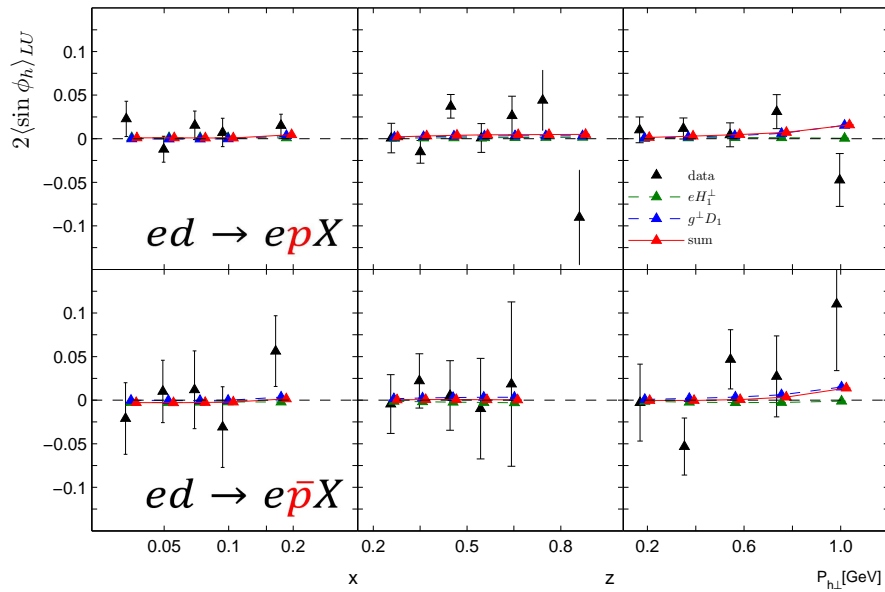


Figure 6.23: Comparison of (anti)proton asymmetries extracted for data collected on deuterium target at HERMES versus asymmetry models from Set 2. The symbols are interconnected with legend description.

Conclusion

In this work the beam single spin asymmetries (BSA) in SIDIS were extracted for charged pions, charged kaons and (anti)protons. The analyzed data was collected at the HERMES experiment during the years 1996-2007 with a longitudinally polarized beam on hydrogen and deuterium targets. The here presented analysis extends previously published results (see [28]). The coincidence of newly extracted results with previously published results and the independent crosscheck of each step of analysis confirms the accuracy of this work.

In the TMD approach (see sec. 2.5) the extracted asymmetry amplitudes present the sum of convolutions of different parton distribution (PDFs) and fragmentation functions (FFs). These TMD functions describe the correlations between transverse momentum of quark, quark spin, target nucleon spin and transverse momentum of the final-state particle. Among these TMDs are the Collins FF H_1^\perp , Boer Mulders PDF h_1^\perp , unpolarized PDF f_1 and unpolarized FF D_1 . assuming non-zero transverse momentum of quark inside the nucleon the extracted asymmetry amplitudes can be interpreted as the results of correlations between transverse momentum of quark, quark spin, target nucleon spin, and transverse momentum of final-state particle. In the here extracted asymmetry each of these twist-2 functions is convoluted with one of the unknown twist-3: e , \tilde{G}^\perp , g^\perp , \tilde{E} . The twist-3 effects are harder to measure, since they are suppressed by the factor $\frac{1}{Q}$. However, the here presented analysis might contribute in improving the knowledge of twist-3 functions.

The π^+ asymmetries extracted from data collected on hydrogen and deuterium are positive. The π^- asymmetries and K^+ are slightly positive. The K^- , p and \bar{p} asymmetries are consistent with zero. The asymmetries of pions increase with increasing z . In general, for all particles the asymmetries decrease with increasing $P_{h\perp}$. Pion asymmetries were compared to results obtained from COMPASS and CLAS experiments, where data was collected on ${}^6\text{LiD}$ and hydrogen targets respectively. Pion asymmetries are in good agreement with COMPASS results (see fig. 6.10). The π^+ asymmetry is in reasonable agreement with CLAS results. The π^- asymmetries are consistent with x and $P_{h\perp}$ projections, while it shows opposite z-dependence and this can indicate different role of TMD functions in different kinematic ranges of the experiments (see fig. 6.11). The results were compared to theoretical predictions (see sec. 6.2). In general, the results are only partially consistent with the theory model, this could be attributed to the missing contributions $f_1\tilde{G}^\perp$ and $h_1^\perp\tilde{E}$ (these two were neglected).

Important aspects of this analysis are the results on the deuterium target, the asymmetries for kaons, protons and antiprotons and the 3D binning, showing the dependence of the asymmetries simultaneously on x, z and $P_{h\perp}$. The 3D results are less sensitive to acceptance (see sec. 5.4). All these results are presented for the first time and will allow to improve the theory models.

Bibliography

- [1] M. Gell-Mann, Y. Ne'emann "The Eightfold Way" Westview Press, p.11, 1964
- [2] E.D. Bloom et al. (1969) "High-Energy Inelastic e-p Scattering at 6° and 10°" Physical Review Letters 23(16): 930-934.
- [3] R. Brandelik et al. (TASSO collaboration) (1979). "Evidence for Planar Events in e+e- Annihilation at High Energies". Phys. Lett. B 86: 243-249
- [4] R. Feynman, J. Bjorken "The behavior of Hadron Collisions at Extreme Energies" High Energy Physics, Third international conference at Stony Brook, pp. 237-249
- [5] J. Ashman et al., (EMC Collaboration), Phys. Lett. B206 (1988) 364.
- [6] See for example, D.L. Adams et al. (E581, E704 Collaborations), Phys. Lett. B 261, 201 (1991); D.L. Adams et al (FNAL-E704 Collaboration), Phys. Lett. B 264, 462 (1991); K. Krueger et al., Phys. Lett. B459, 412 (1991)
- [7] G. Bunce et al., Phys. Rev. Lett. 36, 1113 (1976)
- [8] A. Airapetian, et al., HERMES Collaboration, Phys. Rev. Lett. 84 (2000) 4047;
A. Airapetian, et al., HERMES Collaboration, Phys. Rev. D 64 (2001) 097101.
- [9] H. Avakian, CLAS Collaboration, in: D.G. Crabb., et al. (Eds.), Proceedings of Testing QCD Through SPIN
- [10] D. Adamas, et. al., Spin Muon Collaboration, Phys. Rev. Lett. B 336 (1994) 125;
A. Bravar, Spin Muon Collaboration, Nucl. Phys., A 666 (2000) 314.
- [11] Anna M. et al., COMPASS collaboration, arxiv:1303.2076v1 8 March, 2013
Observables, University of Virginia, April 2002.
- [12] J. Adams et al. (STAR Collaboration), Phys. Rev. Lett. 92, 171801 (2004).
- [13] S.S. Adler et al. (PHENIX Collaboration), hep-ex/0507073;
C. Aidala et al. (PHENIX Collaboration), hep-ex/0410003;
C. Aidala et al. (PHENIX Collaboration), hep-ex/0501054.

-
- [14] F. Videbaek (BRAHMS Collaboration), in Proceedings of 13th International Workshop on Deep Inelastic Scattering (DIS 2005), Madison, Wisconsin, 2005.
- [15] J.P. Ralston and D.E. Soper, Nucl. Phys. B152, 109 (1979).
- [16] J.C. Collins and D.E. Soper, Nucl. Phys. B193, 381 (1981);
J.C. Collins and D.E. Soper, Nucl. Phys. B 194,445 (1982).
- [17] J.C. Collins, D.E. Soper and G. Sterman, "Factorization of Hard Processes ", Stony Brook NY 11794-3840
- [18] D.W. Sivers, Phys. Rev. D 41,83 (1990);
43,261 (1991).
- [19] A. Kotzinian, Nucl.Phys. B441,234 (1995)
- [20] M. Anselmino, M. Boglione, and F. Murgia, Phys. Lett. B 362, 164 (1995).
- [21] U. Elschenbroich, "Transverse Spin Structure of the Proton studied in SEMI-inclusive DIS". The HERMES collaboration, thesis 2006
- [22] M. Burkardt, "Impact parameter dependent parton distributions and transverse single spin asymmetries" Phys. Rev. D66, 114005 (2002)
- [23] R. Jaffe "Spin, Twist and Hadron Structure in Deep Inelastic Processes",arXiv:hep-ph/9602236
- [24] A. Airapetian et al, HERMES Collaboration, Phys. Rev. Lett. 103 (2009) 152002, arXiv:0906.3918, "Observation of the Naive-T-odd Sivers Effect in Deep-Inelastic Scattering"
- [25] A. Airapetian et al, HERMES Collaboration, Phys. Lett. B 693 (2010) 11-16,arXiv:1006.4221 "Effects of transversity in deep-inelastic scattering by polarized protons"
- [26] X. Artru, Proposals for measuring transversity distributions in deep inelastic electron scattering and a model for E-704 asymmetries, prepared for the 5th International Workshop of High-energy Spin Physics, Protvino, Russia, Sep 20-24, 1993, hep-ph/9310323.
- [27] A. Bacchetta, U. D'Alesio, M. Diehl and C.A. Miller , Single-spin asymmetries:The Trento conventions, Phys. Rev. D 70 (2004) 117504
- [28] A. Airapetian, et al.,HERMES Collaboration, Phys. Lett. B 648 (2007),164
- [29] "Beam Single Spin Asymmetry in Azimuthal Distribution of Pion Electroproduction at HERMES" A. Airapetian, et al.,HERMES Collaboration, Draft v. 1.6

- [30] A. Aghasyan, et. al., Phys. Lett. B 704, 397 (2011)
- [31] H. Avakian [CLAS Collaboration] "Measurement of Beam-Spin Asymmetries for π^+ Electroproduction Above the Baryon Resonance Region" ,2004, hep-ex/0301005v2
- [32] J.D. Bjorken, Asymptotic sum rules at infinite momentum, Phys. Rev. 179, 1547-1553,(1969)
- [33] M. Anselmino, A. Efremov, E. Leader. The theory and phenomenology of polarized deep inelastic scattering . Phys. Rept. 261, 1-124(1995)
- [34] M. Diehl and S. Sapeta, On the analysis of lepton scattering on longitudinally or transversely polarized protons, Eur. Phys. J. C41 (2005), 515-533, hep-ph/0503023
- [35] D. Boer and P.J. Mulders , Time reversal odd distribution functions in leptonproduction. Phys. Rev. D 57 (1998) 5780,hep-ph/9711485
- [36] J.C. Collins, Fragmentation of transversely polarized quarks probed in transverse momentum distributions, Nucl.Phys. B396, (1993) 161
- [37] D. Boer and P.J. Mulders, Color gauge invariance in the Drell-Yan process. Nucl. Phys. B569 505-526 (2000)
- [38] P.J. Mulders and R.D. Tangerman, The complete tree-level result up to order $1/Q$ for polarized deep-inelastic leptonproduction, Nucl. Phys. B461,197-237 (1996)
- [39] A.L. Ruiz, thesis "Measurement of transverse single-spin asymmetries in inclusive electroproduction at HERMES" , 2012-2013
- [40] M. Dieffenthaler, thesis "Signals for transversity and transverse-momentum dependent quark distributions studied at HERMES" , 2010
- [41] A.D. Martin, R.G. Roberts, W.J. Stirling and R.S. Thorne "NNLO global parton analysis" Phys. Lett. B531 (2002)216
- [42] A. Prokudin, International School of Physics "Enrico Fermi",Course CLXXX,"Three-dimensional Partonic Structure of the Nucleon" , 2011, Italy, Varenna
- [43] A. Bacchetta, M. Diehl, K. Goeke, A. Metz, P.J. Mulders, M. Schlegel "Semi-inclusive deep inelastic scattering at small transverse momentum" , 2007, hep-ph/0611265
- [44] D.Boer , P.J. Mulders, Phys. Rev. D 57,5780 (1998)
- [45] F. Yuan, Phys.Lett. B 589, 28 (2004)
- [46] L.P. Gamberg, D.S. Hwang, K.A. Oganessyan, Phys. Lett. B 584,276 (2004)

- [47] F. Yuan, hep-ph/0310279
- [48] R. Jakob, P.J. Mulders, J. Rodrigues, Nucl. Phys. A 626, 937 (1997)
- [49] W. Mao, Z. Lu, arXiv:1306.1004v1 (2013)
- [50] W. Mao, Z. Lu, Phys. Rev., D 87, 014012 (2013)
- [51] A. Bacchetta, A. Shafer and J.J. Yang, Phys. Lett., 578, 1009 (2004)
- [52] S. Wandzura and F. Wilczek, Phys. Lett. B 72, 195 (1977)
- [53] A. Bacchetta, R. Kundu, A. Metz and P.J. Mulders, Phys. Lett. B 506, 155 (2001). A. Bacchetta, A. Metz and J.J. Yang, arXiv:hep-ph/0307282
- [54] A. Airapetian et al. [HERMES Collaboration], Observation of the Naive-T-odd Sivers Effect in Deep-Inelastic-Scattering, Phys. Rev. Lett. 103 (2009)
- [55] A. Airapetian et al. [HERMES Collaboration], Effects of transversity in deep-inelastic-scattering by polarized protons. Phys. Lett. B 693 (2010) 11.
- [56] K. Nakamura et al. (PDG), JP G 37, 075021 (2010) "Fragmentation functions in e^+e^- , ep and pp collisions".
- [57] A.A. Sokolov and I.M. Ternov, On Polarization and Spin Effects in Synchrotron Radiation Theory, Sov. Phys. Doklady 8, 1203 (1964)
- [58] M. Beckmann et al. The longitudinal polarimeter at HERA, Nucl. Instrum. Meth. A 479, 334-348
- [59] A. Airapetian, private communication, 2014.
- [60] D.P. Barber et al., The HERA polarimeter and the first observation of electron spin polarization at HERA, Nucl. Instr. Meth., A 329, 79-111 (1993)
- [61] J.T. Brack et al., The HERMES forward tracking chambers: Construction, operation and aging effects. Nucl. Instrum. Meth., A 469 47-54 (2001)
- [62] S. Bernreuther et al., The HERMES back drift chambers. Nucl. Instrum. Meth., A 416, 45-58 (1998)
- [63] A. Andreev et al., Multiwire proportional chambers in the HERMES experiment. Nucl. Instrum. Meth. A 465, 482-497 (2001)
- [64] D.M. Thiessen. The Gas System for the HERMES Transition Radiation Detector. Master's thesis, Simon Fraser University (1996)

- [65] H. Avakian et al. Performance of the electromagnetic calorimeter of the HERMES experiment, Nucl. Instrum. Meth. A 417,69-78 (1998)
- [66] H.E. Jackson [HERMES Collaboration] The HERMES dual radiator RICH: Performance and impact, Nucl.Instrum. Meth. A553 (2005) 205
- [67] N. Akopov et al. [HERMES Collaboration] The HERMES dual-radiator ring imaging cherenkov detector. Nucl. Instrum. and Meth. in Phys., 479(2-3):511-530,2002
- [68] E.Cisbani, Working note on the direct ray-tracing particle identification method for the RICH detector at HERMES, HERMES Internal report (July 1997)
- [69] R.M. Lamb, "The Boer-Mulders and Cahn effects: azimuthal modulations in the spin-independent SIDIS cross section at HERMES", 2010
- [70] Y. Miyachi T. Hasegawa, Estimation of RICH particle identification accuracy using decaying particles./group01/richgrp/dPsys/pmatrix.v3.0/richsys.pdf, 2005
- [71] R. Kaiser, "Particle identification at HERMES", HERMES internal report 97-025 (1997)
- [72] Th. Bayes, An essay towards solving a probleme in the doctrine of chances, Philosophical Transactions of Royal Society of London ,53, 370 (1763)
- [73] C. Baumgarten et al. "The storage cell of the polarized internal H/D gas target of the HERMES experiment" . Nucl. Instr. and Meth. A 508 (2003), 268
- [74] A. Nass et al. "The HERMES polarized atomic beam source", Nucl. Instr. and Meth. A 505 (2003) 633
- [75] C. Baumgarten et al, A gas analyser for the internal polarized target of the HERMES experiment. Nucl. Instrum. Meth. A 508, 268-275(2003)
- [76] A.Airapetian et al. (HERMES Collaboration) The HERMES polarized hydrogen and deuterium gas targets in the HERA electron storage ring, Nucl. Instrum. Meth. A 540, 68-101 (2004)
- [77] C. Baumgarten et al., An atomic beam polarimeter to measure the nuclear polarization in the HERMES gaseous polarized hydrogen and deuterium target, Nucl. Instrum. Meth. A482,606-618 (2002)
- [78] A.Movsisyan, thesis "Deeply Virtual Compton Scattering off a Deuterium Target at the HERMES experiment" (2010)
- [79] CERN Programming Techniques Group, ADAMO reference manual version 3.3 (1993); ADAMO Entity-relationship Programming System, Users Guide version 3.3 (1993)

-
- [80] R.E. Kalman, "New approach to linear filtering and prediction problems", Transactions of the ASME-Journal of basic engineering, D 82, 35-45 (1960)
- [81] M. Beckmann, Extracton of polarised quark distributions of the nucleon from deep inelastic scattering at the HERMES experiment, DESY-THESIS-2000-029 (2000)
- [82] Robert N.Cahn, Azimuthal Dependence in Leptoproduction: A simple Parton model calculation. Phys. Lett. b78:269,1978
- [83] M. Schlegel, A. Metz, "Two-photon exchange in inclusive DIS" (2009), arXiv:0902.0781v1 [hep-ph] 4 Feb 2009.
- [84] T. Sjostrand, S. Mrenna and P.Z. Skands, PYTHIA 6.4 Physics and Manual, JHEP 0605 (2006) 026 hep-e/0603175
- [85] I. Akushevich, H. Bottcher and D. Ryckbosch, RADGEN 1.0: Monte Carlo generator for radiative events in DIS on polarized and unpolarized targets (1998), hep-e/9906408
- [86] B. Anderson et al. Parton Fragmentation and String Dynamics, Phys.Rept. 97 31 (1983).
- [87] GEANT manual - Detector description and simulation tool (1993)
- [88] Blanka Sobloher, Riccardo Fabbri and other, Polarisation at HERA - Reanalysis of the HERA II Polarimeter Data, 2012, arxiv:1201.2894v1
- [89] D. Boer, R. Jakob, and P. J. Mulders, Angular dependences in electroweak semi-inclusive leptoproduction, Nucl. Phys. B564 (2000) 471-485
- [90] A. Bacchetta, M. Diehl, K. Goeke, A. Metz, P. J. Mulders, and M. Schlegel, Semi-inclusive deep inelastic scattering at small transverse momentum, JHEP 0702 (2007) 093.
- [91] Miller C.A., Extracting azimuthal fourier moments from sparse data, in HERMES Transversity Week (Gent) 2006.
- [92] A. Rostomyan, International School of Physics "Enrico Fermi", Course CLXXX, "Three-dimensional Partonic Structure of the Nucleon", p.261
- [93] Solmitz F.T., Annu.Rev.Nucl.Part.Sci.,14 (1964) 375
- [94] M. Diefenthaler, L.L. Pappalardo. Fourier analysis of double-spin asymmetries ALT for pions and charged kaons.
- [95] A.L. Ruiz. Measurement of transverse single -spin asymmetries in inclusive electroproduction at HERMES. 2012.

-
- [96] F. Giordano "The role of transverse momentum and spin in unpolarized semi-inclusive deep inelastic scattering", PhD Thesis, University of Ferrara (2008)
- [97] M. Anselmino, M. Baglione, U. D'Alesio, A. Kotzinian, F. Murgia, A. Prokudin and S. Melis Nucl. Phys. Proc.Suppl. 191, 98 (2009).
- [98] Conference Baryons 2013, UK Glasgow, talk "Beam Spin Asymmetries in SIDIS at HERMES"
- [99] Deutsche Physikalische Gesellschaft (DPG), Frankfurt 2014, talk "Beam Spin Asymmetries in SIDIS at HERMES"
- [100] A. Airapetian et al, Phys. Rev. D 87 (2013) 012010
- [101] X.-G. Lu and Z. Ye. Simultaneous Extraction of the BSAs and the BCA Associated with DVCS with the Extended Maximum Likelihood Method. Internal Note, 07-001, 2007.
- [102] Anna M. et al., COMPASS collaboration, "Measurement of azimuthal hadron asymmetries" in semi-inclusive deep inelastic scattering off unpolarized nucleons (2014). DOI:10.1016/j.nuclphysb.2014.07.019
- [103] W. Gohn, et al., CLAS collaboration, "Beam-spin asymmetries from Semi-inclusive Pion Electroproduction" (2014, 15 April) , arXiv: 1402.4097v2.

Acknowledgements

This work could not been finished without cooperation of colleagues and friends. I could write a very long list of names of the people, who gave their contributions to this dissertation. It would be inconvenient to forget somebody. Therefore, I want to thank the HERMES group at DESY for the discussions and remarks given to this analysis. I am greatly appreciative of my supervisors: Gunar Schnell, Charlotte Van Hulse, Amy Rostomyan and Sergey Yaschenko, who continuously contributed with their ideas and comments to the dissertation.

I thank Prof. Michael Düren for the opportunity to make this analysis, for discussions at Giessen and useful material, which was used for theory part of the thesis. Special thanks goes to Sabine Krohn for help in painful for me administrative things.

I'm grateful to my friends and, especially to Maya Golembiovskaya, who supported me from the beginning.

Finally, I want to thank my family for their presence in my thoughts and deals.

Erklärung zur Dissertation

Ich erkläre: Ich habe die vorgelegte Dissertation selbständig und ohne unerlaubte fremde Hilfe und nur mit den Hilfen angefertigt, die ich in der Dissertation angegeben habe. Alle Textstellen, die wörtlich oder sinngemäß aus veröffentlichten Schriften entnommen sind, und alle Angaben, die auf mündlichen Auskünften beruhen, sind als solche kenntlich gemacht. Bei den von mir durchgeführten und in der Dissertation erwähnten Untersuchungen habe ich die Grundsätze guter wissenschaftlicher Praxis, wie sie in der Satzung der Justus-Liebig-Universität Gießen zur Sicherung guter wissenschaftlicher Praxis niedergelegt sind, eingehalten.

Hamburg, November 25th, 2014
Vitaly Zagrebelnyy
